

DESIGN AND ANALYSIS OF FULLY MAGNETIC
CONTROL FOR PICOSATELLITE STABILIZATION

A Thesis
presented to
the Faculty of
California Polytechnic State University, San Luis Obispo

In Partial Fulfillment
of the Requirements for the Degree
Master of Science in Aerospace Engineering

by
Daniel Vernon Guerrant

June 2005

AUTHORIZATION FOR REPRODUCTION
OF MASTER'S THESIS

I grant permission for the reproduction of this thesis in its entirety or any of its parts, without further authorization from me.

Signature

Date

APPROVAL PAGE

TITLE: Design and Analysis of Fully Magnetic Control for Picosatellite Stabilization

AUTHOR: Daniel Vernon Guerrant

DATE SUBMITTED: June, 2005

Dr. Jordi Puig-Suari, Advisor and Committee Chair Date

Dr. Eric Mehiel, Committee Member Date

Dr. Clark Turner, Committee Member Date

ABSTRACT

Design and Analysis of Fully Magnetic Control for Picosatellite Stabilization

Daniel Vernon Guerrant

This thesis explores the possibilities of achieving three-axis stability on a picosatellite using only magnetic torquers for actuation. The problem is broken into two phases: detumbling and stabilization. The first phase uses the B-dot algorithm to lower the spacecraft rotation to that of the local magnetic field and only requires magnetometers for sensing the field. The algorithm was found to be very resilient to high noise levels, inaccurately calibrated magnetometers, and magnetorquer failure and performed very well even with initial velocities above 10 rpm. The second phase implements a proportion and derivative feedback controller to achieve 10°-20° of pointing accuracy. This algorithm required full knowledge of attitude and rates, and requirements for potential sensors were explored. It was found to be stable even with extremely low resolution and noisy sensors, albeit with an increase in pointing error. The algorithm was also found to be functional with limited controllability under magnetorquer failure. Both simulations include models of the hardware and the gravity gradient disturbance torque.

Table of Contents

	Page
List of Tables	viii
List of Figures	ix
Nomenclature	xi
1 INTRODUCTION	1
2 THEORY AND BACKGROUND	2
2.1 CubeSat/PolySat	2
2.2 Magnetic Torquing.....	3
2.3 Modeling the Earth's Magnetic Field	4
2.4 Coordinate Reference Frames and Transformations.....	4
2.4.1 The Body Frame	5
2.4.2 The Inertial Frame.....	5
2.4.3 The Orbital Frame.....	5
2.4.4 Successive Quaternion Rotations.....	6
2.4.5 Transformation of Angular Rates	7
2.5 The Equations of Motion	8
2.6 Attitude Disturbance Torques	8
2.6.1 Minimum Torquing Ability	9
2.6.2 Magnetic	9
2.6.3 Aerodynamic Drag.....	9
2.6.4 Gravity Gradient	10
2.6.5 Solar Pressure.....	10

2.6.6	Summary	11
2.7	Survey of the Field.....	11
2.7.1	B-dot Controller	12
2.7.2	Three-Axis Controller.....	13
3	HARDWARE	14
3.1	Side and Front Panels.....	15
3.2	Magnetometers.....	16
3.3	Magnetorquers	17
4	ATTITUDE SIMULATION COMPONENTS.....	18
4.1	Orbit Propagator.....	18
4.2	Magnetic Field Estimation.....	18
4.3	Disturbance Torques	19
4.4	Hardware Models.....	19
4.4.1	Magnetorquers	19
4.4.2	Magnetometers.....	20
4.4.3	Other Possible Attitude Determination Hardware	22
4.5	B-dot Detumbling Algorithm.....	23
4.6	Three-Axis Control Algorithm	23
4.7	Computation.....	25
4.8	Summary of Simulation Assumptions	26
5	ATTITUDE SIMULATION RESULTS	27
5.1	B-dot Detumbling	28
5.1.1	Explanation of B-dot plots	28

5.1.2	Optimum Gain Determination	29
5.1.3	Optimum Pulse Time Determination	35
5.1.4	Effect of Magnetometer Noise.....	40
5.1.5	One and Two Torquers Out Performance	46
5.1.6	CP2 Method vs. CP3 Method	49
5.1.7	B-Dot Conclusions.....	51
5.2	Three-Axis Control	52
5.2.1	Explanation of Three-axis Plots.....	52
5.2.2	Optimum Gains Determination.....	54
5.2.3	Optimum Pulse Time Determination	60
5.2.4	Effect of Sensor Resolution	64
5.2.5	Effect of Sensor Noise	69
5.2.6	One and Two Torquers Out Performance	74
5.2.7	Commanding Different Quaternions.....	77
5.2.8	Commanding in the Orbital Frame	79
5.2.9	Three-Axis Conclusions.....	82
5.3	Comparison of B-dot and Three-Axis Controllers.....	82
6	FUTURE WORK.....	84
	BIBLIOGRAPHY.....	86
	Appendix A: Magfd.m.....	87
	Appendix B: CP2 Magnetometer Calibration Data	91
	Appendix C: Orbit Propagation and Attitude Simulator	92

List of Tables

Table 2.1: Worst Case Attitude Disturbance Torques	11
Table 5.1: Three-axis gain investigation.....	60
Table 5.2: Results of Pulse Length Variation	64
Table 5.3: Comparison of B-dot and three-axis algorithms.....	83
Table B.1: Calibration data for CP2 flight panels.....	91

List of Figures

Figure 2.1: The inertial and orbital frames	6
Figure 3.1: CP2 Engineering Model	14
Figure 3.2: CP2 side panel interior face.....	15
Figure 3.3: CP2 side panel with HMC 1052 magnetometer highlighted.....	16
Figure 3.4: CP2 Side Panel with approximate torquer location.....	17
Figure 5.1: Ground track for 5 orbits	27
Figure 5.2: B-dot for 1.5 orbits with $K = 17e4$ and $\delta t = 10\text{sec}$	30
Figure 5.3: B-dot for 1.5 orbits with $K = 11e4$ and $\delta t = 10\text{sec}$	31
Figure 5.4: B-dot for 1.5 orbits with $K = 8e4$ and $\delta t = 10\text{sec}$	32
Figure 5.5: B-dot for 1.5 orbits with $K = 2e4$ and $\delta t = 10\text{sec}$	33
Figure 5.6: B-dot for 1 orbit with $\delta t = 12\text{ sec}$ and $\omega_o = 1\text{ rpm}$	36
Figure 5.7: B-dot for 1.5 orbit with $\delta t = 1\text{sec}$ and $\omega_o = 14\text{ rpm}$	37
Figure 5.8: B-Dot Tip-off Velocity Performance	38
Figure 5.9: B-dot for 1 orbit with $\delta t = 2\text{sec}$ and $\omega_o = 1\text{ rpm}$	39
Figure 5.10: B-dot for 1 orbit with $\delta t = 2\text{sec}$, $\omega_o = 7\text{ rpm}$, $\sigma = 20\text{ bits}$	41
Figure 5.11: B-dot for 2 orbits with $\delta t = 10\text{sec}$, $\omega_o = 0.5\text{ rpm}$, $\sigma = 0\text{ bits}$	42
Figure 5.12: B-dot for 2 orbits with $\delta t = 10\text{sec}$, $\omega_o = 0.5\text{ rpm}$, $\sigma = 2\text{ bits}$	43
Figure 5.13: B-dot for 2 orbits with $\delta t = 10\text{sec}$, $\omega_o = 0.5\text{ rpm}$, $\sigma = 6\text{ bits}$	44
Figure 5.14: Noise level vs. average settling rates.....	45
Figure 5.15: B-dot for 1.5 orbits with $\delta t = 10\text{sec}$, $\omega_o = 1\text{ rpm}$, $\sigma = 3\text{ bits}$, torquer 1 inactive	47
Figure 5.16: B-dot, 1.5 orbits, $\delta t = 10\text{sec}$, $\omega_o = 1\text{ rpm}$, $\sigma = 3\text{ bits}$, torquers 1 and 2 inactive	48
Figure 5.17: CP2 B-dot for 1 orbit with $\delta t = 4\text{ sec}$, $\omega_o = 3\text{ rpm}$, $\sigma = 6\text{ bits}$	50

Figure 5.18: 3-axis, $C_1 = 4e-2$, $C_2 = 3e-5$, $\delta t = 20\text{sec}$, 5 orbits	55
Figure 5.19: 3-axis, $C_1 = 5e-2$, $C_2 = 3e-5$, $\delta t = 20\text{sec}$, 3 orbits	56
Figure 5.20: 3-axis, $C_1 = 2e-2$, $C_2 = 1e-5$, $\delta t = 20\text{sec}$, 5 orbits	57
Figure 5.21: 3-axis, $C_1 = 2e-2$, $C_2 = 2e-5$, $\delta t = 20\text{sec}$, 5 orbits	58
Figure 5.22: 3-axis, $C_1 = 4e-2$, $C_2 = 3e-5$, $\delta t = 20\text{sec}$, 5 orbits, 3° shutoff	59
Figure 5.23: 3-axis, $C_1 = 4e-2$, $C_2 = 3e-5$, $\delta t = 17\text{sec}$, 4 orbits, 3° shutoff	62
Figure 5.24: 3-axis, $C_1 = 4e-2$, $C_2 = 3e-5$, $\delta t = 10\text{sec}$, 5 orbits, 3° shutoff	63
Figure 5.25: 3-axis, $C_1 = 2e-2$, $C_2 = 2e-5$, $\delta\omega = 1e-3$ rad/s, $\delta q = 0.01$	65
Figure 5.26: 3-axis, $C_1 = 4e-2$, $C_2 = 3e-5$, $\delta\omega = 0.01$ deg/s, $\delta q = 0.01$	66
Figure 5.27: 3-axis, $C_1 = 4e-2$, $C_2 = 3e-5$, $\delta\omega = 1e-4$ rad/s, $\delta q = 0.5$	67
Figure 5.28: 3-axis, $C_1 = 4e-2$, $C_2 = 3e-5$, $\delta\omega = 0.01$ deg/s, $\delta q = 0.1$	68
Figure 5.29: 3-axis, $C_1 = 4e-2$, $C_2 = 3e-5$, $\delta\omega = 1e-4$ rad/s, $\delta q = 0.1$, $\sigma_\omega = 2e-4$ rad/s, $\sigma_q = 0.1$...	70
Figure 5.30: 3-axis, $C_1 = 3e-2$, $C_2 = 2e-5$, $\delta\omega = 1e-4$ rad/s, $\delta q = 0.1$, $\sigma_\omega = 4e-4$ rad/s, $\sigma_q = 0.2$...	71
Figure 5.31: 3-axis, $C_1 = 3e-2$, $C_2 = 2e-5$, $\delta\omega = 1e-4$ rad/s, $\delta q = 0.1$, $\sigma_\omega = 5e-4$ rad/s, $\sigma_q = 0.01$.	72
Figure 5.32: 3-axis, $C_1 = 4e-2$, $C_2 = 3e-5$, $\delta\omega = 1e-4$ rad/s, $\delta q = 0.1$, $\sigma_\omega = 1e-4$ rad/s, $\sigma_q = 0.5$...	73
Figure 5.33: 3-axis, $C_1 = 3e-2$, $C_2 = 2e-5$, 7 orbits, b_2 torquer out	75
Figure 5.34: 3-axis, $C_1 = 3e-2$, $C_2 = 2e-5$, b_1 torquer out	76
Figure 5.35: 3-axis, same parameters as Figure 5.34, $q_d = [\sqrt{2}/2 \quad 0 \quad 0 \quad \sqrt{2}/2]$	78
Figure 5.36: Orbital frame, $C_1 = 2e-2$, $C_2 = 1e-5$	80
Figure 5.37: Orbital frame, $C_1 = 3e-2$, $C_2 = 2e-5$	81

Nomenclature

<i>Symbol</i>	<i>Units</i>	<i>Description</i>
a	T/bit	Magnetometer calibration slope
b	T	Magnetometer calibration offset
b_i	--	ith direction in the body frame
i	Amps	Current
i_i	--	ith direction in the inertial frame
n	--, rad/s	Number of torquer coil turns, Instantaneous mean motion
o_i	--	ith direction in the orbital frame
q_i	--	ith component of the quaternion vector
q_e	--	Quaternion error vector
A	m^2	Area
B	Tesla, Gauss	Geomagnetic flux density
C_D	--	Coefficient of drag in free molecular flow
C_1	$A \cdot m^2 \cdot s / rad$	Three-axis controller rate gain
C_2	$A \cdot m^2$	Three-axis controller position gain
GG	--	Gravity gradient
H	N-m-s	Angular momentum
I	$kg \cdot m^2$	Mass moment of inertia
K	$A \cdot m^2 \cdot s / T$	B-dot controller gain
M	$A \cdot m^2$, N-m	Magnetic dipole moment, Moment
$S:N$	--	Signal-to-noise ratio
T	N-m, --	Torque
v	rad	True anomaly
σ	--	Standard deviation of a simulated noise component
ω	rad/s, deg/s	Angular velocity

1 INTRODUCTION

The major difficulties with a picosatellite project are the space, mass, and power limitations. Any attitude control system must be extremely compact and lightweight, so one with a consumable fuel is impractical. While several different attitude control systems were considered, magnetorquers are the simplest, lightest, and most compact. Momentum wheels could be implemented on a future satellite in order to improve pointing accuracy; however, magnetorquers would still be required for momentum dumping. Magnetorquers have several drawbacks, however. First, they require a considerable amount of a picosatellite's already tight power and computational resources. Secondly, their controllability at any given time is limited due to the nature of magnetic torquing. Thirdly, magnetic control is a highly non-linear problem that makes it impossible to implement most traditional control algorithms. This thesis concerns itself with developing and simulating two control algorithms for magnetic stabilization of a CubeSat-style picosatellite as well as simulating their performance on orbit; however, the simulation could conceivably be applied to any size satellite by changing the parameters. Both systems are optimized and then several non-ideal cases considered using fully non-linear simulations.

2 THEORY AND BACKGROUND

2.1 *CubeSat/PolySat*

The CubeSat program was established by Stanford University and California Polytechnic State University (Cal Poly) in 1999 in order to develop a cost-effective platform to allow students to pursue research projects in space. CubeSat has developed a deployment system, the PolySat-Picosatellite Orbital Deployer (P-POD), and handles the logistics of export controls and interfacing with the launch provider. Among the restrictions imposed on CubeSats are a mass of less than 1 kg and that it must be a cube with 10cm sides. The program has had one launch to date, but currently has forty universities, high schools, and private firms developing satellites for future launches.

The PolySat program is Cal Poly's CubeSat development team and was established in 2000. It has currently completed two satellites, CP1 and CP2, and both are scheduled to accompany the next CubeSat launch. While CP1 is a fairly simple device, CP2 was built with the goal of working towards a standardized bus with power, mass, and volume set aside for a generic payload. This would allow future PolySats to be developed more rapidly.

Concurrent with this goal is the development and refinement of the picosatellite's attitude determination and control system (ADCS). More advance ADCS systems would allow increasingly complex and therefore useful payloads to be tested and qualified in space. To that end, one of the secondary missions of CP2 is to flight test the B-dot detumbling algorithm that is analyzed here. This mission will also attempt to use magnetometers and the solar panels as

crude sun-sensors for attitude determination. Unfortunately, the determination portion will be attempted on the ground due to insufficient onboard memory and processing power. CP3 will attempt to take both of these missions one step further by adding sensors and moving the determination portion onboard. It could then use the onboard determination to test the fully magnetic controller developed and simulated here.

2.2 Magnetic Torquing

PolySat uses a set of five magnetorquers imbedded in the spacecraft side panels in order to provide the torque necessary for attitude control. These torquers operate on the same principle as a compass needle, and the torque is given by:

$$\vec{T} = \vec{M} \times \vec{B} \quad \text{and} \quad M_i = i_i \cdot n \cdot A$$

2.1

Where T is the torque, M is the magnetic dipole moment generated by the torquers, B is the magnetic flux density of the earth, i is the current in the torquer, n is the number of turns in the torquer coil, and A is the average of the area enclosed by each loop. Throughout this report, $n \cdot A$ will be substituted for nA which is the sum of the areas enclosed by each torquer loop. On the PolySat side panel layout this is 0.1503m^2 . Because the torque is a cross-product, it is always perpendicular to the magnetic field. In orbit, this presents the problem that only two axes are controllable at any given time. Since the spacecraft experiences two full rotations of the Earth's magnetic field per orbit, though, all axes are controllable over time. Additionally, the maximum torque available at any given time is directly proportional to the magnitude of the Earth's magnetic field vector. At the 600-700km orbit that CubeSat operates at, this can range from ~200mGs at certain points near the equator to ~500mGs near the magnetic poles.¹

2.3 Modeling the Earth's Magnetic Field

Simulating control with magnetic torquers requires knowledge of the magnetic flux density, B , at any point in the spacecraft's orbit. This information was calculated using the 10th generation International Geomagnetic Reference Field (IGRF-10) which was released by the International Association of Geomagnetism and Aeronomy in January 2005 and is valid until 2010. The IGRF is a series of Gaussian coefficients that model the Earth's main field and its annual rate of change. The field is calculated as the negative gradient of a scalar potential V :

$$\mathbf{B} = -\nabla V$$

This can be represented by the truncated series expansion:

$$V(r, \theta, \lambda, t) = R \sum_{n=1}^{\infty} \left(\frac{R}{r} \right)^{n+1} \sum_{m=0}^n (g_n^m(t) \cos m\lambda + h_n^m(t) \sin m\lambda) P_n^m(\theta)$$

where r is the distance from the center of the Earth, θ is the colatitude (90° -latitude), λ is the longitude, R is a reference radius (6371.2 km), $g_n^m(t)$ and $h_n^m(t)$ are the coefficients at time t , and $P_n^m(\theta)$ are the Schmidt semi-normalized associated Legendre functions of degree n and order m . The main field coefficients g and h are functions of time, and for the IGRF the change is assumed linear over five-year intervals. In a source-free environment such as orbit, the IGRF is accurate down to 1 nT.²

2.4 Coordinate Reference Frames and Transformations

This section defines the various coordinate frames used during attitude simulation. All frames are right orthogonal. The attitude simulation and equations of motion are represented and calculated in the inertial frame. The state vector must then be transformed to and from the orbital frame in order to provide full control in both frames.

2.4.1 The Body Frame

This frame has axes that correspond to the principle inertial axes of the spacecraft and an origin at the spacecraft center of gravity. For simplicity, these are assumed to coincide with the primary structural axes of the spacecraft.

2.4.2 The Inertial Frame

This frame has an origin at the center of gravity of the spacecraft and translates with the spacecraft as it orbits. The i_1 axis is parallel to a line drawn from the center of the Earth through the spacecraft's perigee. The i_2 axis lies in the orbital plane and runs parallel to the spacecraft's velocity vector at perigee. The i_3 axis is perpendicular to the orbital plane and follows the right hand rule. Throughout this paper, angular rates given in the inertial frame refer to rates taken along the body axes but represent motion relative to the inertial frame. Quaternions referenced in the inertial frame represent the Euler-axis rotation from the inertial to body reference frames. The simulation software developed for this report calculates all attitude differential equations in this frame.

2.4.3 The Orbital Frame

This frame also has an origin at the center of gravity of the spacecraft and translates with the spacecraft as it orbits. The o_1 axis is collinear with a line drawn from the center of the Earth through the spacecraft's center of gravity, also known as the local vertical. The o_2 axis lies in the orbital plane and represents the local horizontal. The o_3 axis is perpendicular to the orbital plane, follows the right hand rule, and coincides with the i_3 axis. The angle between the i_1 and o_1 and

also between the i_2 and o_2 axes is equal to v , the true anomaly. Angular rates given in the orbital frame refer to rates taken along the body axes but represent motion relative to the orbital frame. Quaternions referenced in the orbital frame represent the Euler-axis rotation from the orbital to body reference frames. Since the simulation itself does not use this frame, results given in the orbital frame are shown for reference only. The following figure shows the relationship between the orbital and inertial frames.

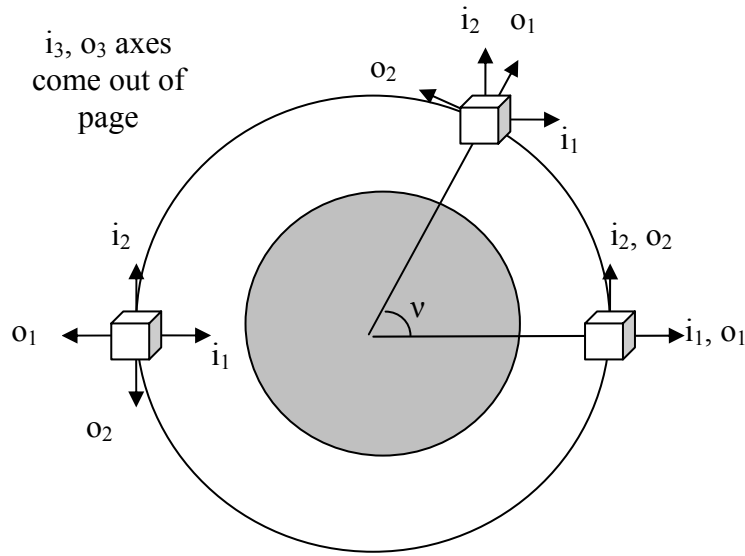


Figure 2.1: The inertial and orbital frames

2.4.4 Successive Quaternion Rotations

Since the simulation is run in inertial frame, the orbital quaternion vector represents two successive quaternion rotations. The first is from the inertial to the orbital frame and the second between the body and inertial frame. The composite rotation is given by the following equation:¹

$$\begin{bmatrix} q_1^D \\ q_2^D \\ q_3^D \\ q_4^D \end{bmatrix} = \begin{bmatrix} q_4'' & q_3'' & -q_2'' & q_1'' \\ -q_3'' & q_4'' & q_1'' & q_2'' \\ q_2'' & -q_1'' & q_4'' & q_3'' \\ -q_1'' & -q_2'' & -q_3'' & q_4'' \end{bmatrix} \begin{bmatrix} q_1' \\ q_2' \\ q_3' \\ q_4' \end{bmatrix}$$

The transformation between inertial and orbital frames is a single rotation about the 3rd axis, so the rotation quaternions are:

$$\mathbf{q}' = \mathbf{q}_{io} = \begin{bmatrix} 0 & 0 & \sin(\nu/2) & \cos(\nu/2) \end{bmatrix}^T \quad \text{and} \quad \mathbf{q}'' = \mathbf{q}_i$$

While the substitution for the reverse from and orbital to inertial quaternion is given by:

$$\mathbf{q}' = \mathbf{q}_{oi} = \begin{bmatrix} 0 & 0 & \sin(-\nu/2) & \cos(-\nu/2) \end{bmatrix}^T \quad \text{and} \quad \mathbf{q}'' = \mathbf{q}_o$$

2.4.5 Transformation of Angular Rates

Since the rates are referenced to the body axis in both the orbital and inertial frames, this transformation is actually just the subtraction or addition of the rotation rate between the orbital and inertial frames. The rotation of the orbital frame relative to the inertial frame is equal to the mean motion, or $\bar{\omega}_{oi} = [0 \ 0 \ \nu]^T$. Before this vector can be added or subtracted, however, it must be transformed into the body frame by way of the transformation matrix.¹

$${}_i\mathbf{T}_b = \begin{bmatrix} 1 - 2(q_2^2 + q_3^2) & 2(q_1q_2 + q_3q_4) & 2(q_1q_3 - q_2q_4) \\ 2(q_1q_2 - q_3q_4) & 1 - 2(q_1^2 + q_3^2) & 2(q_2q_3 + q_1q_4) \\ 2(q_1q_3 + q_2q_4) & 2(q_2q_3 - q_1q_4) & 1 - 2(q_1^2 + q_2^2) \end{bmatrix}$$

2.2

Where the inertial quaternion vector is used. The full equations for the transformations of the angular rates are given by:

$$\bar{\omega}_o = \bar{\omega}_i - {}_i\mathbf{T}_b \cdot \bar{\omega}_{oi} \quad \text{and} \quad \bar{\omega}_i = \bar{\omega}_o + {}_i\mathbf{T}_b \cdot \bar{\omega}_{oi}$$

2.5 The Equations of Motion

The Euler equations of motion for the angular velocities of a spinning, rigid-body spacecraft are:

$$\begin{aligned}\dot{\omega}_1 &= \left(\frac{I_2 - I_3}{I_1} \right) \omega_2 \omega_3 + \frac{T_1}{I_1} \\ \dot{\omega}_2 &= \left(\frac{I_3 - I_1}{I_2} \right) \omega_1 \omega_3 + \frac{T_2}{I_2} \\ \dot{\omega}_3 &= \left(\frac{I_1 - I_2}{I_3} \right) \omega_1 \omega_2 + \frac{T_3}{I_3}\end{aligned}$$

Where T represents the torques acting on the spacecraft, which can be either internal (control) or external (disturbance). The angular position of the spacecraft is represented in quaternions, and their governing differential equation is:

$$\begin{bmatrix} \dot{q}_1 \\ \dot{q}_2 \\ \dot{q}_3 \\ \dot{q}_4 \end{bmatrix} = \begin{bmatrix} 0 & \omega_3 & -\omega_2 & \omega_1 \\ -\omega_3 & 0 & \omega_1 & \omega_2 \\ \omega_2 & -\omega_1 & 0 & \omega_3 \\ -\omega_1 & -\omega_2 & -\omega_3 & 0 \end{bmatrix} \begin{bmatrix} q_1 \\ q_2 \\ q_3 \\ q_4 \end{bmatrix}$$

Together with a numerical differential equation solver, these seven equations allow the propagation of the spacecraft attitude for any time. They return the state vector in the inertial reference frame.

2.6 Attitude Disturbance Torques

The four main disturbance torques that would affect a picosatellite in LEO are magnetic, aerodynamic, gravity gradient and solar pressure in order of magnitude. The following equations were taken from Space Mission Analysis and Design (SMAD).³ The numbers shown are for 600 km orbit, which is the low side of what a CubeSat program will see. Therefore, these disturbances are worst-case.

2.6.1 Minimum Torquing Ability

As a reference for the succeeding sections, below is calculated the minimum torquing ability for the PolySat system.

$$T_{\min} = M \cdot B = nA \cdot i \cdot B_{\min} = 0.15m^2 (0.25A) 2e-5T = 7.5e-7N \cdot m$$

This is representative of one board per axis, power dropping to 250mA from the peak 300mA, and the minimum Earth's magnetic field at 600km.

2.6.2 Magnetic

This is a torque due to the magnetic field being created by the non-magnetorquer components of the satellite and includes residual magnetic field in the structure and that being generated by the operating electronic components. Since the governing equation is the same for the torque control itself, its magnitude can be related to torque ability as the ratio of the residual magnetic field to the induced dipole of the magnetorquers. The residual field was not measured, but it is reasonable to assume that it is at most one fiftieth of the torquer field.

2.6.3 Aerodynamic Drag

This is due to the drag with the atmosphere and primarily affects satellites in LEO. The maximum possible torque is given by:

$$T_{a_{\max}} = \frac{1}{2} \rho V^2 C_D AL$$

Where C_D is the coefficient of drag for a flat plate perpendicular to a free molecular flow which is approximately equal to 2-2.5. A is the cross sectional area of the spacecraft, and L is the distance between the centers of pressure and gravity. One of the CubeSat design requirements is

that the spacecraft c.g. be within 2 cm of the geometric center of the spacecraft. This number will be used here even though the actual c.g. of CP2 was considerably within this limit. Plugging in the numbers for a 600km orbit yields:

$$T_{a_{\max}} = \frac{1}{2} \left(4.89e-13 \frac{\text{kg}}{\text{m}^3} \right) \left(7550 \frac{\text{m}}{\text{s}} \right)^2 2.5 \left(0.01 \text{m}^2 \right) 0.02 \text{m} = 6.97e-9 \text{N} \cdot \text{m}$$

2.6.4 Gravity Gradient

This is due to the difference in the pull of gravity across the spacecraft. The maximum gravity gradient (GG) torque is given by:

$$T_{gg_{\max}} = (I_{\max} - I_{\min}) 3n_{\max}^2$$

Where I_{\max} and I_{\min} are the maximum and minimum principle moments of inertia and n is the orbital angular velocity of the spacecraft. Most CubeSats will be inserted into nearly circular orbits, so this term can be substituted for the mean motion.

$$T_{gg_{\max}} = \left(0.0005 \text{kg} \cdot \text{m}^2 \right) 3 \left(0.00108 \frac{\text{rad}}{\text{s}} \right)^2 = 1.75e-9 \text{N} \cdot \text{m}$$

Where the mean motion for a 600km circular orbit is used. The difference in principle inertias is estimated based on the value from the CP2 solid model ($0.0002 \text{kg} \cdot \text{m}^2$) and a factor of safety of 2.5.

2.6.5 Solar Pressure

This is a torque due to impact with solar wind. Like aerodynamic drag, it is mainly a function of the distance between the centers of pressure and gravity. The maximum torque is given by:

$$T_{sp_{\max}} = \frac{F_s}{c} A(1+r)L$$

Where F_s is solar flux (1367 W/m^2), c is the speed of light ($3e8 \text{ m/s}$), and r is the solar reflectance factor. Even substituting the improbably high reflectance factor of 0.8, the maximum possible torque is only:

$$T_{sp_{\max}} = \frac{1367 \frac{W}{m^2}}{3e8 \frac{m}{s}} 0.01m^2 (1 + 0.8) 0.02m = 1.64e-9 N \cdot m$$

2.6.6 Summary

The following table compares the results of the previous sections.

Table 2.1: Worst Case Attitude Disturbance Torques

<i>Torque Type</i>	<i>N*m</i>
Minimum Torquing Ability	7.50e-07
Residual S/C Magnetic Field	2.00e-08
Aerodynamic	6.97e-09
Gravity Gradient	1.75e-09
Solar Pressure	1.64e-09

Since these torques are all roughly two orders of magnitude smaller than even the minimum torquing ability, all but gravity gradient were not modeled in the attitude simulation.

2.7 Survey of the Field

While the use of magnetic torquing is nothing new to the satellite community, no program has yet even attempted to fly a nano- or picosatellite using solely magnetic control. Below are summarized several reports and papers that were useful in designing this system.

2.7.1 B-dot Controller

For his thesis, Kristian Svartveit of Norway's NCUBE program summarized the development and testing of their Attitude determination system.⁴ As a member of the CubeSat program, NCUBE was subject to the same size and mass restriction as PolySat. Their control system consisted of both magnetorquers and a small boom for gravity gradient (GG) stabilization. A pointing accuracy of 10° - 20° was necessary in order to use the broadband antenna they had onboard. Their system used two different magnetic control algorithms but relied entirely on the GG boom for their pointing accuracy. The first magnetic algorithm was the B-dot detumbling controller and the second would simply tip the spacecraft 90° in case it accidentally aligned with the GG boom pointed away from Earth. Their attitude determination system used a Kalman filter to reduce noise and integrate attitude information from a set of magnetometers and crude, solar panel sun sensors. While the analysis was not particularly helpful due to the addition of the GG boom, it did contain pseudo-code for B-dot which was useful for designing the algorithm used here. There was no on-orbit data in this report because it was written before the launch of the satellite.

Another CubeSat program to use B-dot was the AAU CubeSat by Aalborg University in Denmark.⁵ This team also developed constant-gain and LMI controllers for three-axis pointing stability. All of the analysis was done for periodic linear systems, however, which are not a very accurate representation of the mechanics involved. Unfortunately, contact was never made with this satellite after deployment, so no on-orbit information is available.

2.7.2 Three-Axis Controller

Several theoretical studies were found that talked about the possibility of three-axis stabilization. They were not particularly useful due to their use of supplementary non-magnetic actuators or linear analysis. The most useful information for the three-axis controller came from a report by M. Guelman about the magnetic control experiments performed on the Israeli Guerwin-Techsat.⁶ This satellite was a 50kg cube, was launched in July 1998, and successfully functioned for over 4.5 years. They had both magnetorquers and a momentum wheel onboard which was shut down for several on-orbit, full magnetic control tests. Three magnetic controllers were developed for three-axis stabilization, called the COMPASS, linear quadratic regulator (LQR), and No-Wheel controllers. The COMPASS controller used the law:

$$\bar{m} = -C_1 \left(\dot{\bar{B}}_{measured} - \dot{\bar{B}}_{expected} \right) - C_2 \left(\bar{B}_{measured} - \bar{B}_{expected} \right)$$

The No-Wheel controller, named for the complete shutdown of the momentum wheel, followed the law:

$$\bar{T}_{req} = - \left(C_1 \cdot \bar{\omega}_e + C_2 \cdot I^{-1} \cdot \bar{q}_e \right)$$

The LQR controller was not used because of its linear approximations. The COMPASS controller was tested for the PolySat system, but was found to be less accurate than a No-Wheel-type controller. This report also presented the pseudo-reverse of the cross-product from equation 2.1 that is presented later. Their tests showed that with even a very small momentum bias accuracies of 2°-2.5° were possible. Regrettably, due to a malfunction of the linear Kalman filter and the fact that the momentum wheel was not equipped with a break, they were not able to achieve fully magnetic three-axis stabilization.

3 HARDWARE

The PolySat team has designed and is refining a standardized bus that will be used on future incarnations and could be sold to or shared with other schools and companies. This bus consists of several standardized components: an aluminum structure, the CD&H board, the power board, four side panels, and a front panel (left-most face, Figure 3.1 below). The remaining face is left for a payload-specific board and there is an internal mount for another payload board.

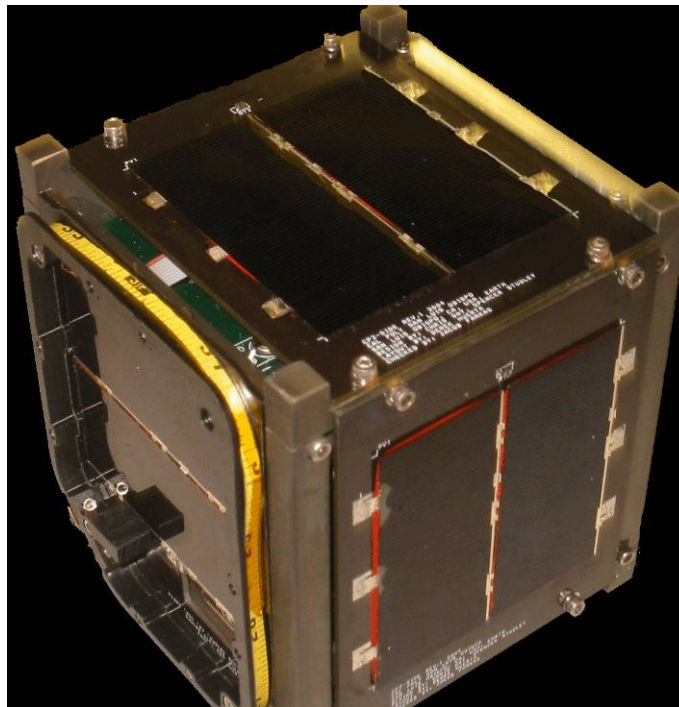


Figure 3.1: CP2 Engineering Model

3.1 Side and Front Panels

The side panels each have two solar panels, a magnetometer, magnetorquer coils, two temperature sensors, and the electronics to control all these devices. The front panel has the same equipment as the side panels with the addition of the antenna route, antenna, and holes for the remove-before-flight pin and diagnostic port. The standard configuration is for four side panels and one front panel. The sixth face could be equipped with another side panel or reserved for the payload, as is the case with CP2 and CP3.

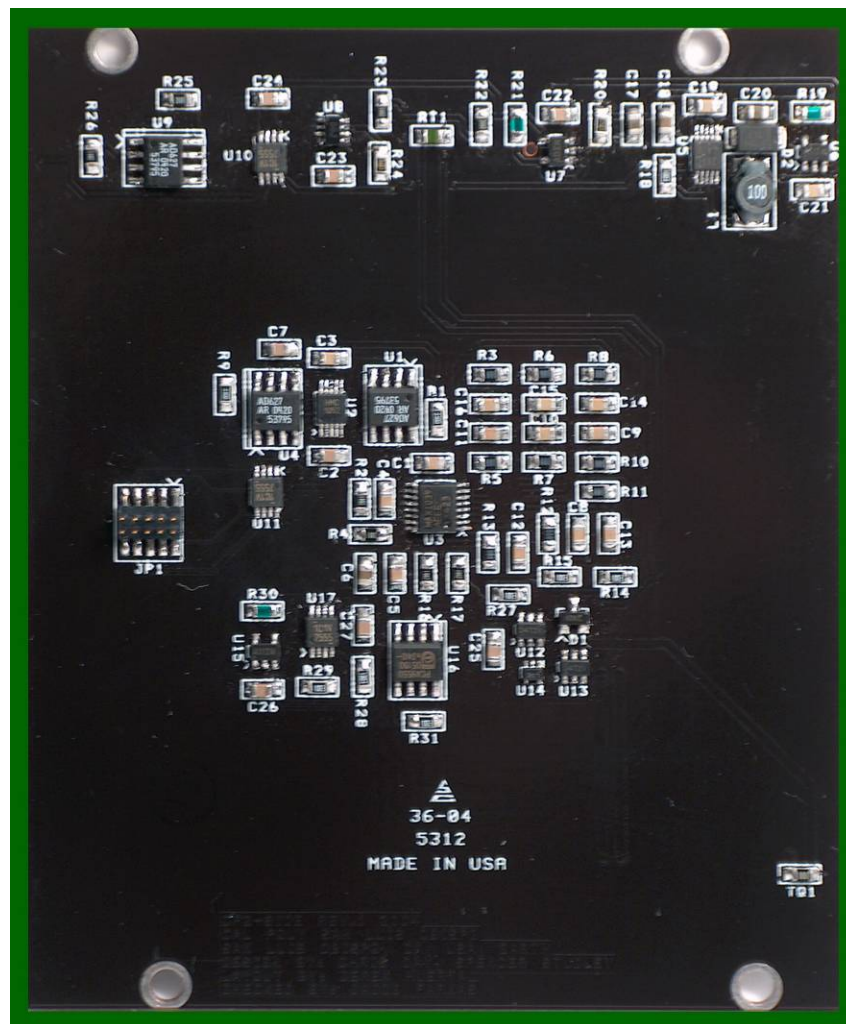


Figure 3.2: CP2 side panel interior face

3.2 Magnetometers

Each of the side panels is equipped with a Honeywell HMC 1052 2-axis magnetometer, highlighted in Figure 3.3 below. The output voltage is amplified by the op-amps on either side and digitized into an 8 bit signal. The range and offset of this signal is controlled by changing the values of the amplifier resistors. Ideally, these would be set to give the sensors a range of $\pm 500\text{mGs}$ and a resolution of 3.9mGs . Full control of the offset values for both magnetometer axes independently was not available on CP2, but the problem was corrected for the CP3 layout.

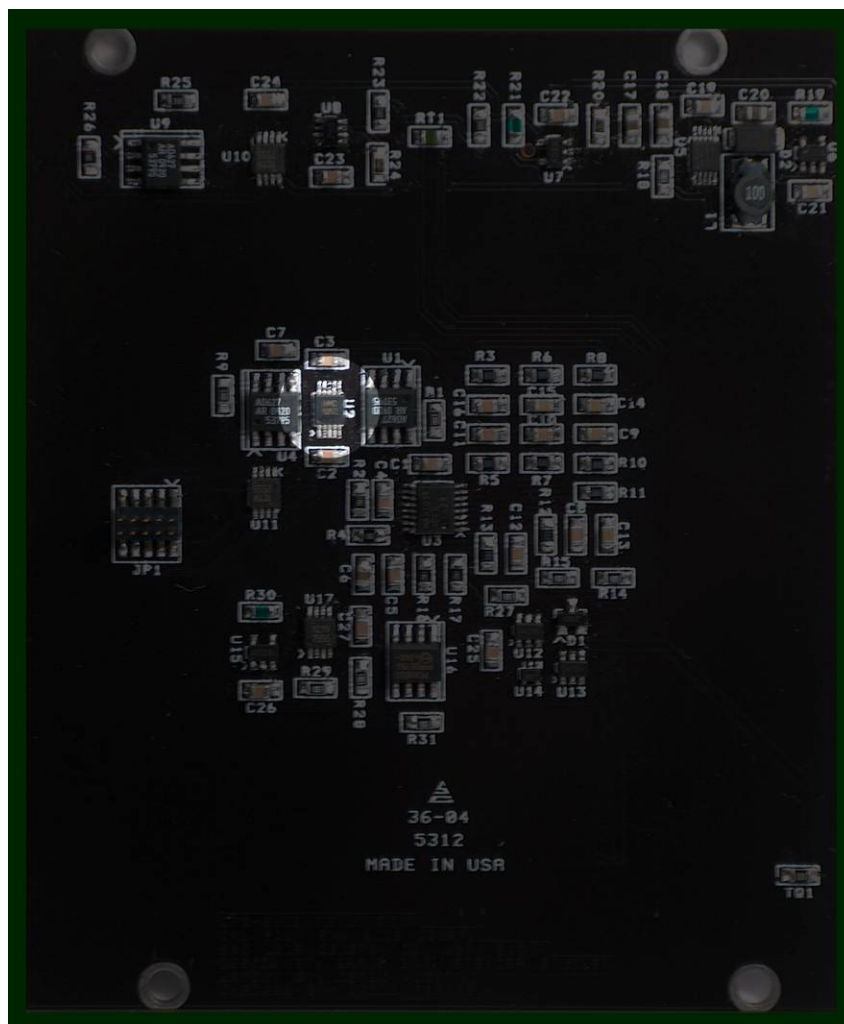


Figure 3.3: CP2 side panel with HMC 1052 magnetometer highlighted

Each side panel contains a sandwich of three layers with 18 coils each for a total of 54 turns and a total enclosed area of 0.1503m^2 . Figure 3.4 below has the approximate coil location superimposed over the panel. Note that the number of coils shown below is not correct. Current is controlled by a pulse-width modulator to provide a current of at most $\pm 300\text{mA}$. The maximum value will change depending on battery charge and power available. The current is controlled by two commands of one byte. One is for the direction and the other is the magnitude. This gives the magnetorquer current a resolution of 1.2 mA .



4 ATTITUDE SIMULATION COMPONENTS

The attitude simulation is based on a tool developed by fellow graduate student Erick Sturm called the Orbit Propagator and Attitude Simulator (OPAS). The attitude portion of this simulation was highly modified in order to implement and debug full 3-axis control of a simulated PolySat. The inertial properties of the spacecraft were taken from the IDEAS model of CP2, however, different sizes of satellite may be simulated using this tool by changing the inertias and gains appropriately. The code is reprinted in Appendix C in its entirety.

4.1 Orbit Propagator

This portion of OPAS was left largely in its original form and includes the J2, third body, and atmospheric drag disturbance terms. Results are displayed in the form of a ground track. It also calculates the magnetic field at every time step of the propagation. This information is then interpolated for every point in the attitude simulation.

4.2 Magnetic Field Estimation

The magnetic field at every point in the simulation was calculated by a MATLAB program called “magfd” developed by Maurice Tivey at the Woods Hole Marine Magnetism Group.⁷ This program accepts the spacecraft location in space and time and returns the magnetic field vector as estimated by the IGRF-10 Gaussian coefficients. Field information is calculated at each step of the orbit propagation, and linearly interpolated for intermediate points of the attitude simulation. The “magfd” code is reprinted in Appendix A.

4.3 Disturbance Torques

The only disturbance torque modeled in this attitude simulation was that of gravity gradient simply because it is very easy to implement. The Euler equations are modified in this fashion:

$$\begin{aligned}\dot{\omega}_1 &= \left(\frac{I_2 - I_3}{I_1} \right) \omega_2 \omega_3 + \frac{T_1}{I_1} - \left(\frac{I_2 - I_3}{I_1} \right) 3n^2 C_{21} C_{31} \\ \dot{\omega}_2 &= \left(\frac{I_3 - I_1}{I_2} \right) \omega_1 \omega_3 + \frac{T_2}{I_2} - \left(\frac{I_3 - I_1}{I_2} \right) 3n^2 C_{11} C_{31} \\ \dot{\omega}_3 &= \left(\frac{I_1 - I_2}{I_3} \right) \omega_1 \omega_2 + \frac{T_3}{I_3} - \left(\frac{I_1 - I_2}{I_3} \right) 3n^2 C_{11} C_{21}\end{aligned}$$

Where the C_{ii} terms come from the body-to-inertial quaternion transformation matrix of equation 2.2. Including it in the simulation had a negligible affect on the results. Its magnitude is compared with other possible disturbances in Table 2.1. Even though other disturbances are not simulated, they are of similar magnitude to gravity gradient. Since there was a negligible difference between the results with and without GG, it is probable that the other disturbances would have little effect as well.

4.4 Hardware Models

Each of the components of the ADCS introduces another level of uncertainty to the system. This is represented here by adding a normally-distributed random noise component and rounding each value to the component's resolution.

4.4.1 Magnetorquers

The magnetorquers were first simulated by assigning each component of the magnetic dipole requested to one torquer panel. These requests were converted to a current command by

equation 2.1. The current command was then limited so that no individual magnetorquer would request more than the hardware limit of 300mA. The current was limited by halving all components until they were within the maximum allowed. This method was chosen based on the advice of the software team due to the fact that a division by two is a simple bit flip in binary math. Finally, a two byte command is sent to the pulse-width modulator (PWM) that controls the torquer current. The first byte gives the current direction while the second breaks the full range from 0-300mA into 256 steps, so the current requested by the simulation was rounded off to the nearest 1.2 mA.

4.4.2 Magnetometers

The magnetometers were modeled in several different ways to test varying degrees of accuracy and methods of implementation. In the actual hardware, the voltage from the actual magnetometers is converted into a one bit number for each of the two axes that it reports. The relationship between this voltage and magnetic flux density is linear and given by the equation:

$$M = a(\text{bit value}) + b$$

4.1

Where a and b are calibration factors. With five side panels and two axes each, there are ten channels of information. This provides double redundancy on two axes and triple redundancy on the third. The reading of each of the ten magnetometers is simulated using:

$$mt_{ij} = \text{round}\left((B_i - b) / a + \sigma_{mt} * \text{randn}\right)$$

4.2

Where mt_{ij} is the j th reading of body axis i and is given in bits. *Round* is a function that rounds the reading to the nearest bit value. The last term adds a noise where σ is the standard deviation

of the noise and *randn* is a function that returns a random number with mean zero and a standard deviation of one. In other words, this simulates a reading with the correct resolution of the magnetometers and introduces a noise with standard deviation of σ . Two different versions of the calibration factors were simulated.

4.4.2.1 Ideal Calibration

In this case, it is assumed that the resistors controlling each channel of the magnetometers are appropriately sized so that each channel reports a 0 at -500 mGs and 255 at 500 mGs, which is slightly above the 480mGs that will be seen on orbit¹. With 256 steps between ± 500 mGs, this gives the magnetometers a resolution of approximately 4 mGs. The bit value is converted back to magnetic flux density using equation 4.1 and plugging in $a = 5e-5/128$ T/bit and $b = -5e-5$ T. The median is then taken of the three or four readings for each axis. This is done so that readings from any malfunctioning magnetometers on orbit would be discarded. This three-component vector is then returned to the simulation and used for the calculation of magnetorquer commands.

4.4.2.2 Real CP2 Calibration Information with B-dot Bit Calculation

This case simulates the actual way in which CP2 will calculate and execute B-dot. It differs from the previous one in that the a and b calibration values are taken from the actual test data for the CP2 flight side boards. The calibration data are given in Appendix B and were taken in a very rough manner not intended for attitude extrapolation. Since these data are not stored onboard CP2, this method also differs in that the bit values are not converted back into magnetic

flux values. Accuracy is decreased because each magnetometer has a different range and offset which could conflict with each other. As before, the median is then taken of the three or four readings for each axis. The goal of this version is to demonstrate that readings from magnetometers with different zero points, ranges, and resolutions can still be combined for effective control.

4.4.3 Other Possible Attitude Determination Hardware

In order for the three-axis control algorithm to function, full knowledge of the spacecraft position and rates is required. Several methods are under consideration for the CP3 project including an extended Kalman filter for the magnetometer data, gyros, star trackers, and sun sensors. These would be mounted on the payload board or payload face. In order to maintain generality and since the final architecture had not yet been decided at the time of writing, the simulated quaternions and rates were modified with an arbitrary noise and resolution as shown below.

$$\omega_i = \text{round}\left(\omega_{i_{\text{exact}}} + \sigma_{\omega} \cdot \text{randn}, \delta\omega\right)$$

$$q_i = \text{round}\left(q_{i_{\text{exact}}} + \sigma_q \cdot \text{randn}, \delta q\right)$$

4.3

Where the σ 's are the standard deviation of the noise and the round function rounds the reading off to the nearest step of the resolution, $\delta\omega$ or δq . Rather than plug in given values, this report will examine what noise levels and resolutions are required for convergence of the three-axis algorithm.

4.5 B-dot Detumbling Algorithm

The calculation of B-dot itself was done by a simple backwards difference method:

$$\hat{\mathbf{B}} = \frac{\mathbf{B}^t - \mathbf{B}^{t-\delta t}}{\delta t} \quad \mathbf{M}_{req} = -K \cdot \hat{\mathbf{B}}$$

4.4

Where the gain was found through trial-and-error by decreasing its value until the system the fastest settling time was reached. As described in Section 4.4.2.2, on CP2 the values for B and B-dot are calculated as unitless bit values, whereas the preferable method is to convert each magnetometer reading into tesla prior to calculation of B-dot. As written for CP2, the inputs for the B-dot command are the total run time, gain, time between readings, wait time, and torquer pulse time.

4.6 Three-Axis Control Algorithm

The more complicated of the control algorithms, full control in three axes requires accurate attitude knowledge to function correctly. The algorithm itself is just a simple rate and position feedback similar to the one used on the Gurwin-Techsat⁵:

$$\vec{T}_{req} = -\mathbf{I}(C_1 \cdot \vec{\omega}_e + C_2 \cdot \vec{q}_e)$$

Where T_{req} is the requested torque, C_1 and C_2 are gains, and ω_e is the error in angular velocity. The equation is multiplied by \mathbf{I} , the principle moment of inertia vector, in order to size each torque appropriately to the axis about which it is torquing. Rather than the entire quaternion, the vector q_e is the first three components of the quaternion error vector, which approximate the Euler angles for small angles. The entire vector is given by the equation:⁸

$$\mathbf{q_e} = \begin{bmatrix} q_{d4} & q_{d3} & -q_{d2} & -q_{d1} \\ -q_{d3} & q_{d4} & q_{d1} & -q_{d2} \\ q_{d2} & -q_{d1} & q_{d4} & -q_{d3} \\ q_{d1} & q_{d2} & q_{d3} & q_{d4} \end{bmatrix} \begin{bmatrix} q_{a1} \\ q_{a2} \\ q_{a3} \\ q_{a4} \end{bmatrix}$$

4.5

Where q_d is the desired vector and q_a is the actual quaternion. When the desired vector was given in the orbital frame, it was converted to the inertial frame at each time step and then input into the quaternion error equation above. Since the frames are rotating relative to each other, this meant that the desired quaternions would oscillate as the system settled out to a constant rotation in the inertial frame. Refer back to sections 2.4 for this transformation procedure.

The next step is to convert the desired torque vector into a magnetorquer command. As mentioned in Section 2.2, the torque cannot be commanded directly since the possible torque vector is always perpendicular to the magnetic field. Instead, the magnetic dipole is requested using⁵:

$$\vec{M}_{req} = \frac{\vec{B} \times \vec{T}_{req}}{|\vec{B}|^2}$$

4.6

This equation saves power by only torquing the portion of the requested vector perpendicular to the magnetic field and is a best-fit approximation of the reverse of the cross-product from equation 2.1.

4.7 Computation

The flow of the attitude simulation portion was written in order to mimic the computational flow onboard the actual satellite as much as possible. The main controller parameters are those of the gains (K for \dot{B} and C_1 and C_2 for three-axis) and the pulse length, δt . The pulse length defines both the time between magnetometer readings and the time that the torquers are pulsed for before the cycle is repeated. A complete controller cycle consists of:

1st reading \rightarrow Wait $\delta t \rightarrow$

2nd reading \rightarrow Wait 0.1 sec for torque command calculation \rightarrow

Turn on torquers \rightarrow Wait $\delta t \rightarrow$

Turn off torquers \rightarrow Wait 0.1 sec for torque field to die out

The 0.1 seconds after the second magnetometer reading was set in order to simulate the time it might take the processor to handle the attitude information and calculate the necessary current commands. The 0.1 sec after torquing was determined from experimental data for the magnetometer readings. It was found that magnetometer readings taken immediately after pulsing the torquers were greatly skewed by the residual magnetic field, but even a small buffer such as this was sufficient to allow the induced field to dissipate.

4.8 Summary of Simulation Assumptions

While an attempt was made to make the simulation as real as possible, a point of diminishing returns must be considered when eliminating assumptions. Consequently, several approximations were kept in the simulation. They are:

- The spacecraft is a rigid body.
- The principal inertial and structural axes coincide.
- Disturbance torques other than gravity-gradient are negligible.
- The power subsystem is always capable of providing 300mA per torquer.
- There is a properly functioning attitude determination system in operation.
- Sensors are properly calibrated and mounted, i.e. there is no misalignment or offset error.
- Command computation needs can be met in 0.1 seconds.

5 ATTITUDE SIMULATION RESULTS

This section summarizes and analyzes the results from the hundreds of simulations run to explore the capabilities of a magnetically controlled CubeSat. These simulations were run for anywhere from one to seven orbits or 95 to 665 minutes. The orbit propagator outputs a ground trace which is shown below for five orbits.

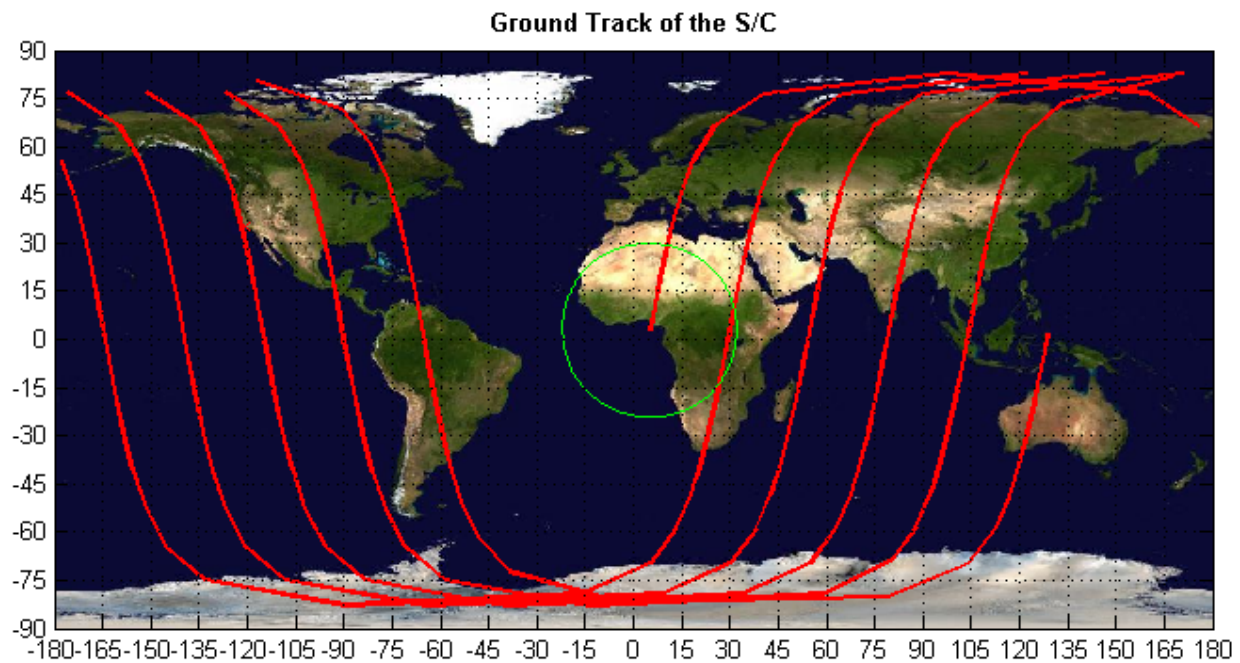


Figure 5.1: Ground track for 5 orbits

This figure shows the orbit simulation starting over the equator near Indonesia, sweeping over the poles several times and stopping off the west coast of Africa. The green circle represents the ground area with a line-of-sight to the satellite. The spacecraft is in a sun-synchronous orbit and processes across the Earth with each new orbit.

5.1 *B-dot Detumbling*

Many simulations were run in order to optimize the two main control parameters, the gain from equation 4.4 and the pulse length. After these were found, many more simulations were run to analyze the system's performance under less than ideal conditions. The failure modes that were analyzed were those of high tip-off velocities, noisy magnetometer readings, and torquer failure. Additionally, the B-dot calculation methods of CP2 and CP3 were compared.

5.1.1 Explanation of B-dot plots

The results of each simulation are summarized in a single figure divided into six subplots which are lettered from a-f. The x-axis of all plots is given in minutes. One may use the orbital period of approximately 95 minutes to convert these values to fractions of an orbit. With the exception of the quaternions, the lines within each subplot represent Cartesian axes and are colored according to:

Axis 1: Blue

Axis 2: Green

Axis 3: Red

Axis 4: Cyan (for the fourth quaternion or magnitude of the angular velocity only)

An explanation of each subplot follows:

- a) *Magnetic Field in the Orbital Frame* displays the components of the magnetic field found in the orbit propagator by magfd (see Section 4.2).
- b) *Magnetic Field in the Body Frame* shows the magnetic field components seen by the sensors. The gray lines represent the values measured by the spacecraft and include any noise terms.

- c) *B-dot* shows the values calculated by the B-dot algorithm.
- d) *Torquer Current Provided* relates to B-dot by a factor of K/nA but is also bound by the current limiter described in Section 4.4.1.
- e) *Inertial Angular Rates* are the actual simulated values. These are given as a reference and not used in the control algorithm. See Section 2.4.2 for a definition of the frame.
- f) *Inertial Quaternions* are the actual simulated values shown for reference.

5.1.2 Optimum Gain Determination

The optimum gain was found by simulating a range of values and selecting the one that settled the fastest. These simulations were run for $1\frac{1}{2}$ orbits and had minimal noise in the magnetometer readings. The initial angular velocities were set at $\omega = [0.1 \ -0.05 \ 0.05]^T$ which is approximately 1 rpm about the b_1 axis. The pulse lengths were set to ten seconds. There were three types of unstable behavior: complete instability, instability starting at the North Pole, and instability localized to the North Pole. These distinctions were due to the fact that the effective gain changes with the fluctuation of the local magnetic field, which is the strongest at the North Pole. The first—complete instability—occurred for gains of about $1.7e5$ and higher. Figure 5.2 below shows the results of this simulation.

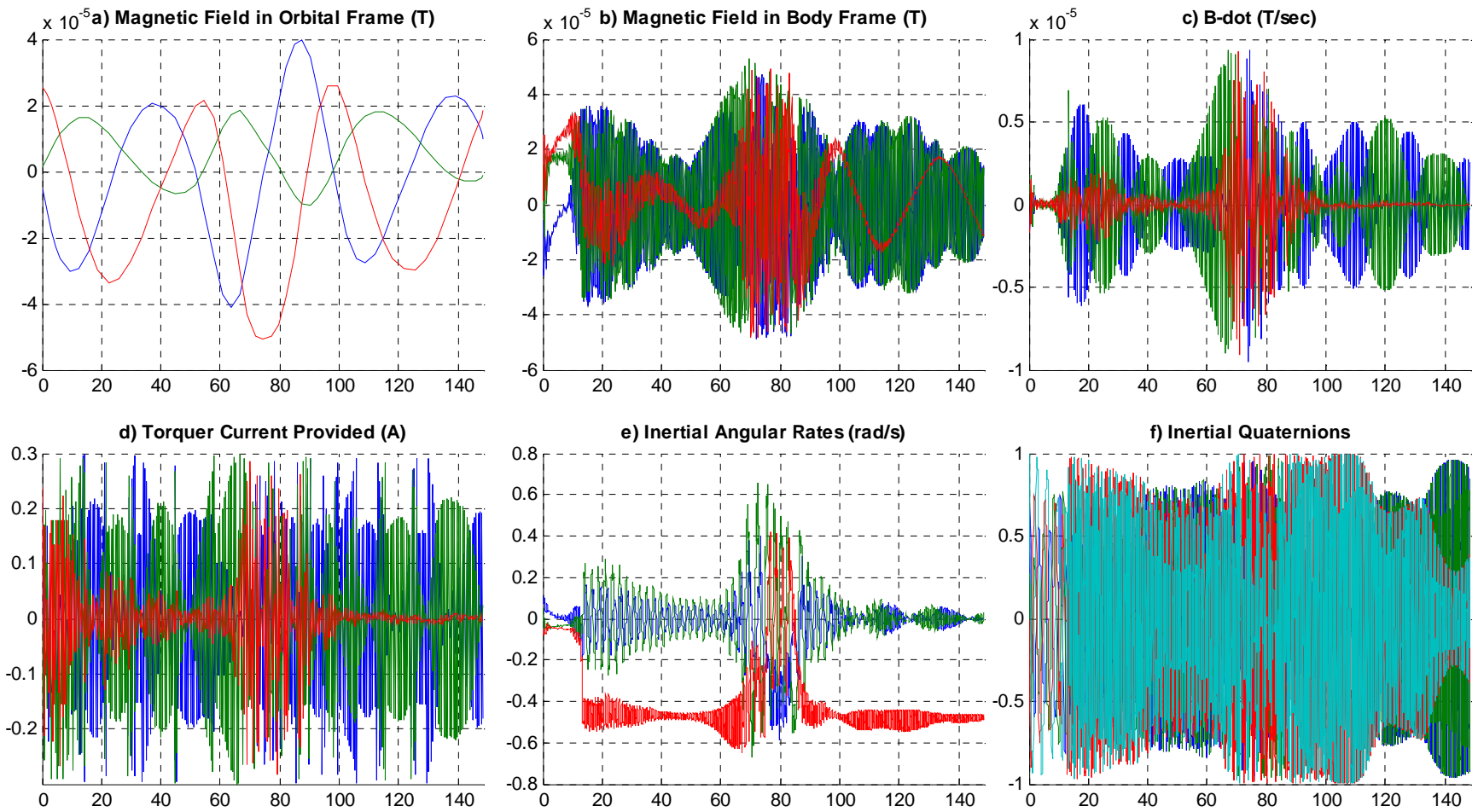


Figure 5.2: B-dot for 1.5 orbits with $K = 17e4$ and $\delta t = 10\text{sec}$

Plot d) shows that the gain is so high that magnetorquer current is being clipped for the entire simulation. Even so, B-dot reduces the angular velocities initially, but then some disturbance sends it spinning about the major inertial axis, b_3 . The additional instability around 70 minutes corresponds to a peak in the magnetic field as shown in plot a). This peak occurs as the satellite transits the North Pole and is further examined in the following simulation.

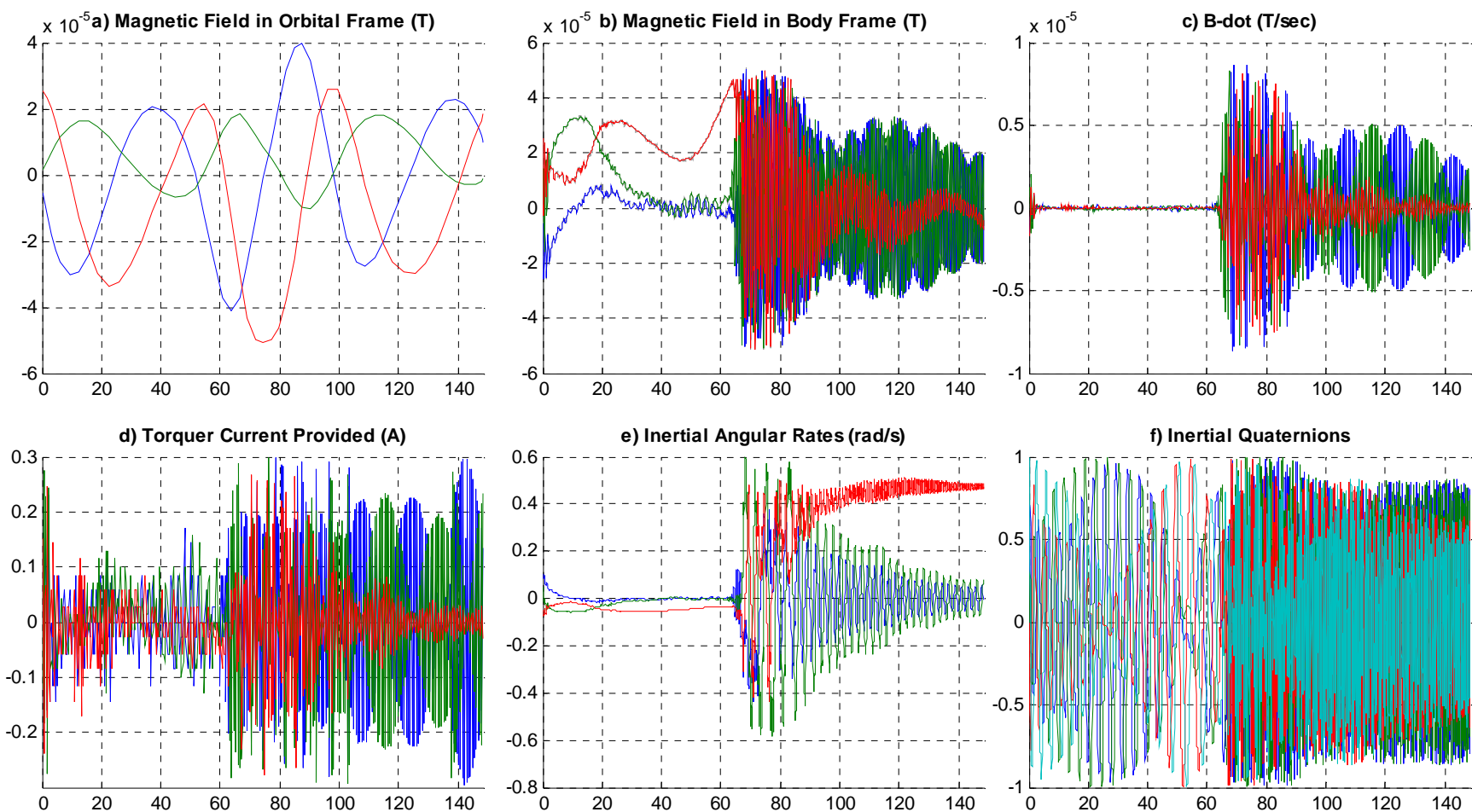


Figure 5.3: B-dot for 1.5 orbits with $K = 11e4$ and $\delta t = 10\text{sec}$

The second instability case occurs for gains between approximately $1.1e5$ and $1.7e5$. The satellite initially settles but then diverges as near the pole. Not only is the field strength highest here, but also its rate of change of direction. At this point the torquers have become saturated and the angular velocities too great for the system to recover. Again, the spacecraft spins about the major axis.

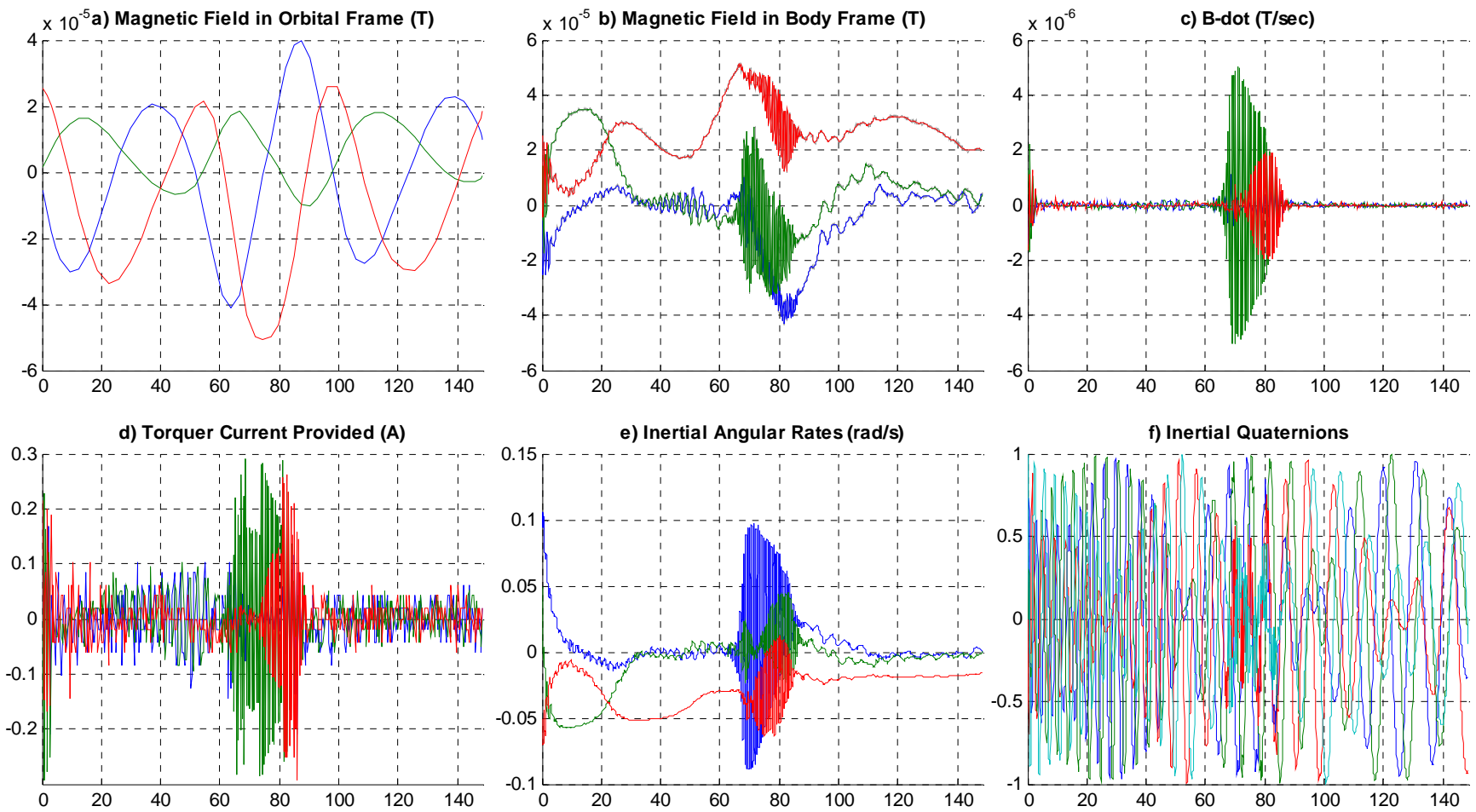


Figure 5.4: B-dot for 1.5 orbits with $K = 8e4$ and $\delta t = 10\text{sec}$

In this case the rates only explode near the pole, but do not diverge enough that the system cannot recover. Gains lower than about $7e4$ converged at all points in the orbit; however, it was found that the maximum stable gain did not converge the fastest. The optimum gains were found to be between $2.5e4$ and $1.5e4$. Figure 5.5 below shows the results for a gain of $2e4$.

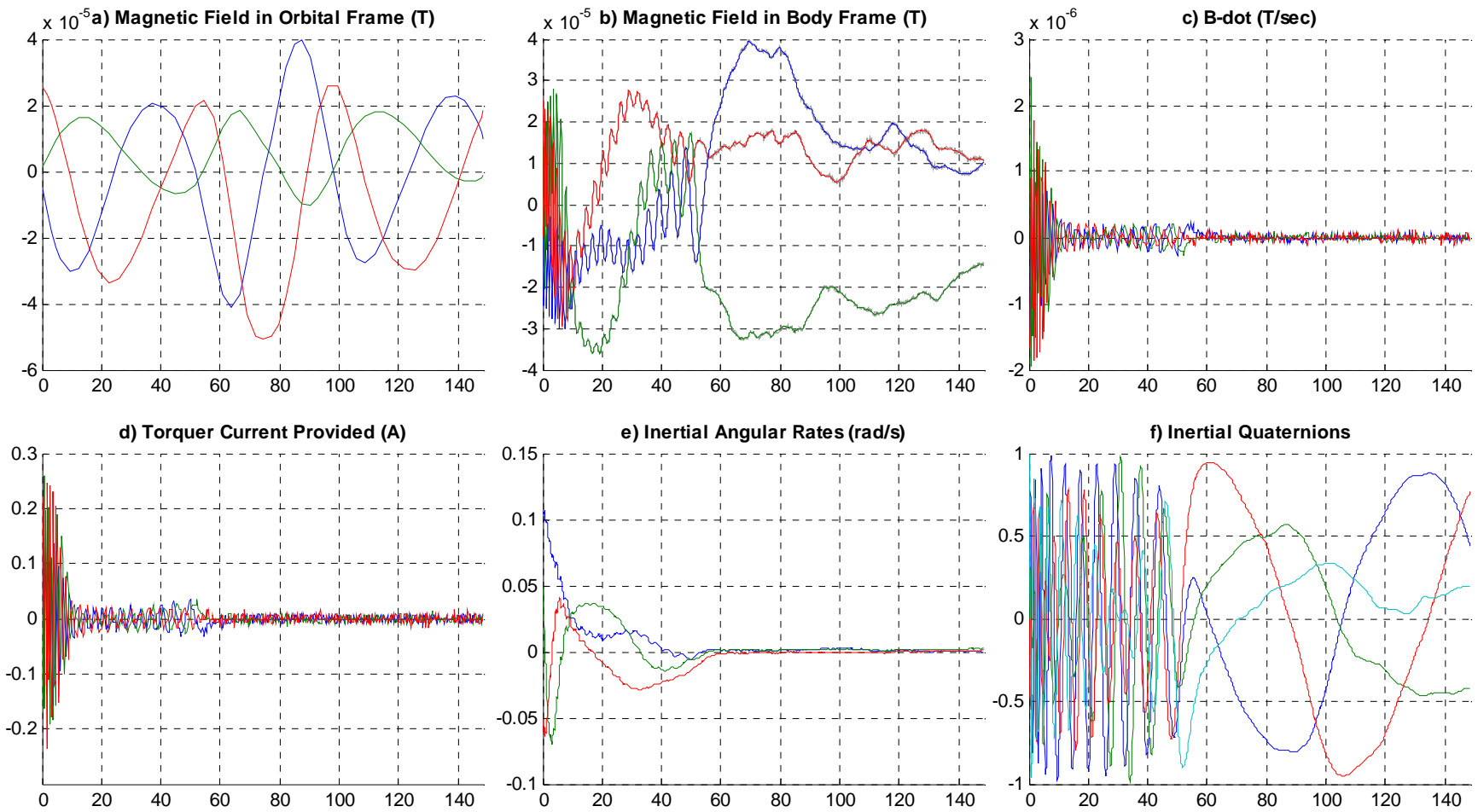


Figure 5.5: B-dot for 1.5 orbits with $K = 2e4$ and $\delta t = 10\text{sec}$

The center of the optimum gain range was selected to allow for margins on either side. At this gain, the system settles after approximately 70 minutes and then maintains an angular velocity of about $2.5e-3$ to $3e-3$ rad/s (0.14 to 0.17 deg/s). The magnetic field vector itself rotates twice per orbit, giving it an average angular velocity of about 0.13 deg/s. This indicates that B-dot is

performing very near the limit of its capability at this gain value. It was found that modifying the other controller parameters had very little effect on the optimum gain setting, so a gain of $2e4$ was used for the remainder of these experiments.

It is important to note that these gain values are highly dependent on the mass moment of inertia of the spacecraft and should be recalculated for different configurations. The only consequence of having the gain set too low is a proportional increase the settling time. Additionally, it was found that stability can be improved for higher gains by decreasing the pulse time. The gain with the fastest settling time, however, was well within this stability limit, so that is not a valid reason to decrease pulse time. The relationship between pulse time and the maximum stable tip off velocity is the subject of the next section.

5.1.3 Optimum Pulse Time Determination

While the gain is more directly related to the speed with which the system settles, the maximum rotational velocity from which \dot{B} can recover is directly related to pulse length. \dot{B} essentially assumes that the rate of change of the magnetic field does not change between the field reading interval and the pulsing interval. As the actual rotation of the spacecraft increases, this assumption becomes less valid until the nonlinearity makes the system unstable. This problem is easily solved by decreasing the interval time, δt , so that the assumption is once again valid. On the other hand, a larger interval time means less demand on the spacecraft's processor time, so these two design constraints must be traded.

For this investigation, the tip-off velocity was increased in 1 rpm increments and then the pulse length shortened until the system converged. Now that the optimum gain has been found, all of these simulations could be shortened to one orbit. The initial rates were $[x \ -0.05 \ 0.05]$ rad/s where x is the test, tip-off velocity about the b_1 axis and the other two represent perturbation velocities. CubeSat's investigations into its P-POD deployment system indicate that the most probable maximum deployment rotation would be no greater than 1 rpm, so this was the first point investigated.

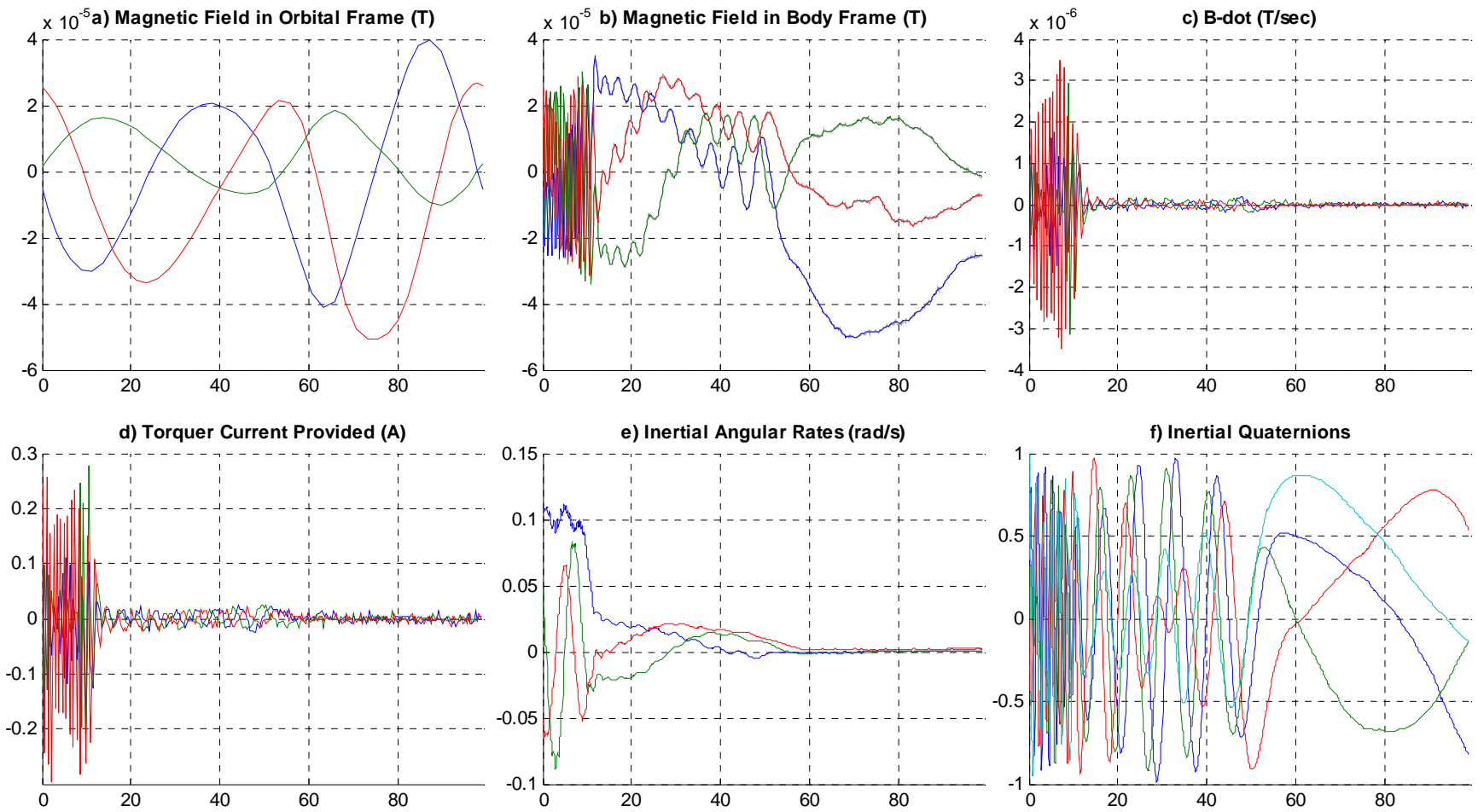


Figure 5.6: B-dot for 1 orbit with $\delta t = 12$ sec and $\omega_0 = 1$ rpm

Given an initial velocity of 1 rpm, the largest interval for which the rates settle was found to be 12 seconds and the results are shown above. As before in Figure 5.5 the rates settle within about 70 minutes, so this illustrates that δt has little effect on settling time. Several more simulations were run at increasing velocities until a δt of one second was no longer sufficient to settle.

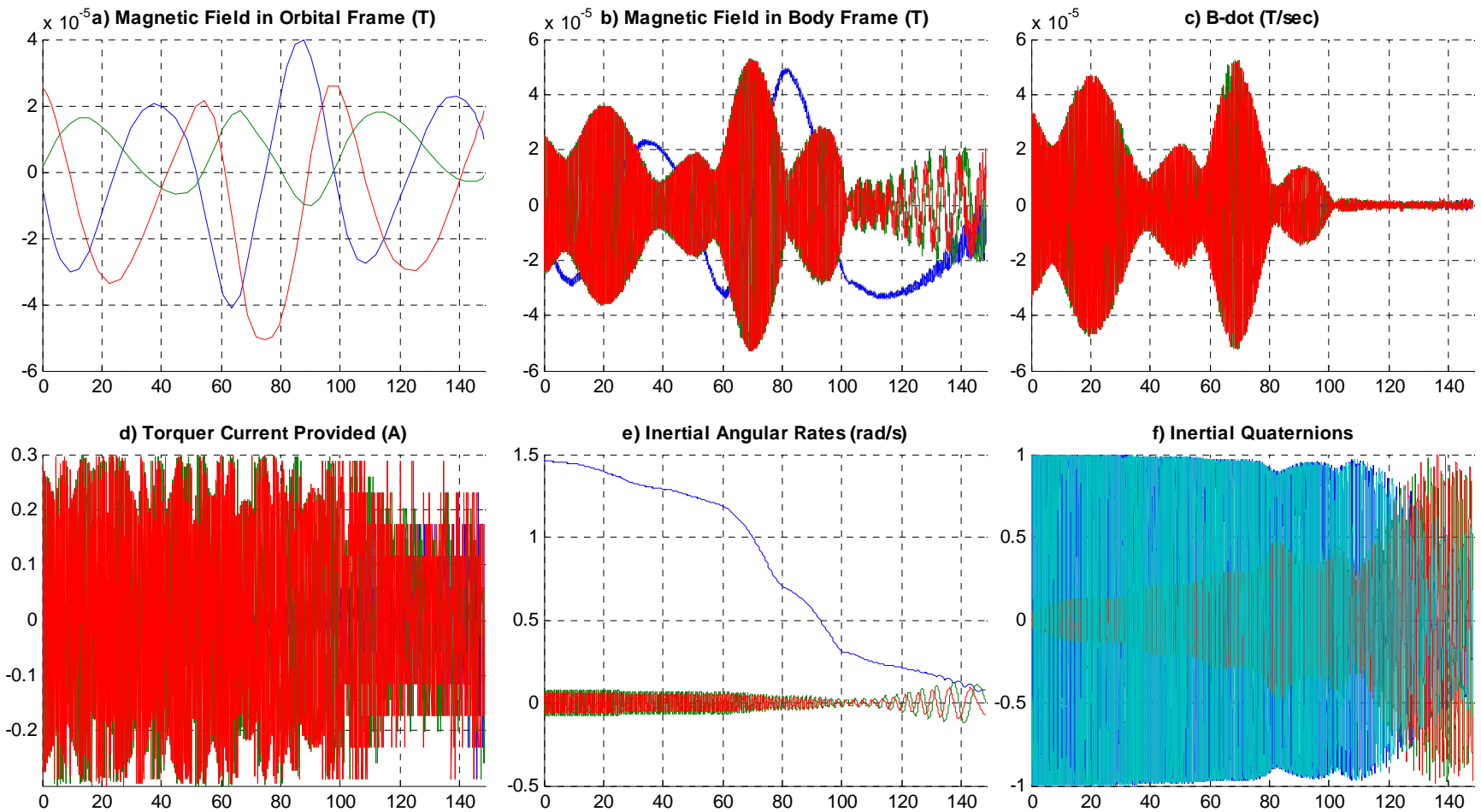


Figure 5.7: B-dot for 1.5 orbit with $\delta t = 1\text{sec}$ and $\omega_0 = 14\text{ rpm}$

It was found that if the calculations could be done once every second, B-dot is capable of handling tip-off velocities of as high as 14 rpm. That is one revolution every 4.3 seconds, which is way beyond anything that the satellite would ever see. There was an increase in settling time to the fact that the torquers are saturated while the angular velocity is above approximately 0.2 rad/s.

The results for the intermediate simulations are summarized in the following chart.

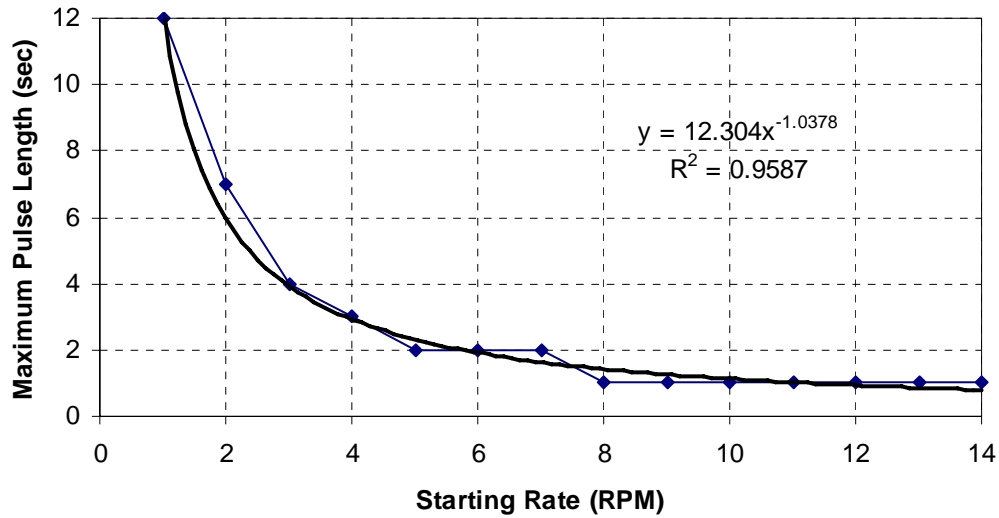


Figure 5.8: B-Dot Tip-off Velocity Performance

This chart shows what the maximum pulse length for which the system will settle given some initial velocity. The data roughly follow a power series trend which is also shown on the plot. All of these simulations settled in around 70 minutes to around 0.003 rad/s. As shown above, decreasing the pulse length has very little benefits early on but allows for extreme initial velocities if intervals of one or two seconds can be achieved. The initial velocity and pulse length have practically no effect on the final settling velocity, and the settling time is increased only for initial velocities of approximately 7 rpm and higher. The pulse length only benefits the maximum initial velocity and does not matter as long as the initial velocity is below the maximum. For example, if a pulse length of two seconds were chosen, but the satellite only experienced a tip-off velocity of 1 rpm, it would still settle as shown below.

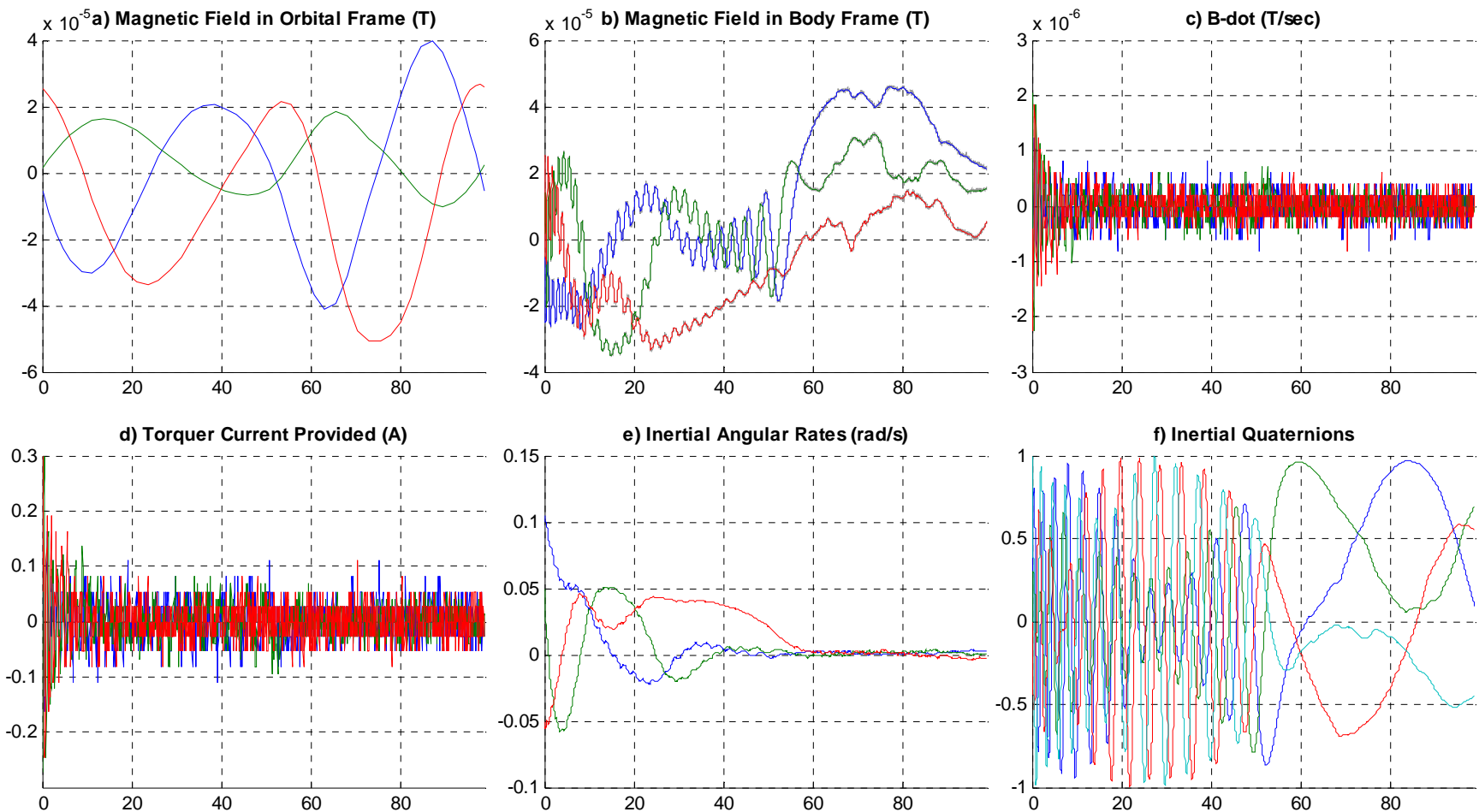


Figure 5.9: B-dot for 1 orbit with $\delta t = 2\text{sec}$ and $\omega_0 = 1\text{ rpm}$

Compare this plot to the 12 second pulses of Figure 5.6. While the settling time is unaffected, the B-dot calculated is much larger overall, which means a larger current draw. The short time between magnetometer readings means that the magnetic field has not changed significantly. Since their resolution is limited to around $4\text{e-}7\text{ T}$, the short pulse lengths introduce extra noise to the signal.

Based on these factors, the optimum pulse length was found to be the 10 seconds that had been used previously. This allows a 22% margin of what the spacecraft can handle over the maximum probable 1 rpm, while still generating a relatively noise-free B-dot signal. If it does not appear to be settling on orbit, the pulse length could always be shortened.

5.1.4 Effect of Magnetometer Noise

During the extensive hardware tests performed for this report, it was found that the magnetometers themselves were practically noise free. The simulation of noise here represents magnetic interference from the operating components of the spacecraft. On the proposed CP3 satellite, the bias would be minimized by performing the final magnetometer calibration on a complete and powered satellite. The experiment was run by increasing the value of the standard deviation of the noise, σ , from equation 4.2 while holding the gain at the optimum $2e4$.

The first step is to determine what the effect of noise is. It was suspected that the noise only had affected the final settling rates and not settling time or stability, and this was confirmed for reasonable noise levels. Figure 5.10 below show a simulation with a 7rpm tip-off velocity and σ at 20 bits ($\sim 8e-6$ T).

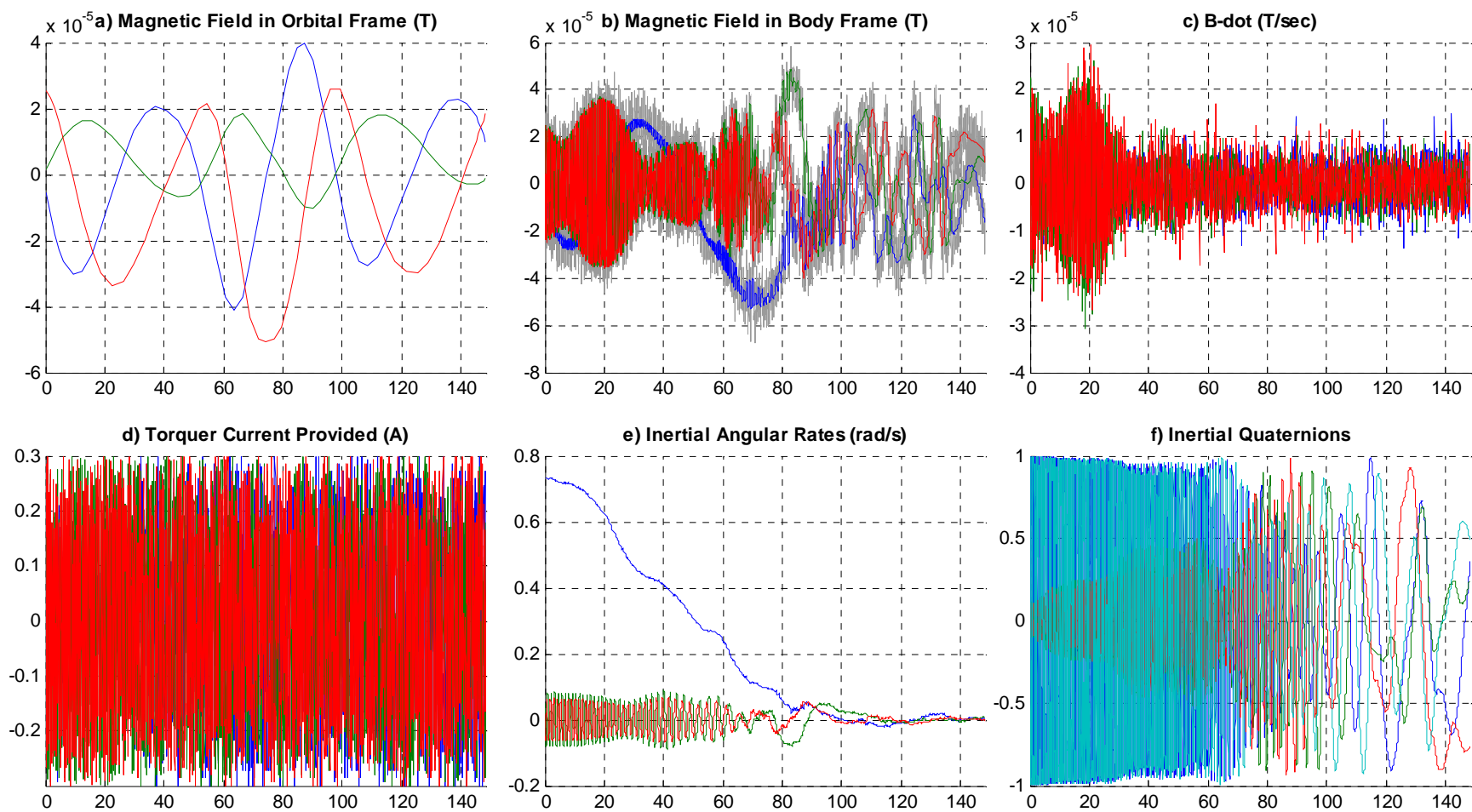


Figure 5.10: B-dot for 1 orbit with $\delta t = 2\text{sec}$, $\omega_o = 7\text{ rpm}$, $\sigma = 20\text{ bits}$

This figure demonstrates B-dot's ability to settle from very high velocities with signal-to-noise (S:N) as high as 4:1. The noise drives B-dot to continually oscillate about its settling point, causing a dramatic increase in power consumption and settling rates.

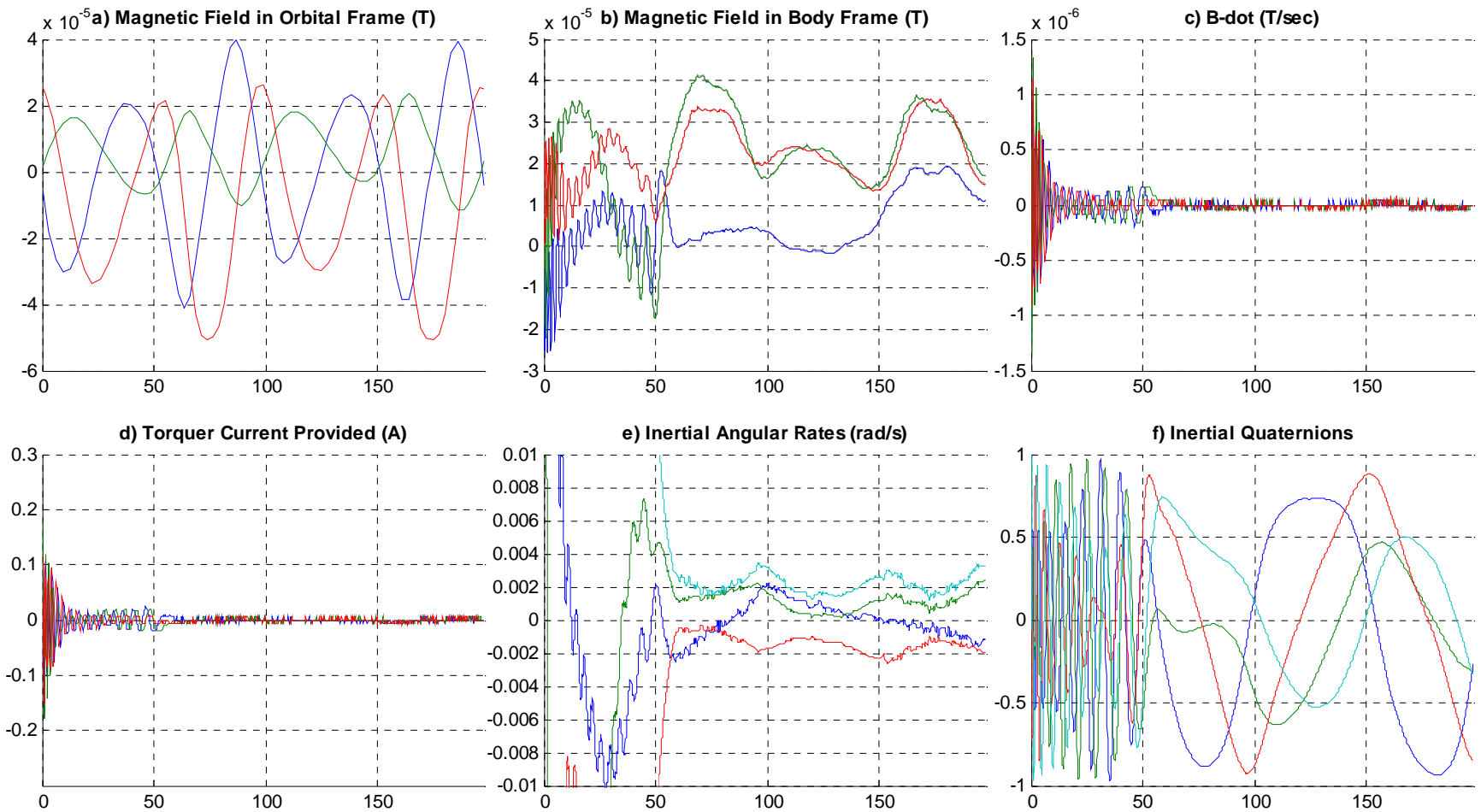


Figure 5.11: B-dot for 2 orbits with $\delta t = 10\text{sec}$, $\omega_0 = 0.5\text{ rpm}$, $\sigma = 0\text{ bits}$

This plot shows the best-case, no-noise condition for comparison. For this analysis, plot e) was modified to include a plot of the magnitude (teal), and the limits were shrunk to zoom in on the settling rates. After about 60 minutes, the spacecraft is tracing the angular rate of the magnetic field vector, which averages 0.0022 rad/s with peaks at the poles. The current draw is also very minimal.

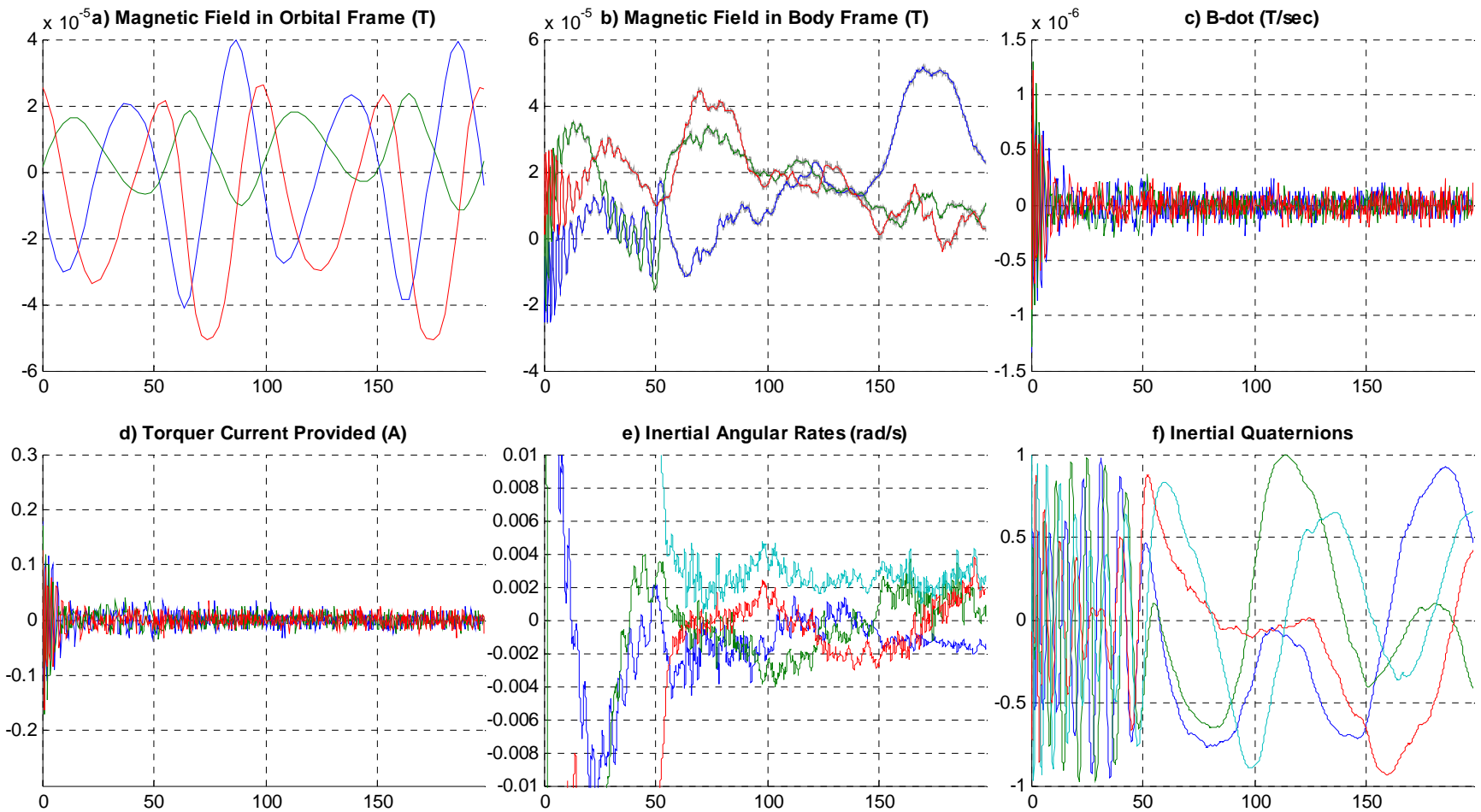


Figure 5.12: B-dot for 2 orbits with $\delta t = 10\text{sec}$, $\omega_0 = 0.5\text{ rpm}$, $\sigma = 2\text{ bits}$

In this simulation a small error with $\sigma = 2\text{ bits}$ ($\sim 8\text{e-}7\text{ T}$) was introduced. While the satellite still follows the magnetic field, the average is closer to 0.003 rad/s (0.17 deg/s) and current consumption is up 2-3 times. If the noise is above about 6 bits, the noise component becomes larger than the fluctuation of the field, and the spacecraft stops tracing the magnetic field.

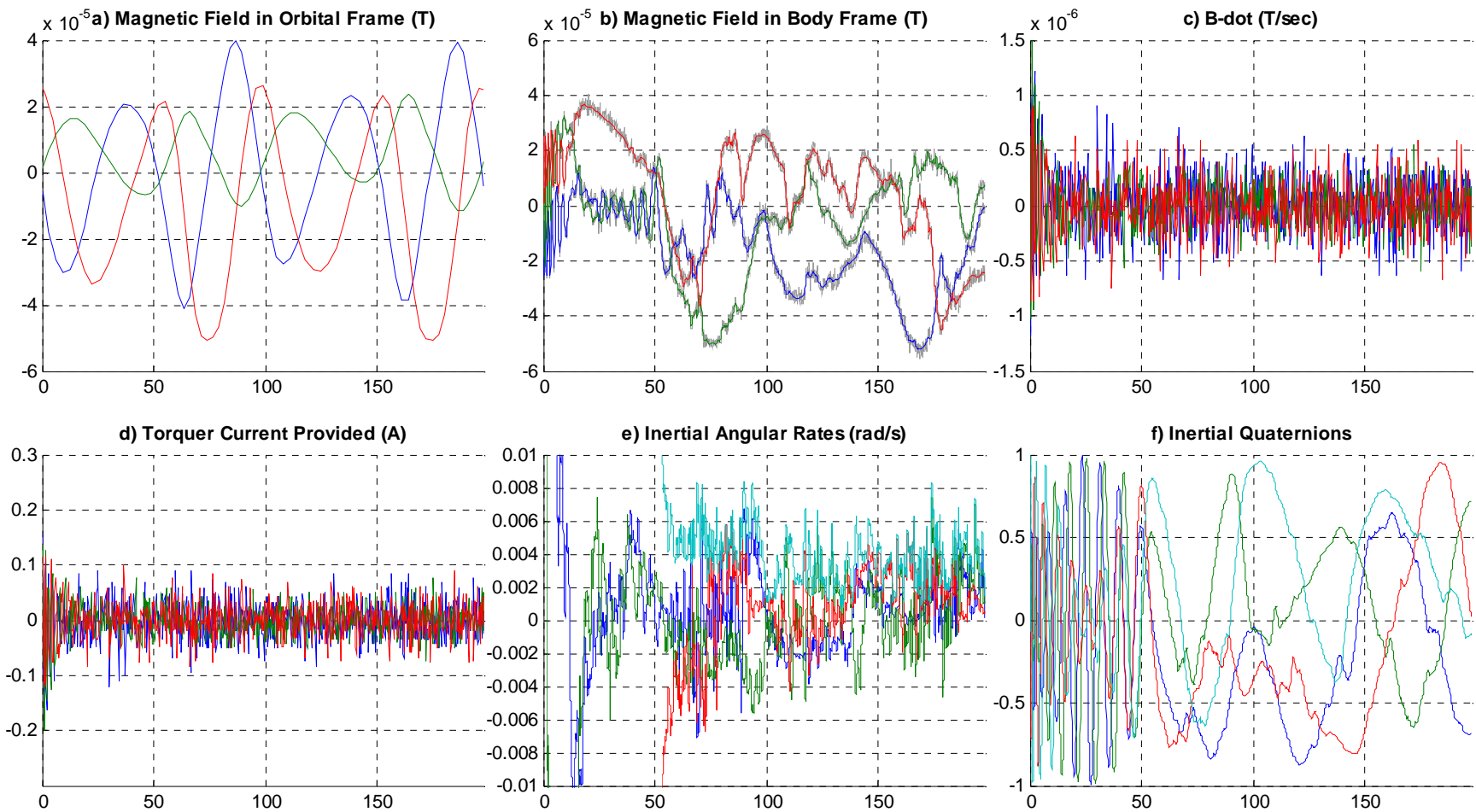


Figure 5.13: B-dot for 2 orbits with $\delta t = 10\text{sec}$, $\omega_0 = 0.5\text{ rpm}$, $\sigma = 6\text{ bits}$

At this point, it is difficult to make out the oscillation of the field and the noise has increased the settling velocity to around 0.004 rad/s (0.23 deg/s). Increases past this point were found to have a fairly linear relationship between settling velocity and noise level. The results of these simulations are summarized in below

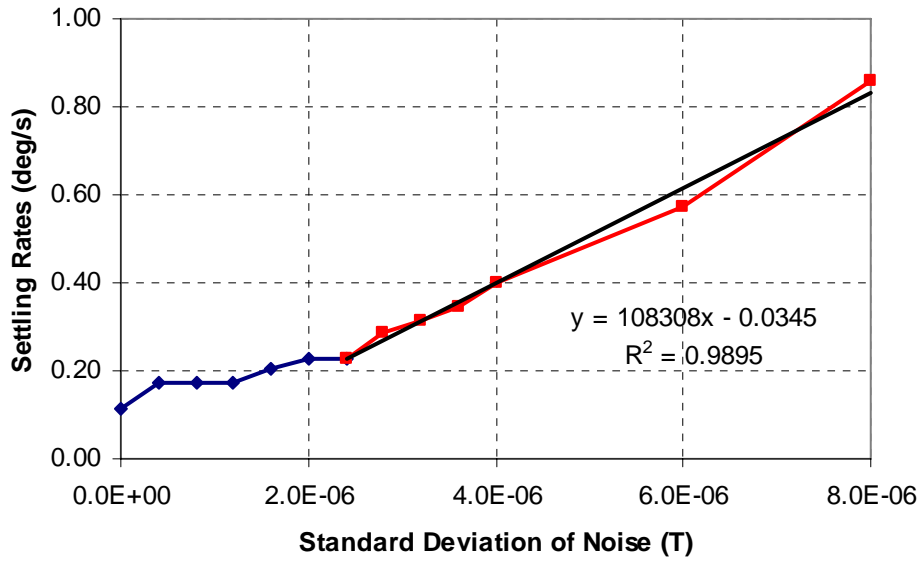


Figure 5.14: Noise level vs. average settling rates

The graph shows the fairly strong linear relationship between noise and settling rate for standard deviations above 6 bits (2.4×10^{-6} T or S:N $\sim 7:1$). As mentioned earlier, this represents the transition when the noise levels supersede the fluctuation of the local magnetic field as the largest component of B-dot.

Because the rate of change of the magnetic field fluctuates through the spacecraft orbit, performance can be improved by using a simple convergence test algorithm. This would examine the value of B-dot and terminate control when some minimum value was reached. In practice, noise limits the effectiveness of this approach; however, it can be mitigated by averaging the values of B-dot over several time steps. It was found that velocities of 0.0017 rad/s (0.10 deg/s) could be achieved for a low-noise simulation. For higher noise levels, this method reduced the settling velocity from 0.01 rad/s (0.57 deg/s) to 0.0035 (0.20 deg/s) at a noise level of 15 bits (6×10^{-6} T or S:N $\sim 3:1$). The algorithm is based on the idea that even with high levels of noise the system will randomly settle out to a low velocity eventually.

5.1.5 One and Two Torquers Out Performance

This section investigates how well B-dot performs in case one or more torquers fail and the problem goes undetected. Since there is redundancy on two of the control axes, should one torquer fail the redundant torquer could be activated to make up for it. While no system settled with only one active torquer, it was found that settling possible with two active torquers at a small sacrifice in settling time. Figure 5.15 below shows the results of a simulation with a faulty torquer on the b_1 axis. The results below still show the current values that the system is attempting to provide to the inactive torquer(s).

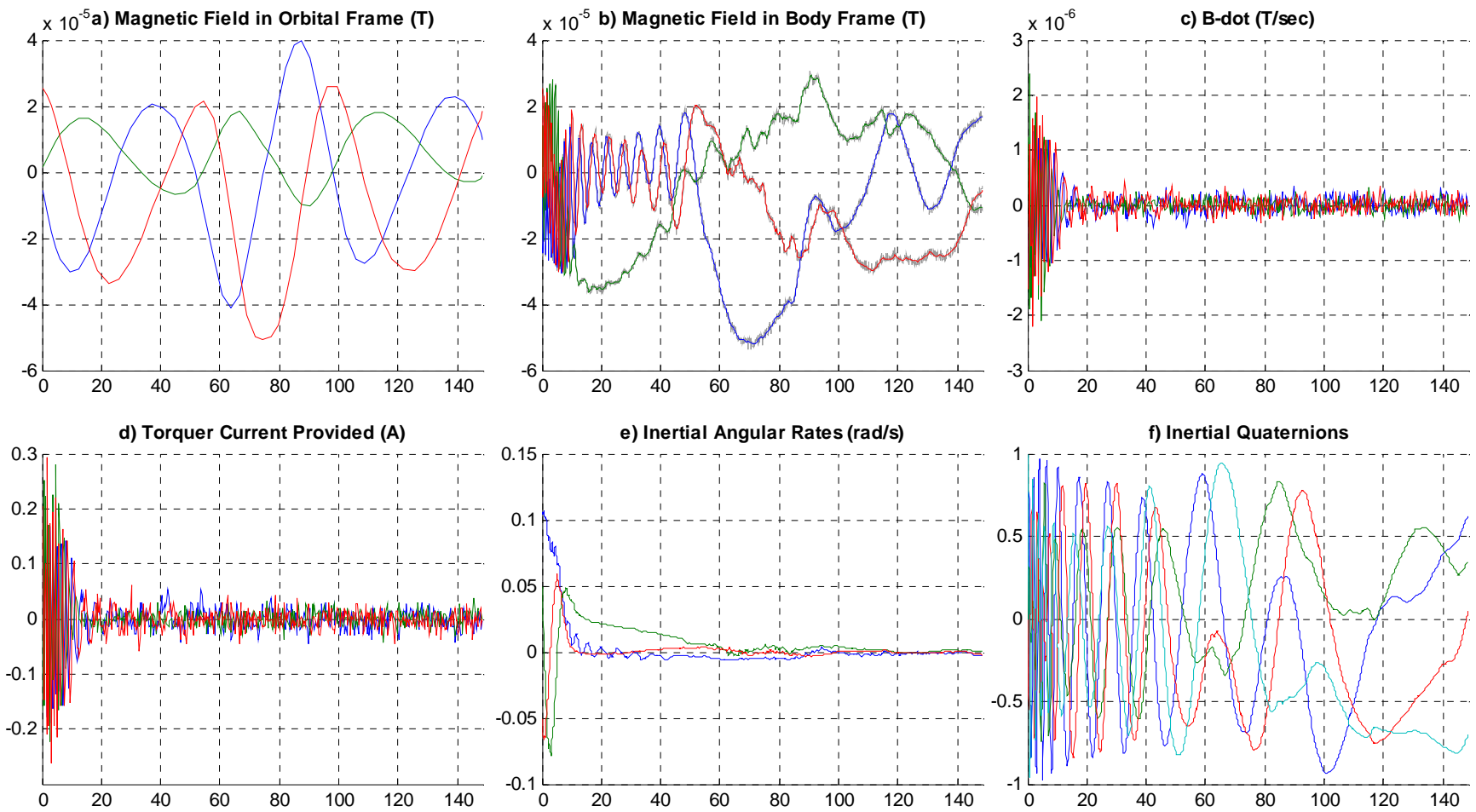


Figure 5.15: B-dot for 1.5 orbits with $\delta t = 10\text{sec}$, $\omega_o = 1\text{ rpm}$, $\sigma = 3\text{ bits}$, torquer 1 inactive

With a single torquer inactive, the final settling rates are similar, but the settling time is approximately doubled. Since the torque is perpendicular to the torquer axis, all three axes are controllable with only two torquers. The results are similar for a torquer out the other two axes. The system is unable to settle with two torquers out, however.

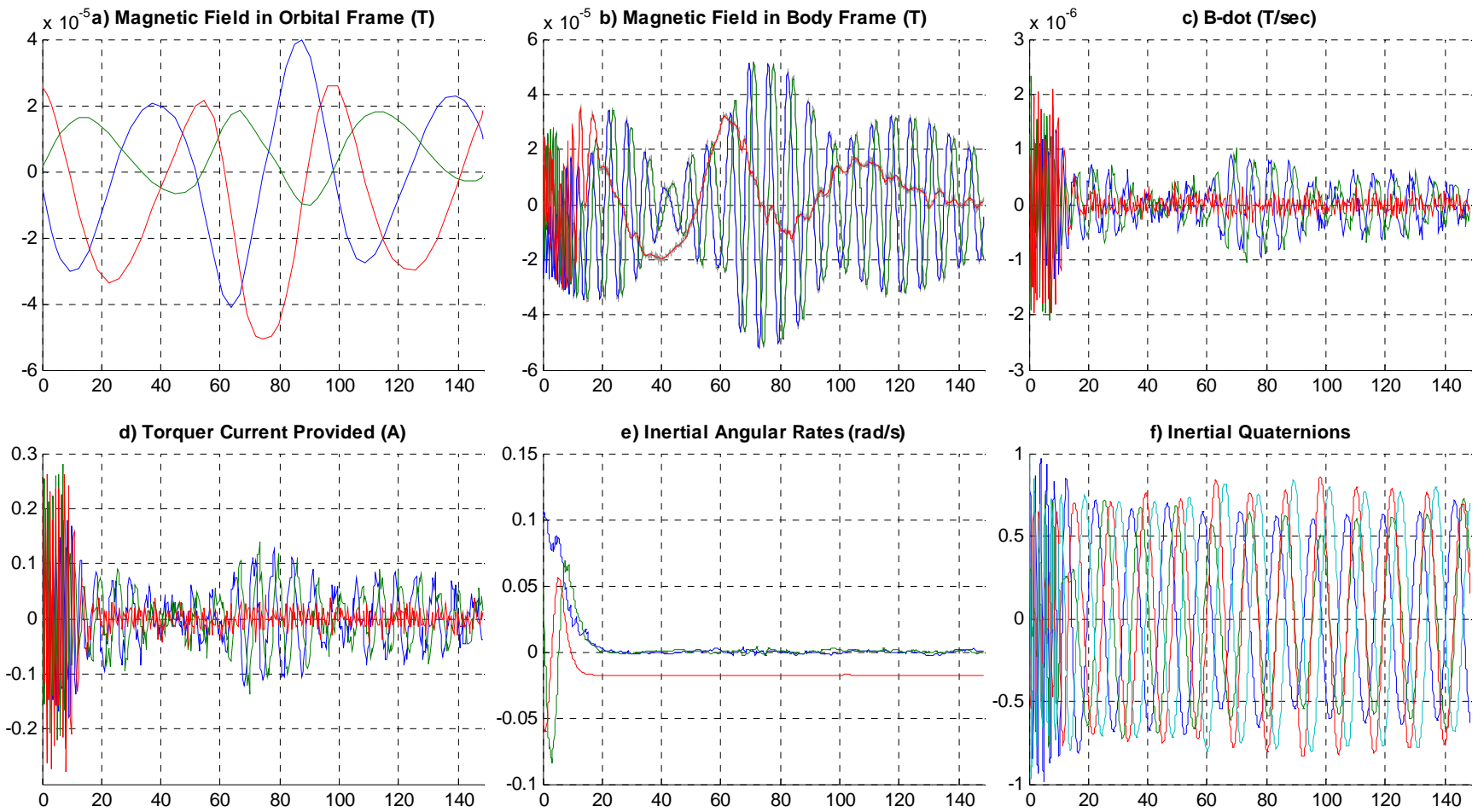


Figure 5.16: B-dot, 1.5 orbits, $\delta t = 10\text{sec}$, $\omega_o = 1\text{rpm}$, $\sigma = 3\text{bits}$, torquers 1 and 2 inactive

Since the one remaining torquer is not able to torque about its own axis, the ω_3 component never damps. Interestingly, the single torquer is very effective at damping out the other two axes and does so in less than a third of an orbit. The results are similar for the torquers out on other axes.

Since each torquer is capable of torquing in both of its in-plane axes, the system will damp as long as there are two orthogonal torquers active. With one torquer out, the final velocities are comparable to the full system with an associated increase in settling time.

5.1.6 CP2 Method vs. CP3 Method

An even simpler version of B-dot which has no magnetometer calibration data is implemented on the CP2 satellite. This method was outlined in Section 4.4.2.2. Performance was practically identical to the calibrated version for both the high noise and high tip-off velocities. Figure 5.17 below gives an example of the CP3 method with both high noise and velocity.

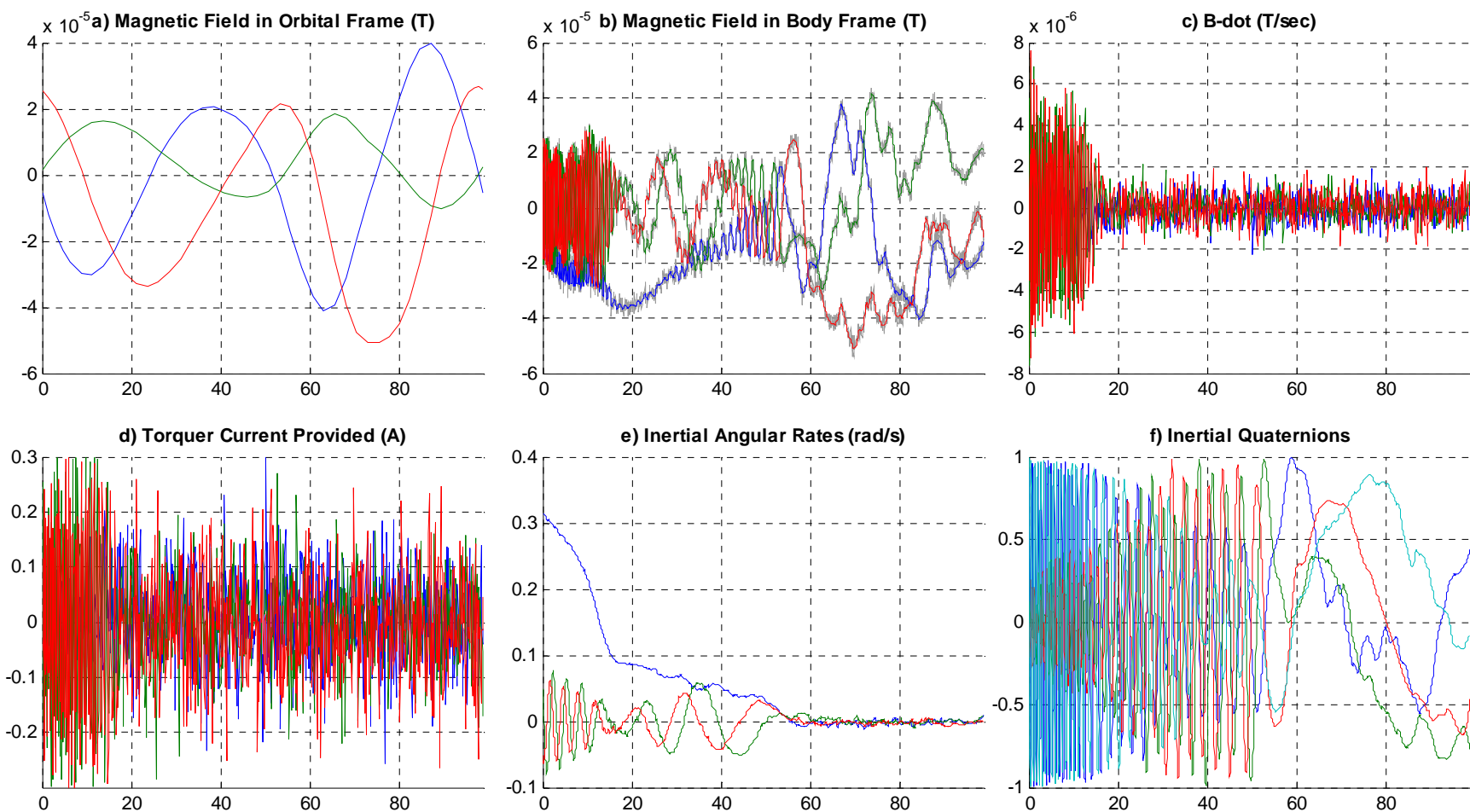


Figure 5.17: CP2 B-dot for 1 orbit with $\delta t = 4$ sec, $\omega_0 = 3$ rpm, $\sigma = 6$ bits

Even with a combination of high noise and initial rate, performance is nearly identical to the B-dot run with calibrated magnetometer data. Even though CP3 would have to have the calibration data onboard, the B-dot algorithm could be simplified in order to decrease processor load for the detumbling stage with few to no drawbacks.

5.1.7 B-Dot Conclusions

The B-dot algorithm was found to be very robust and could handle many types of failure with little drop in performance. The system still settled even in with the simultaneous introduction of high magnetometer noise, large tip-off velocities, and an inoperative torquer. It was also found that the system has a large range of stable gains which give some leeway for incorrect moment of inertia determination and decreases in available power. Finally, the CP2 method was found to be nearly as effective as the CP3 method and equally as stable. The CP2 method could therefore be implemented on CP3 if the savings in processing time were significant. If this were done, though, it would be important to make sure that the appropriate resistors were used to minimize the differences in offset and range between magnetometers.

5.2 Three-Axis Control

Even more simulations were run in order to optimize the control parameters for the three-axis controller. The main parameters are those of the position and rate gains and pulse length, which were found to be much more coupled than the B-dot parameters. Additionally, since the attitude determination hardware has not yet been selected, this report will also examine what requirements such a system might have in order to converge sufficiently. After these were found, performance with one and two torquers out was also analyzed. Finally, the capability of the algorithm to settle in any direction in both the orbital and inertial frames was demonstrated. As will be shown, all of these factors are interrelated and modifications in one require that the other parameters be re-optimized.

5.2.1 Explanation of Three-axis Plots

The results of each simulation are summarized in a single figure divided into six subplots lettered from a-f. The current and magnetic field plots shown for B-dot were replaced with attitude-related plots since that is the primary concern here. Furthermore, the current draw on the torquers was extremely low, peaking at 0.1 A initially and then averaging less than 1 mA. The x-axis of all plots is given in minutes. One may use the orbital period of approximately 95 minutes to convert these values to fractions of an orbit. With the exception of the quaternions, the lines within each subplot represent Cartesian axes and are colored according to:

Axis 1: Blue

Axis 2: Green

Axis 3: Red

Axis 4: Cyan (for quaternions only)

The line types are:

- Solid: Actual values used by the simulation.
- Dashed: Desired values used by the control algorithm.
- Gray: Measured values used by control algorithm. Include discretization and noise.

An explanation of each subplot follows:

- a) *Quaternion Error* displays the quaternion rotation between the actual and desired quaternion vectors as defined in equation 4.5. The first three terms are used in the torque calculation.
- b) *Inertial Angular Rates* are the actual simulated values. See Section 2.4.2 for a definition of the frame.
- c) *Inertial Quaternions*. See Section 2.4.2 for a definition of the frame.
- d) *Pointing Error* represents the error rotation angle about the quaternion error axis. It was calculated from:

$$q_{e4} = \cos\left(\frac{\theta_e}{2}\right)$$

Small changes in q_{e4} are compounded as θ_e approaches zero, so any noise in the quaternion signal is extremely amplified.

- e) *Orbital Angular Rates*. See Section 2.4.3 for a definition of the frame. These are given for reference only and were not used directly in the error calculation.
- f) *Orbital Quaternions*. See Section 2.4.3 for a definition of the frame. These are given for reference only and were not used directly in the error calculation.

5.2.2 Optimum Gains Determination

The optimum gains were found using trial and error on a range of values and selecting the ones that settled the best pointing accuracy the fastest. These simulations were run without noise in the sensor readings and initial angular velocities of $\omega = [0.005 \ -0.005 \ 0.002]^T$, is a conservative post-B-dot case. The desired quaternion vector was $q_d = [0.5 \ 0.5 \ 0.5 \ 0.5]$, which was chosen because it represents a rotation about all three axes. This algorithm was found to take considerably longer to settle to a reasonable pointing accuracy, so the simulation time was increased to five or seven orbits. Because of the slow rotations, the pulse lengths were set to twenty seconds.

The range of gains for which the system would settle was fairly narrow, with the system not settling on both the high and low ends of the spectrum. Since the rates in rad/s were about three orders of magnitude smaller than the quaternions, the quaternion gain was always three orders of magnitude smaller than the rate gain. There were four basic types of undesirable behavior: divergence, oscillation about the desired, very low pointing accuracy, very long settling time. The best rate gains were in the range from $2e-2$ to $5e-2$, while the best position gains were from $1e-5$ to $3e-5$. Finding this range was fairly difficult due to the coupling of the two gains. The plot below shows the results for the best gain combination of $C_1 = 4e-2$ and $C_2 = 3e-5$.

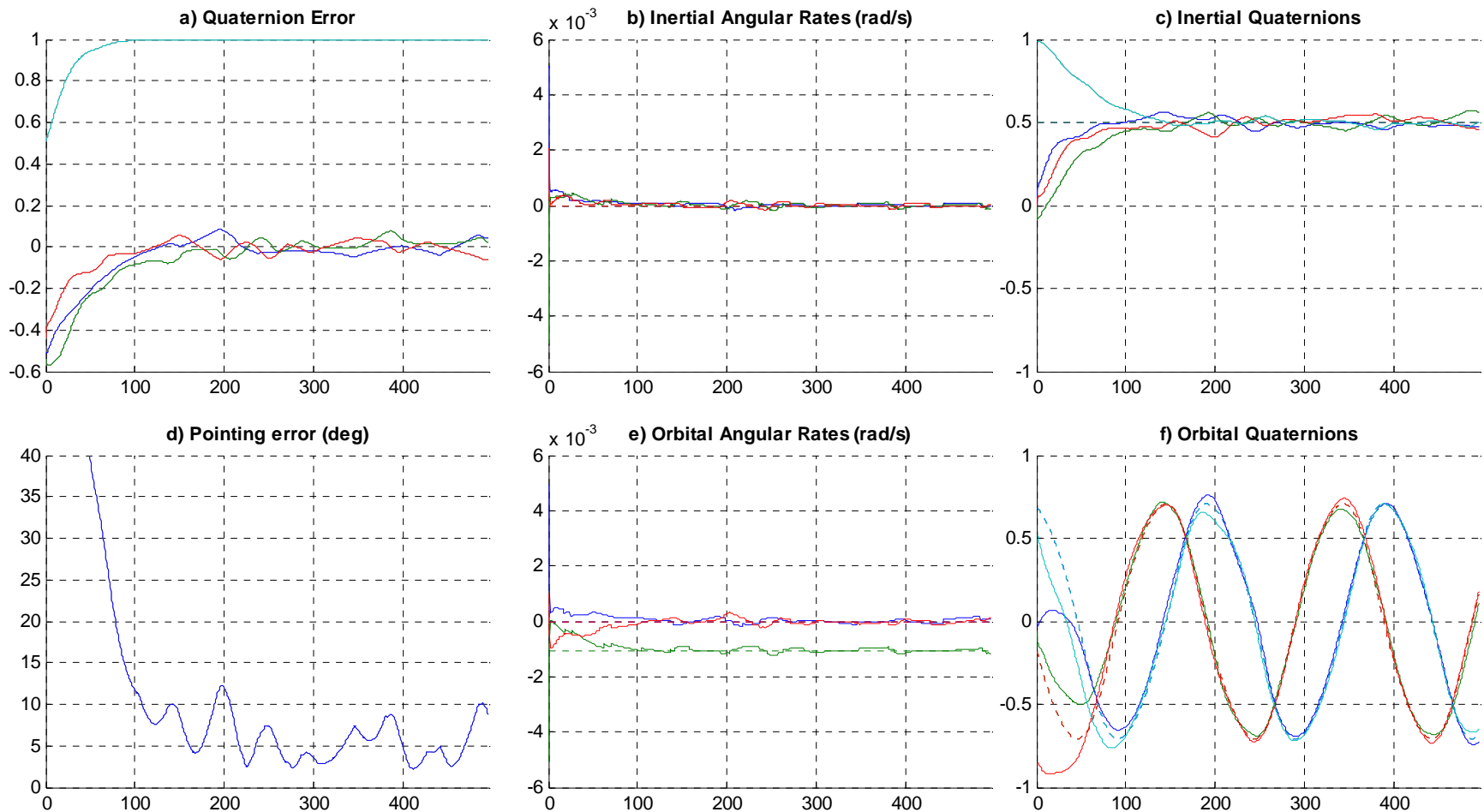


Figure 5.18: 3-axis, $C_1 = 4\text{e-}2$, $C_2 = 3\text{e-}5$, $\delta t = 20\text{sec}$, 5 orbits

Plot d) shows how the system settles to within 12° after approximately one orbit. The rates settle extremely rapidly, dropping to a tenth of their original magnitude in a matter of minutes. Increasing either of the gains produces instability in the system. The next figure shows the results for an increase in the rate gain.

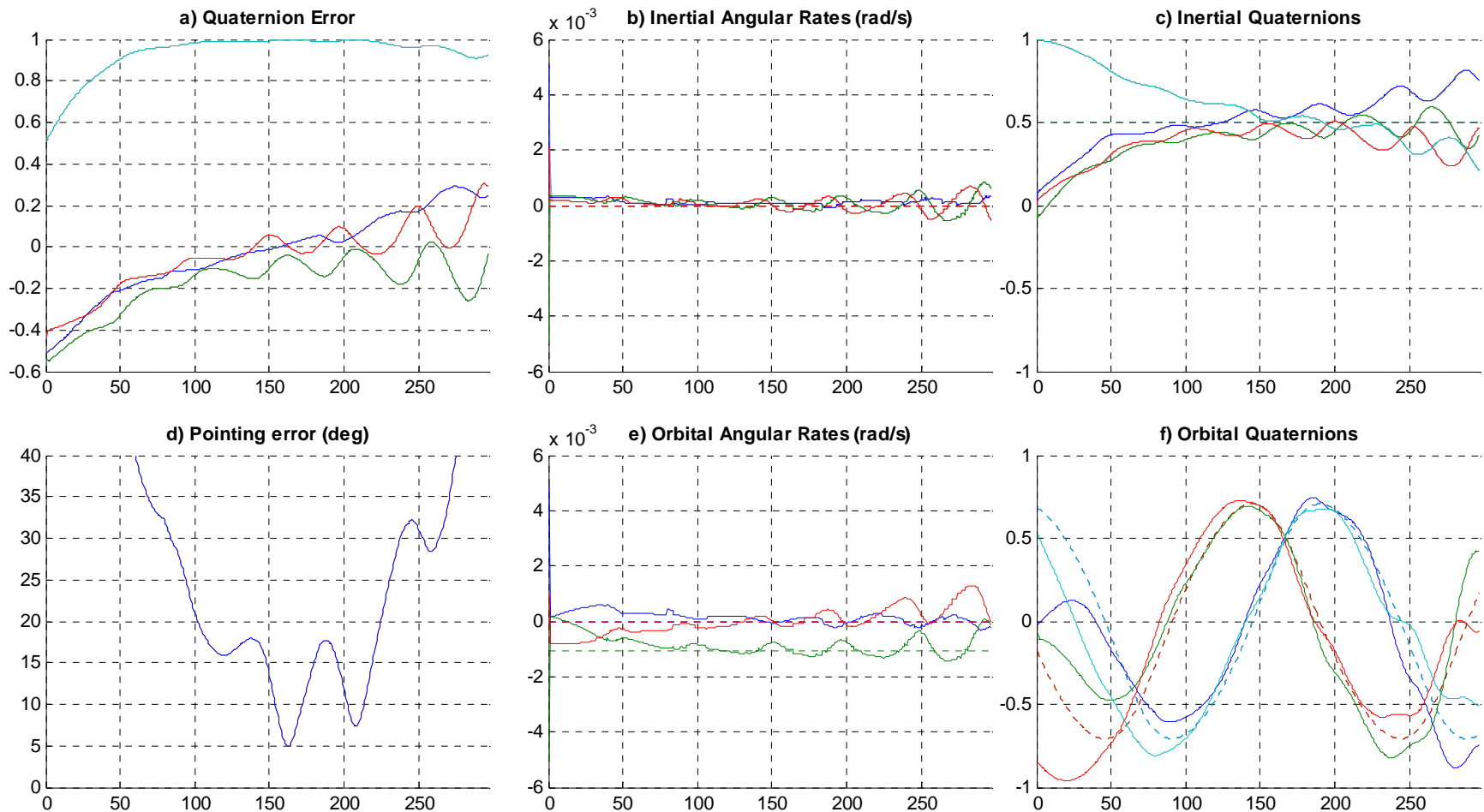


Figure 5.19: 3-axis, $C_1 = 5e-2$, $C_2 = 3e-5$, $\delta t = 20\text{sec}$, 3 orbits

This is an example of divergent behavior. In this case, the rate gain was incremented to $5e-2$, which created eventual instability as the quaternions approached their target. A rate gain of $5e-2$ can be stabilized, however, if the position gain is dropped to $2e-5$ or lower. Rate gains of $6e-2$ and higher though are always unstable. Instability can also occur if the gains are too low.

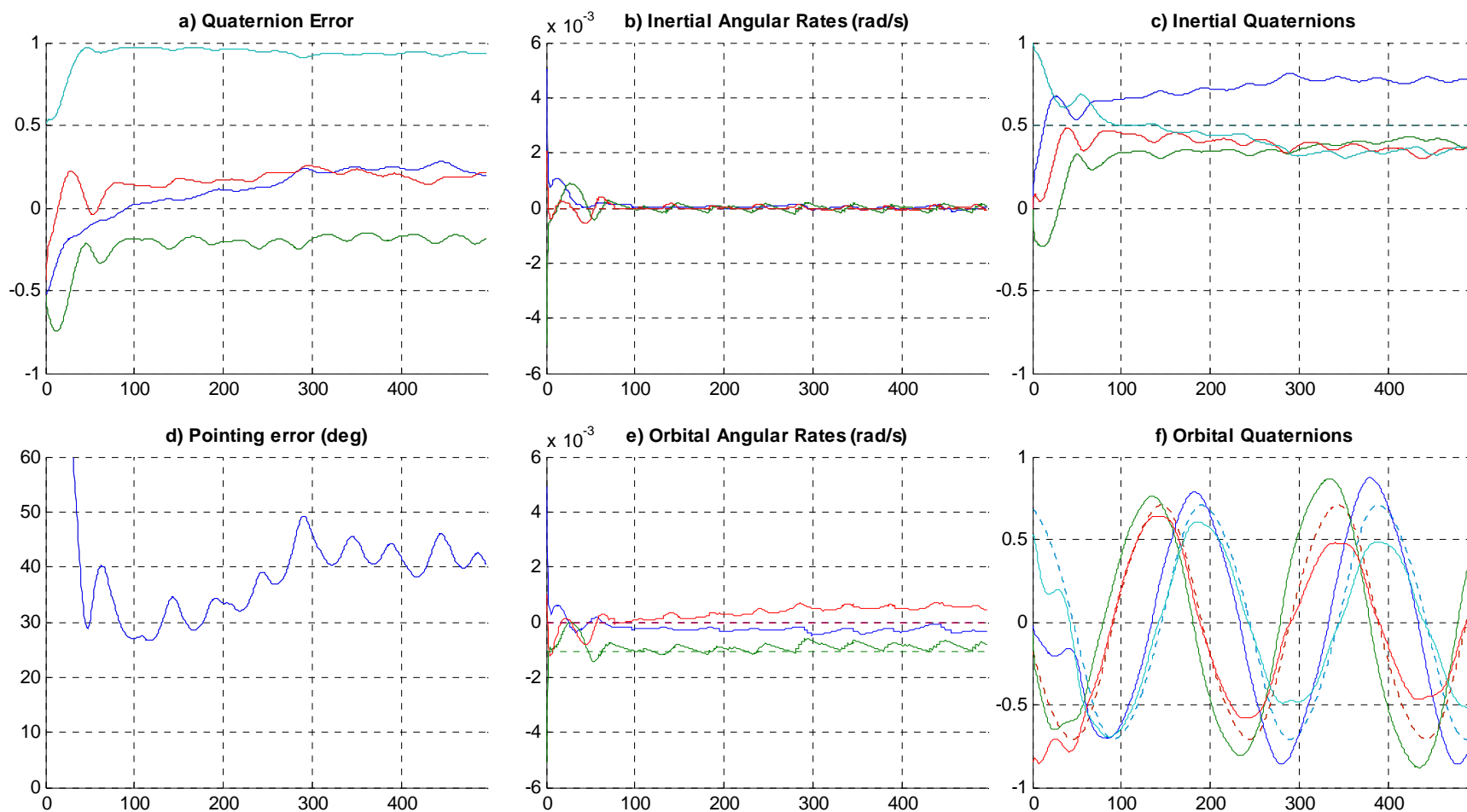


Figure 5.20: 3-axis, $C_1 = 2e-2$, $C_2 = 1e-5$, $\delta t = 20\text{sec}$, 5 orbits

Here the rate gain seems to be acceptable; however, the position gain is just not high enough to induce the system to settle to a reasonable pointing accuracy. This system might benefit from the addition of a position error integrator. If the gains are set too high, though, the system can also develop a rate oscillation that refuses to damp out.

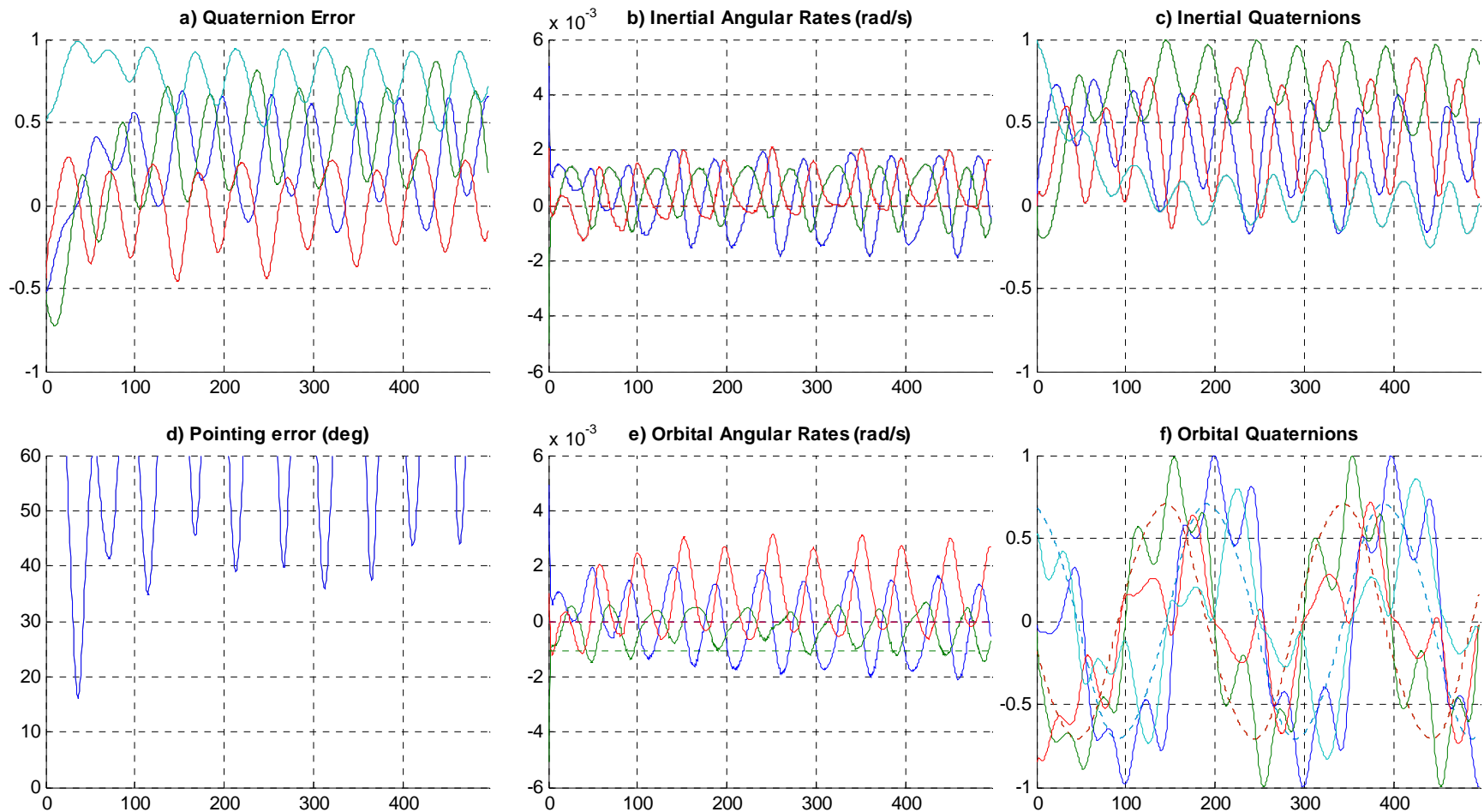


Figure 5.21: 3-axis, $C_1 = 2e-2$, $C_2 = 2e-5$, $\delta t = 20\text{sec}$, 5 orbits

Incrementing the position gain independently of the rate gain caused the system to start circling about the desired position at a distance of about 45° . While neither gain is particularly high, together they are too high for the system to handle. Even though the system does not blow up entirely, it is clear that it will never approach the desired either.

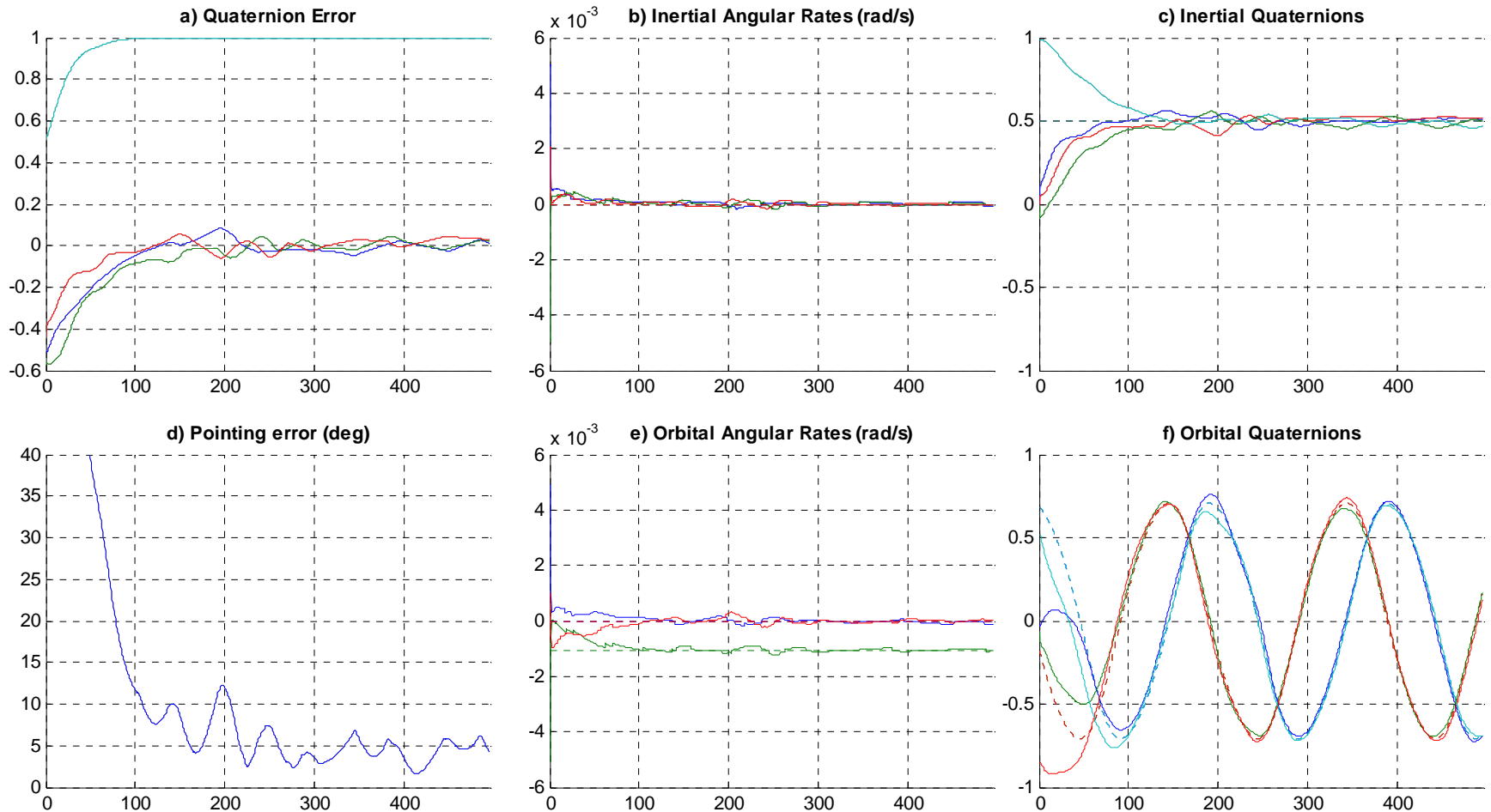


Figure 5.22: 3-axis, $C_1 = 4e-2$, $C_2 = 3e-5$, $\delta t = 20\text{sec}$, 5 orbits, 3° shutoff

Returning to the best gains of $C_1 = 4e-2$ and $C_2 = 3e-5$, accuracy can be improved upon even further by using an algorithm similar to the one used for B-dot. This algorithm deactivates controller once the spacecraft is pointed within a certain limit of the target and then reactivates it as the spacecraft drifts off-target. The results are shown for a cutoff value of 3° . Compare to Figure 5.18.

The table below summarizes the results of the gain optimization work.

Table 5.1: Three-axis gain investigation

<i>Rate Gain (C1)</i>	<i>Position Gain (C2)</i>	<i>Settling Time (min)</i>	<i>Accuracy (deg)</i>
2e-2	2e-1	q _e won't close	C2 too low
2e-2	2e-5	Rates oscillate	C1 too low
3e-2	1e-5	Extremely slow	C2 too low
3e-2	2e-5	260	11
3e-2	3e-5	Diverges	Combo too high
4e-2	1e-5	Diverges	C2 too low
4e-2	2e-5	180	15
4e-2	3e-5	210	10
4e-2	4e-5	Diverges	C2 too high
5e-2	2e-5	200	13
5e-2	3e-5	Diverges	Combo too high
6e-2	1e-5	Diverges	C1 too high

This table shows the upper and lower boundaries of the acceptable gain range. In conclusion, the gains are highly coupled to each other, and it is important to have both at appropriate values. Also, since the range for which the system converges is so narrow, it is important that the moments of inertia of the spacecraft be accurately determined. Additionally, the shutoff algorithm had some success at making previously unstable gain values stable, especially for the noisy signals discussed in Section 5.2.5 below.

5.2.3 Optimum Pulse Time Determination

Unlike B-dot, there is a large amount of coupling between both the gains and pulse time. All three parameters have an effect on stability, settling time, and pointing accuracy, so the optimum combination had to be found for all three parameters at once. Since the angular rates are all very

small at this point, B-dot's problem where the field changed too much during long pulse times does not apply. Instead, long pulse times cause the system to drift back and forth across its goal too much for it to settle. For this analysis, the pulse time was varied to find the lowest pointing error. The optimum gain of the previous section was used, as well as the same initial velocities representative of a post-B-dot scenario. For this gain setup, the best pulse length was approximately 17 seconds, and the results are shown below.

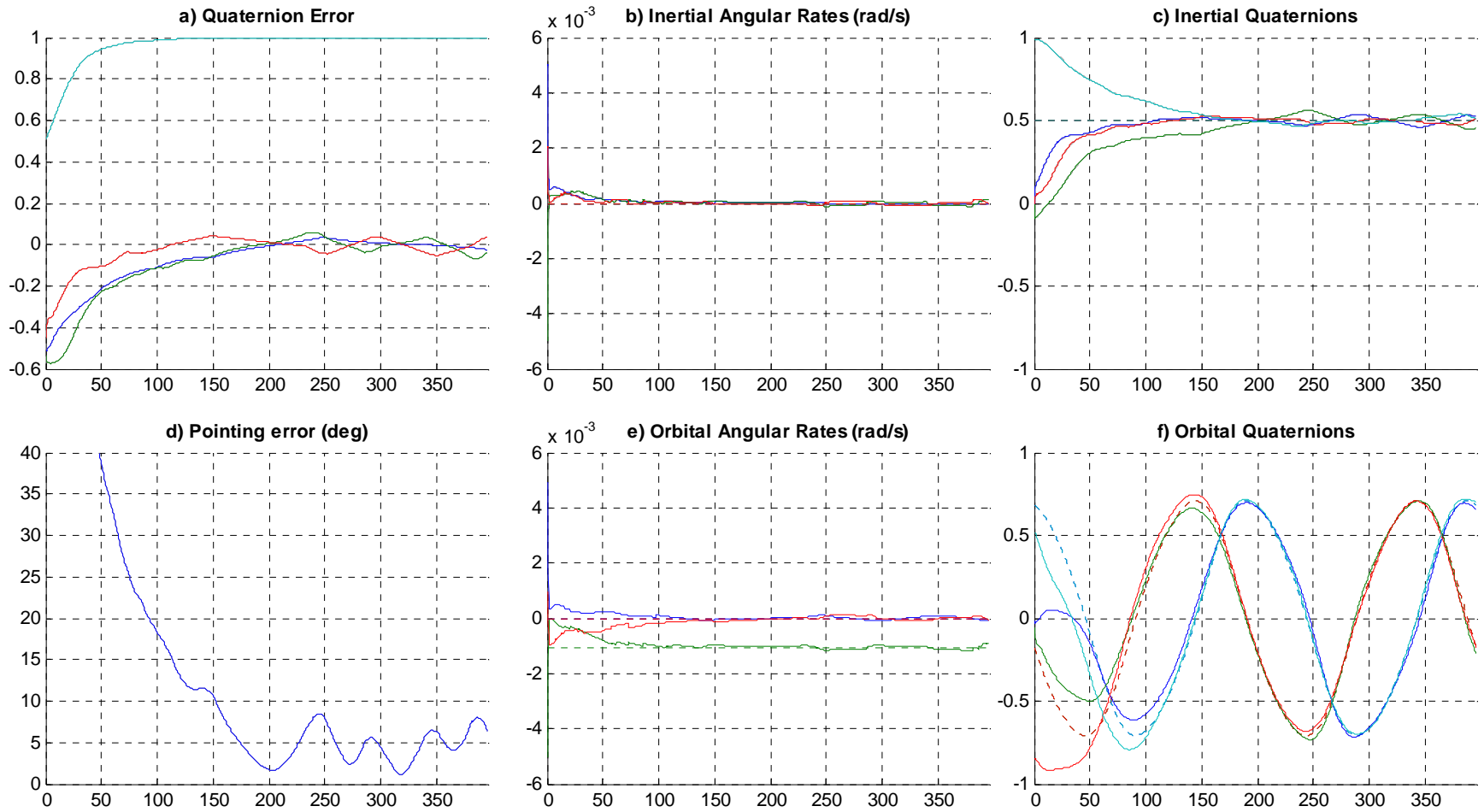


Figure 5.23: 3-axis, $C_1 = 4e-2$, $C_2 = 3e-5$, $\delta t = 17\text{sec}$, 4 orbits, 3° shutoff

While this is not a large improvement on the 20 or 15 second cases, the steady-state condition for 17 seconds has the mildest oscillation. Without any noise in the system, the best pointing accuracy achievable is about 8° - 9° with errors as low as 2° for brief periods. Decreasing the pulse time below harms accuracy as shown below for a simulation with 10 second pulses.

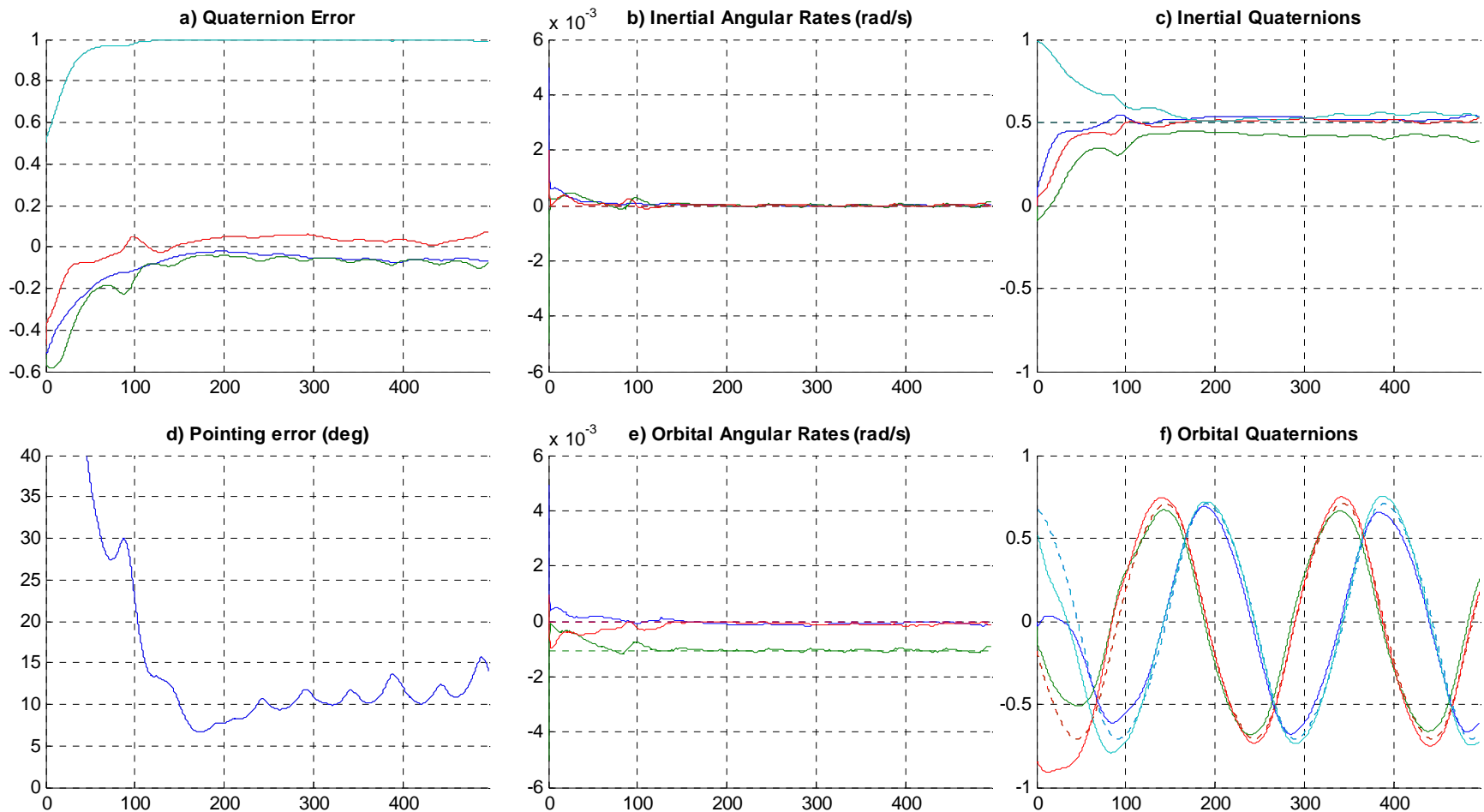


Figure 5.24: 3-axis, $C_1 = 4e-2$, $C_2 = 3e-5$, $\delta t = 10\text{sec}$, 5 orbits, 3° shutoff

Here, as the spacecraft approaches the desired point, it cannot close the gap even though the rates are very low. One possible explanation is that with the rates low the short pulses do not have time to do their job before being recalculated.

The results of the pulse length investigation are summarized in the table below.

Table 5.2: Results of Pulse Length Variation

<i>Pulse Length (sec)</i>	<i>Settling Time (sec)</i>	<i>Pointing Accuracy (deg)</i>
5	100	21
10	120	14
15	160	8
17	160	8
20	210	10
25	Unstable	180

The 17 seconds selected as the optimum lies in the middle of the saddle between unstable and low accuracy. This is the value that will be used for the remainder of the experiments.

5.2.4 Effect of Sensor Resolution

This section is an exploration of the requirements for accuracy necessary for three-axis control rather than a simulation of actual hardware. Not only is this thesis designed to be generally applied, but at the time of writing the sensors for CP3 had not been selected nor their capabilities explored. For this experiment, the resolutions δq and $\delta \omega$ from equation 4.3 were modified while the standard deviations of the noise levels were kept small. The same initial velocity and pulse lengths as the previous section were used. The results were fairly predictable; the lower the resolution, the higher the pointing error until the system could no longer stabilize. Working on each sensor individually, the lowest rate resolution for which the system settled was $1e-3$ rad/s (0.057 deg/s).

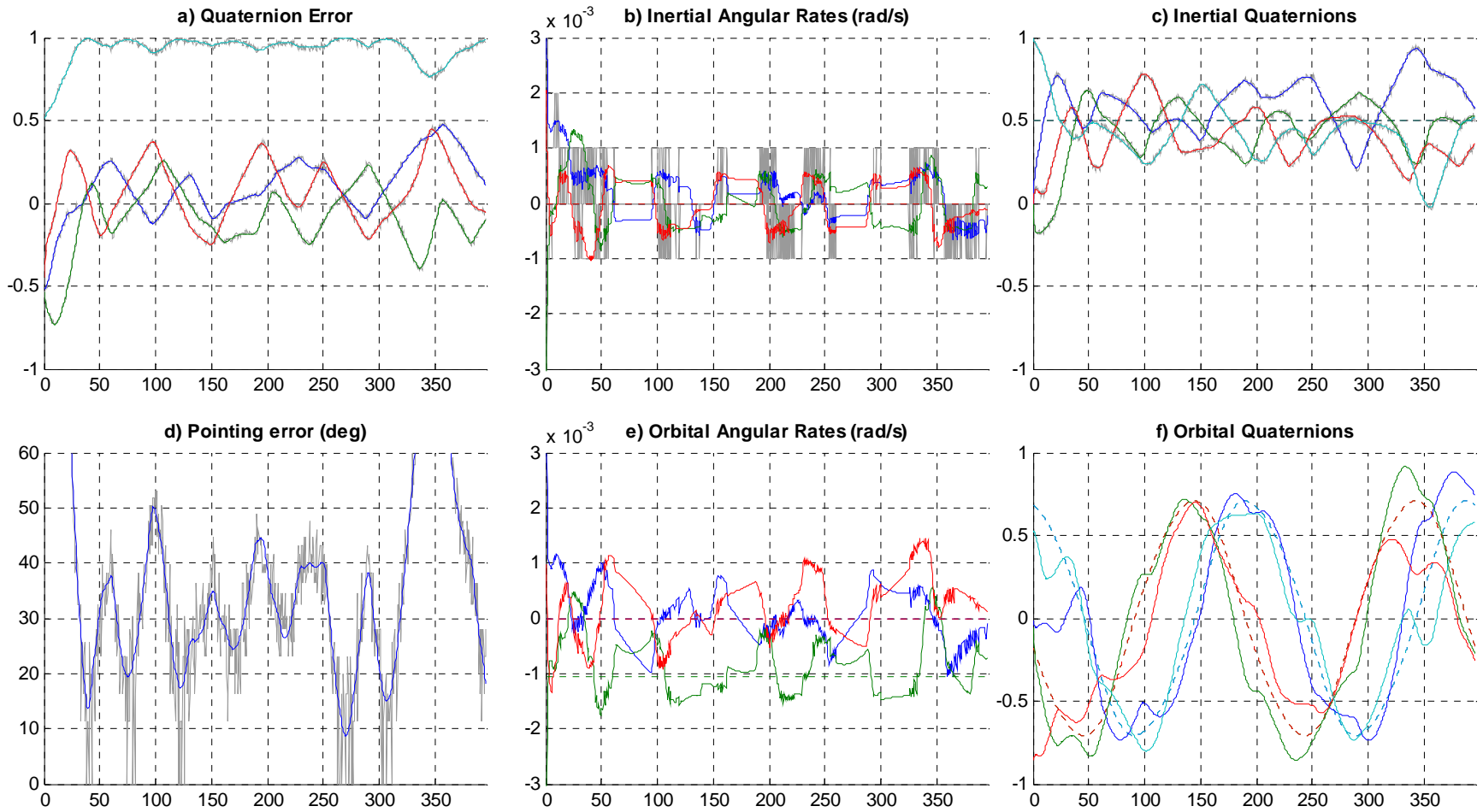


Figure 5.25: 3-axis, $C_1 = 2e-2$, $C_2 = 2e-5$, $\delta\omega = 1e-3$ rad/s, $\delta q = 0.01$

Except for one deviation, the system converges to point within about 45° of the target even with these extremely low resolutions. In order to get the system to converge, however, it was necessary to lower the gain values to $C_1 = 2e-2$, $C_2 = 2e-5$. Please note that the y-scales of subplots b), d), and e) have been restricted to focus on the settling conditions and make allowances for worse accuracy.

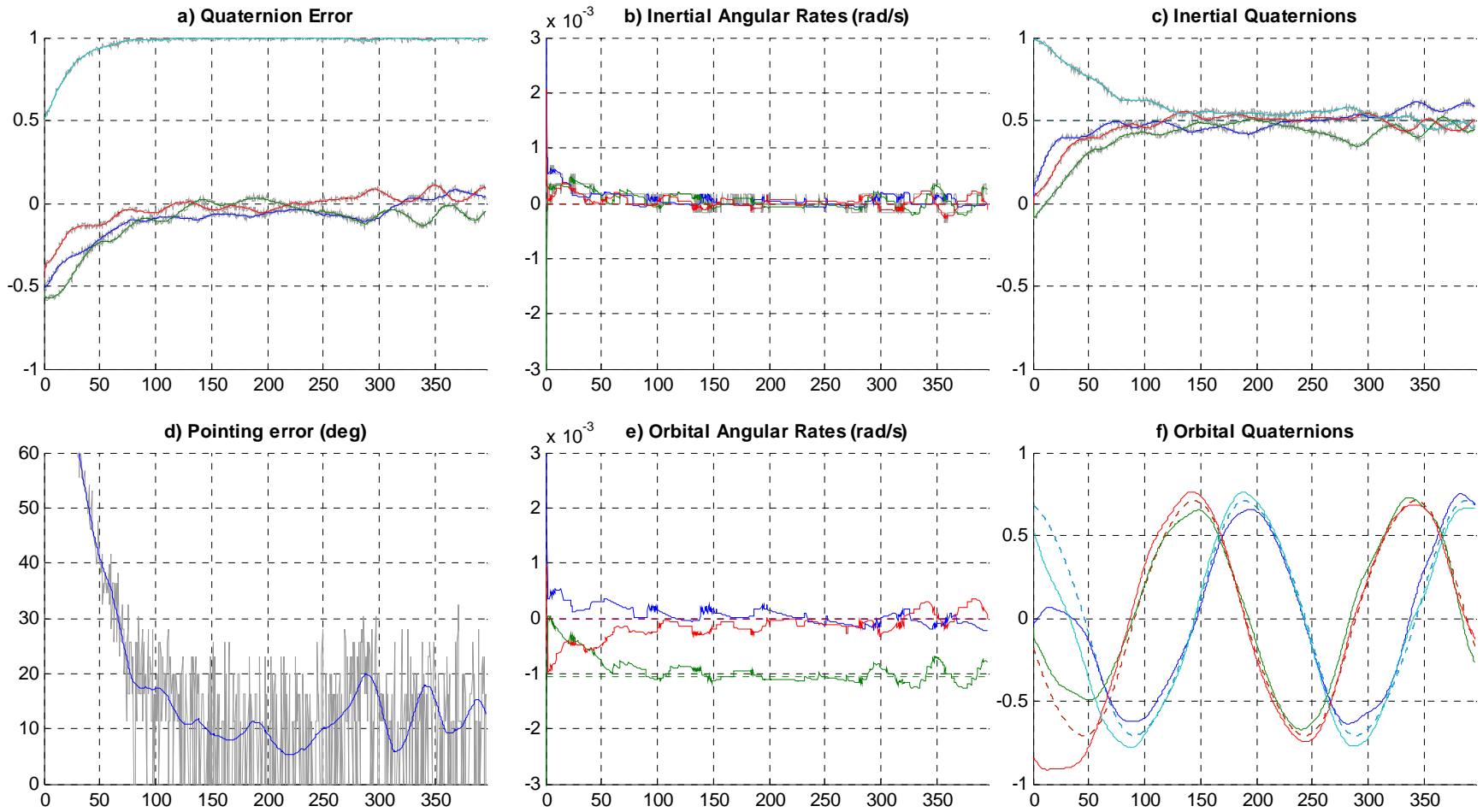


Figure 5.26: 3-axis, $C_1 = 4e-2$, $C_2 = 3e-5$, $\delta\omega = 0.01$ deg/s, $\delta q = 0.01$

Pulling back from the extreme case above, the lowest resolution for which the original gains settled was approximately 0.01 deg/s (1.8e-4 rad/s). Even with this low resolution the pointing accuracy only suffers by about 10° and settling time is lowered to within one orbit. The next figure illustrates how much more forgiving the controller is of extremely low quaternion resolutions.

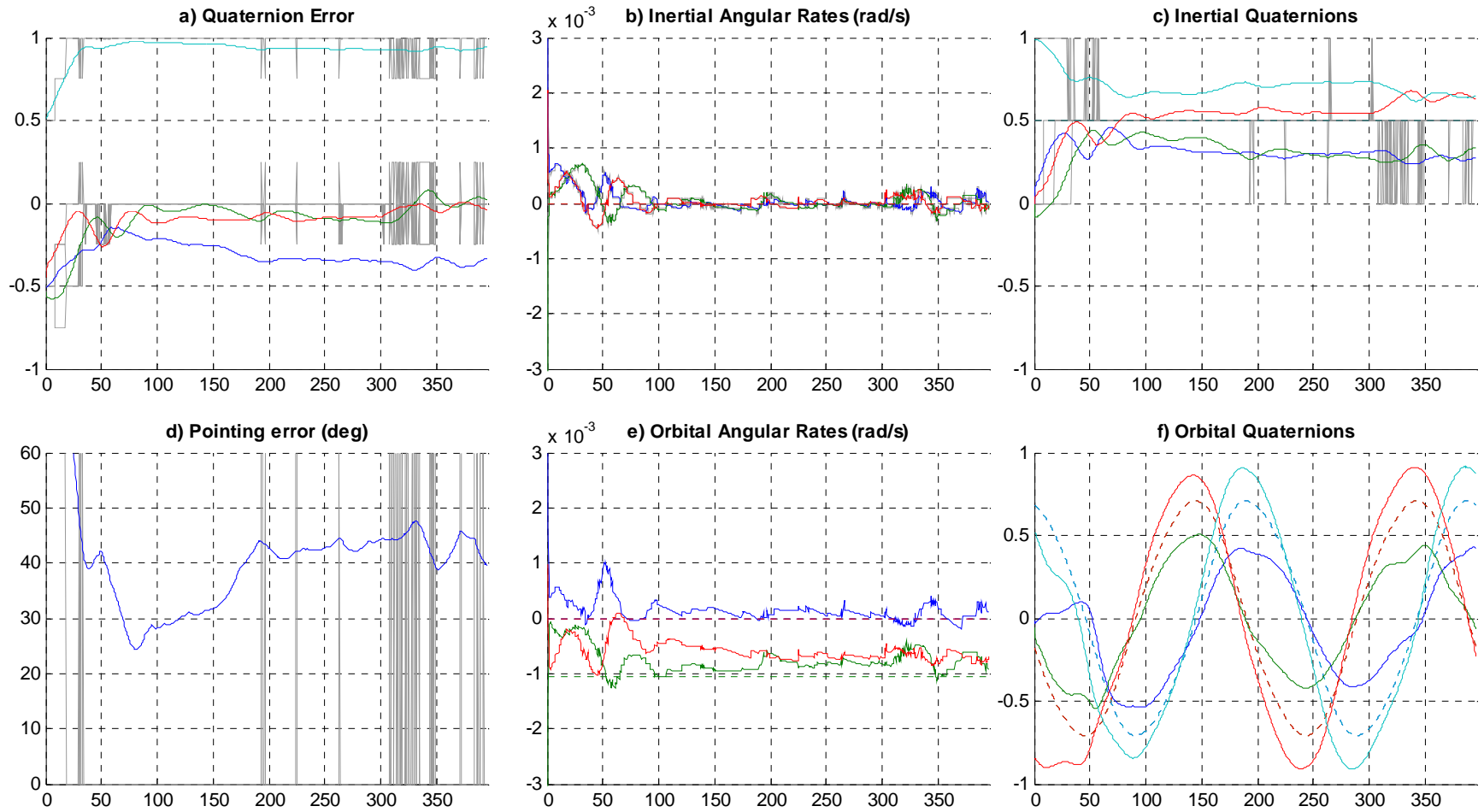


Figure 5.27: 3-axis, $C_1 = 4e-2$, $C_2 = 3e-5$, $\delta\omega = 1e-4$ rad/s, $\delta q = 0.5$

In this simulation, the quaternions are rounded to 0.5 meaning there are only five possible values for each component. This made it impossible for the system to close the gap, but it was at least stable with an accuracy of about 45°. Combining the digitization of both sensors at more reasonable values produced the following results.

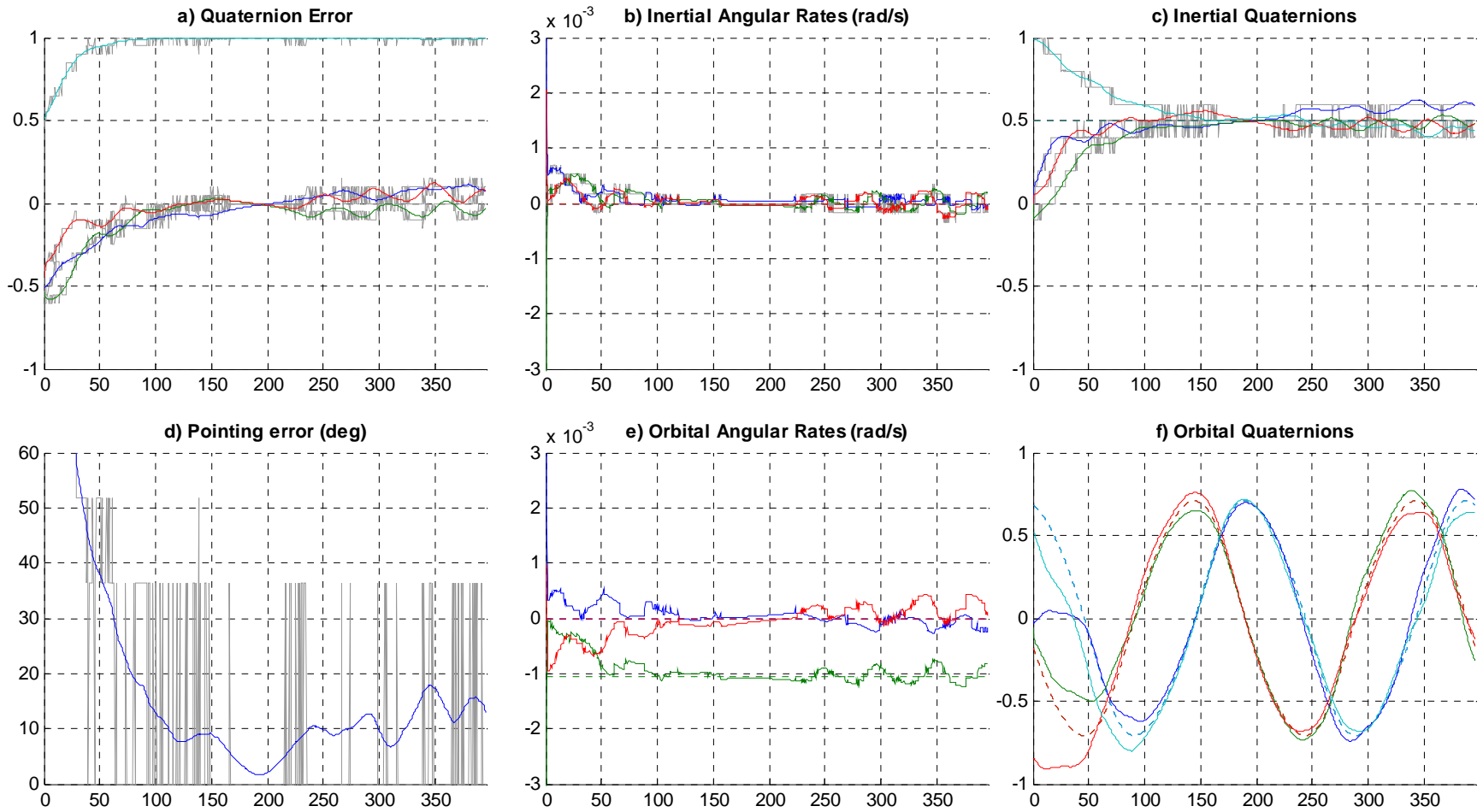


Figure 5.28: 3-axis, $C_1 = 4e-2$, $C_2 = 3e-5$, $\delta\omega = 0.01$ deg/s, $\delta q = 0.1$

This figure shows that with reasonably precise sensors, pointing accuracies in 10-15 degree range are not unreasonable. Additionally, precise rate knowledge is much more critical to stability than position information is.

5.2.5 Effect of Sensor Noise

As mentioned for B-dot, the magnetometers were found to be practically noise free, and the simulation of their noise represents magnetic interference from operating components. The instruments used for attitude determination under consideration would not be influenced by electromagnetic fields the way that magnetometers are, so fairly low noise levels should be achievable for the attitude information. Ideally, a Kalman filter would also be implemented to further reduce this noise. The experiment was run by increasing the value of the standard deviation of the noise, σ , from equation 4.3. The same initial velocities and pulse times were used as for previous simulations and the shutoff algorithm was employed to mitigate noise problems. The resolutions were set to $1\text{e-}4$ rad/s (0.006 deg/s) for the rates and 0.1 for the quaternions.

As with resolution, it was found that low rates noise was more important than low position noise. The next figure shows the results of a simulation run with medium noise levels for both rate and position using the optimum gains found earlier.

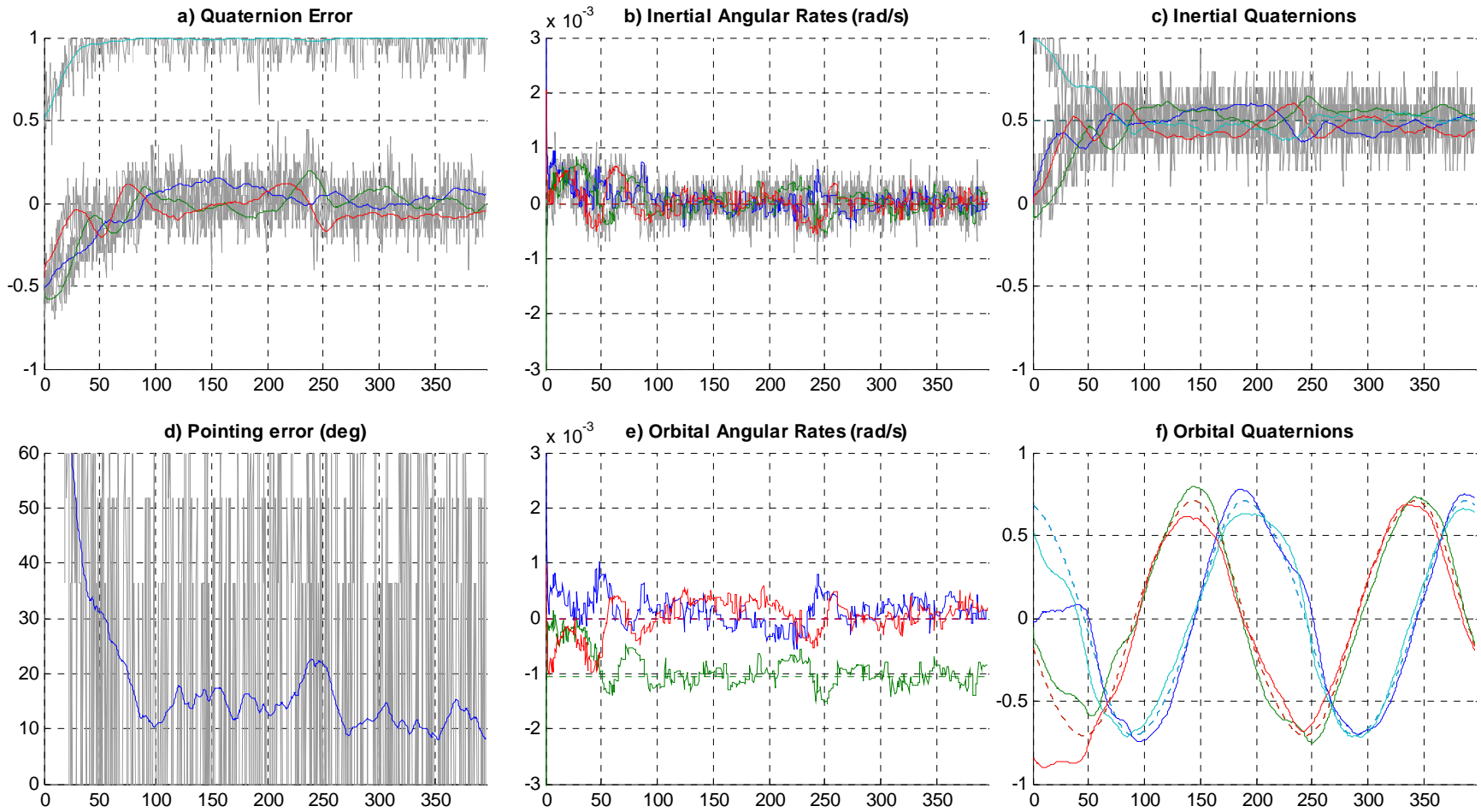


Figure 5.29: 3-axis, $C_1 = 4\text{e-}2$, $C_2 = 3\text{e-}5$, $\delta\omega = 1\text{e-}4$ rad/s, $\delta q = 0.1$, $\sigma_\omega = 2\text{e-}4$ rad/s, $\sigma_q = 0.1$

Even with signal-to-noise ratios (S:N) of about 3:1, the system settles to within about 20° after one orbit. Increasing the rate noise beyond this level causes the spacecraft to go unstable and increasing the position noise causes it to settle with an error greater than 60° . By lowering the gain, however, the system is capable of handling even more noise.

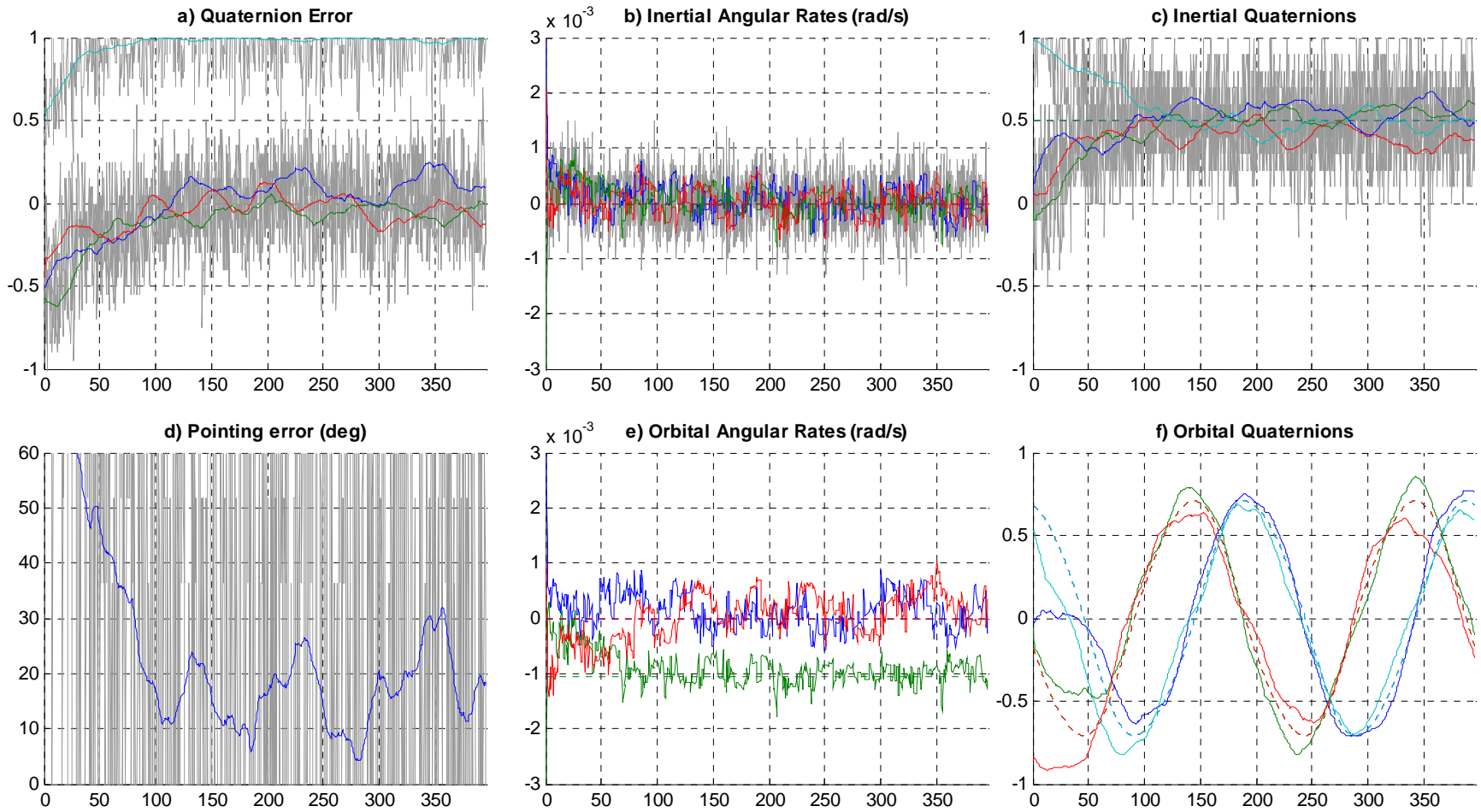


Figure 5.30: 3-axis, $C_1 = 3\text{e-}2$, $C_2 = 2\text{e-}5$, $\delta\omega = 1\text{e-}4$ rad/s, $\delta q = 0.1$, $\sigma_\omega = 4\text{e-}4$ rad/s, $\sigma_q = 0.2$

Incrementing the gains down allowed the introduction of extremely unlikely levels of noise with S:N of nearly 1:1. Even so, the system was able to point within 30° of the target. Note that the accuracy oscillates at the orbital period with valleys near the equator. The control law was also able to handle even larger noise levels for each sensor type individually, just not both at the same time.

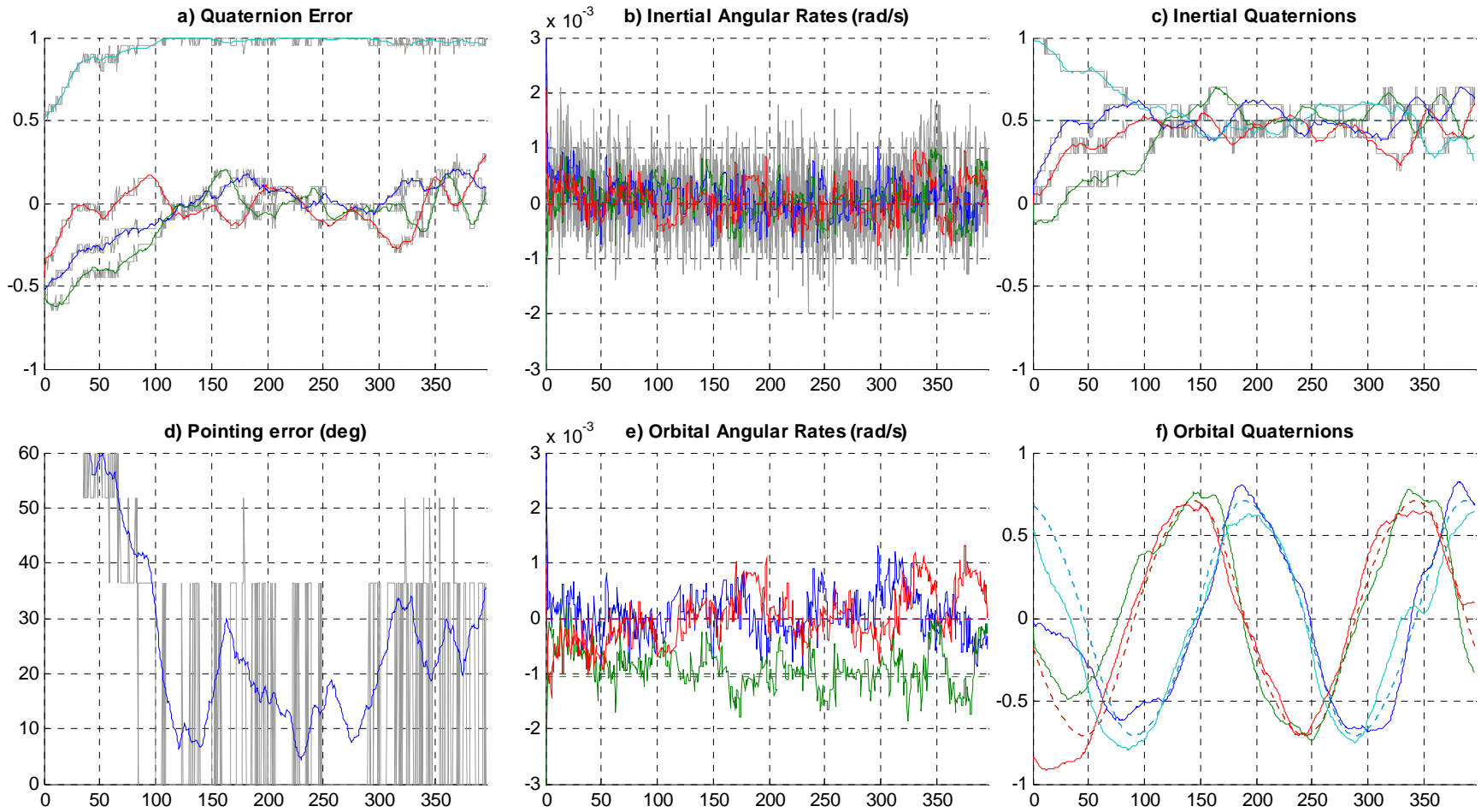


Figure 5.31: 3-axis, $C_1 = 3e-2$, $C_2 = 2e-5$, $\delta\omega = 1e-4$ rad/s, $\delta q = 0.1$, $\sigma_\omega = 5e-4$ rad/s, $\sigma_q = 0.01$

The gain of Figure 5.30 was better at handling high rate noise and was used for the above simulation. With the quaternion noise minimized, it was able to handle rate noise with S:N of 1:1.5.

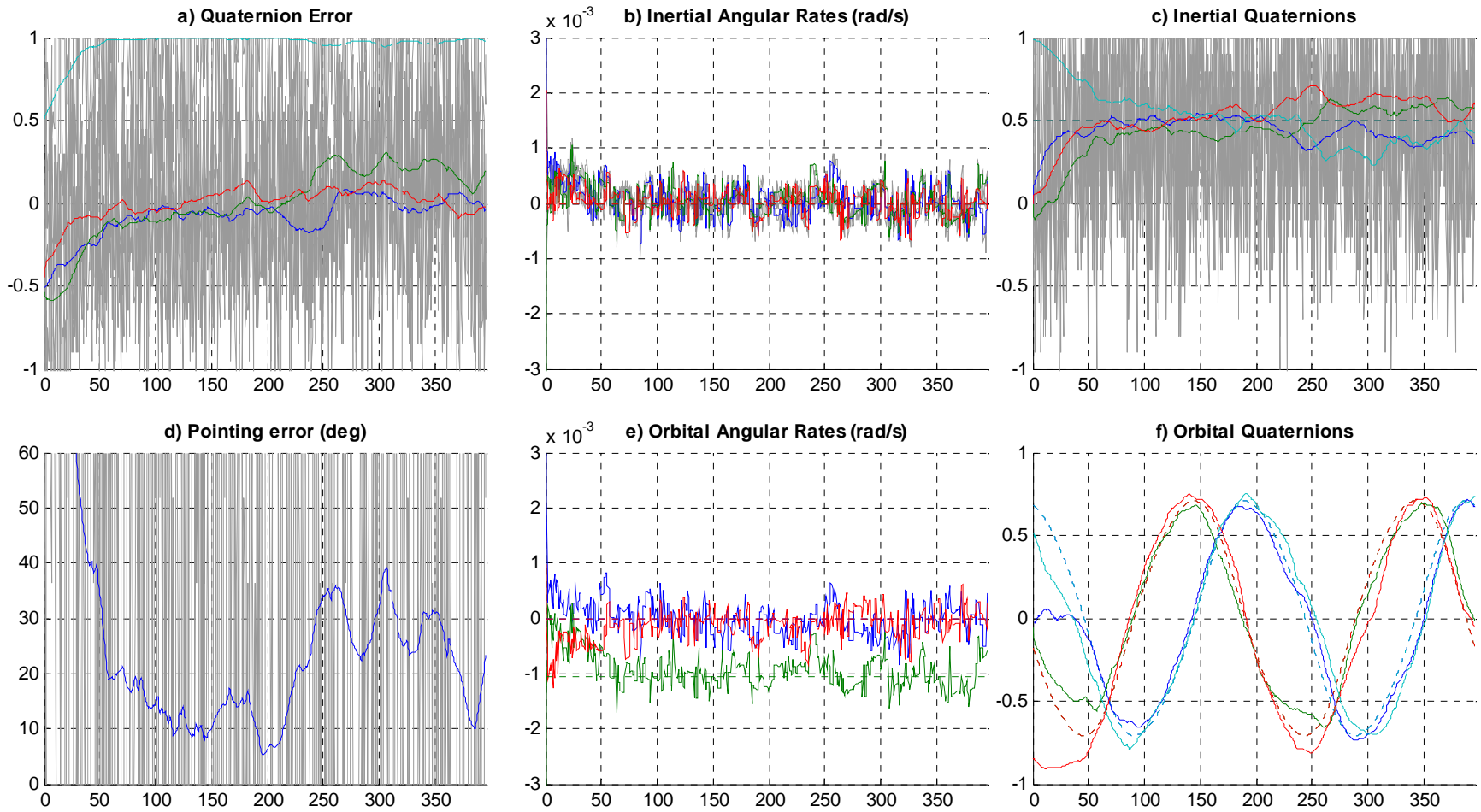


Figure 5.32: 3-axis, $C_1 = 4\text{e-}2$, $C_2 = 3\text{e-}5$, $\delta\omega = 1\text{e-}4$ rad/s, $\delta q = 0.1$, $\sigma_\omega = 1\text{e-}4$ rad/s, $\sigma_q = 0.5$

The original gains turned out to be better for quaternion noise, so they were used for the above example. By keeping the rate noise low, the controller functioned relatively effectively even when the quaternion noise reached S:N of 1:2. Both of the previous two cases represent a malfunction in the determination system which hopefully would be caught on the ground.

It was found that performance under noisy conditions could be improved by lowering the gains, but a minor drop in pointing accuracy. The optimum gains from earlier of $C_1 = 4e-2$ and $C_2 = 3e-5$ were unable to handle much noise in the rates, so the gains were pulled back to $C_1 = 3e-2$ and $C_2 = 2e-5$. These were much more robust against noise in the rates and good enough for quaternion noise. One benefit of the loss in pointing accuracy was that the system was able to reach its relatively steady state much faster. This means that if pointing requirements are relaxed slew time can be greatly improved. Additionally, the system would periodically reach pointing errors of less than 10° even with extremely noisy signals. For example, if one wanted to take a picture of a particular star and determination were fairly accurate, one could create a subroutine that only took the picture once the pointing error was within an acceptable threshold.

5.2.6 One and Two Torquers Out Performance

Next was examined the failure case of one or more torquers failing and the problem going undetected. Since there is redundancy on two of the control axes, should one torquer fail the redundant torquer could be activated to make up for it. While no system settled with only one active torquer, it was found that settling possible with one inactive torquer. In fact, while there was a slight increase in settling time, pointing accuracy was often improved with a torquer out. The stability of the malfunctioning system depended highly on the desired orientation. For instance, Figure 5.33 below shows a simulation with the axis 2 torquer out.

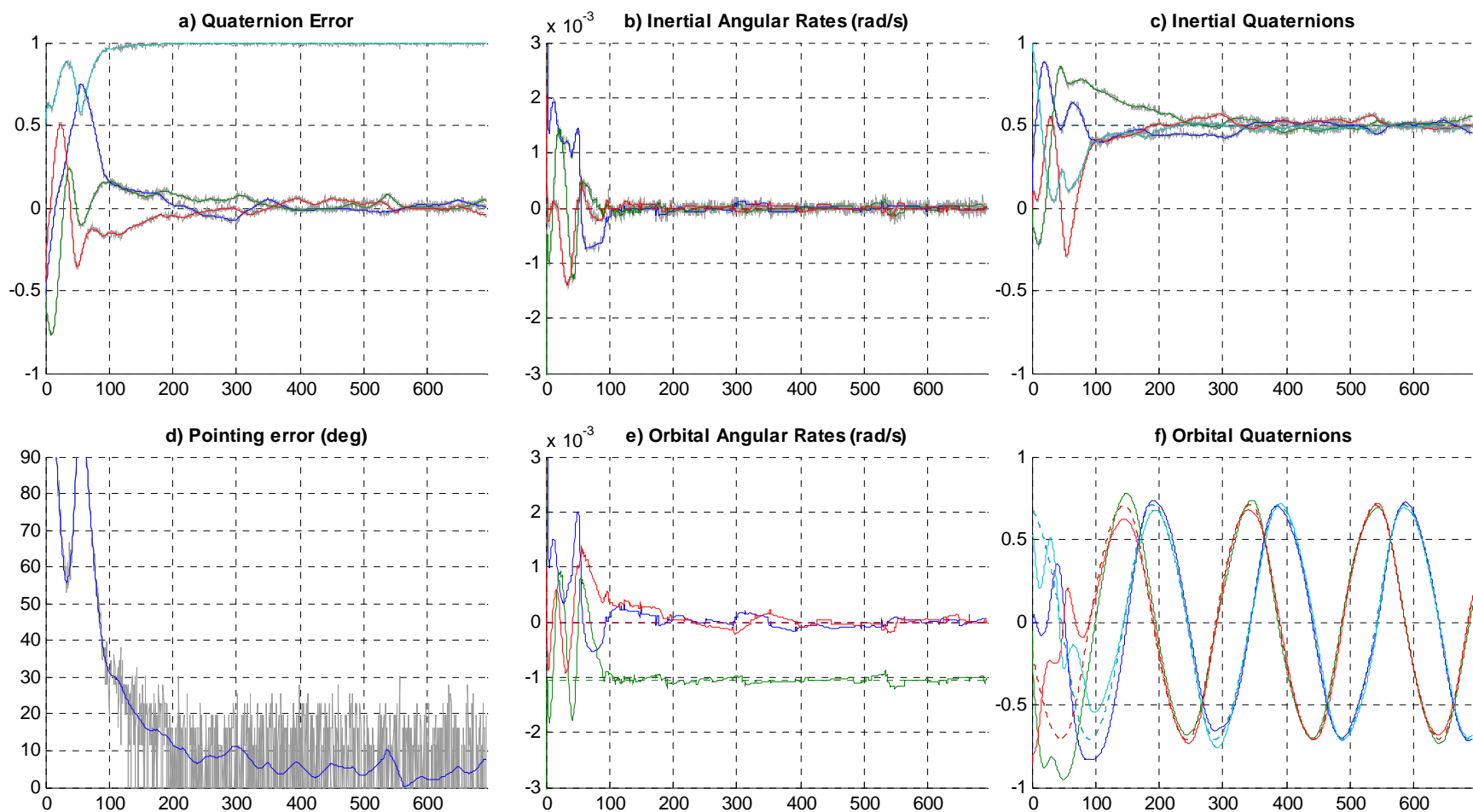


Figure 5.33: 3-axis, $C_1 = 3e-2$, $C_2 = 2e-5$, 7 orbits, b_2 torquer out

As can be seen in the figure, stability and accuracy are actually improved by deactivating the second torquer axis. The same is true when the third axis is set to zero. Since each torquer torques about both in-plane axes, the improved performance may be due to less interference between torquers. If the first axis torquer is deactivated, however, accuracy is dramatically decreased.

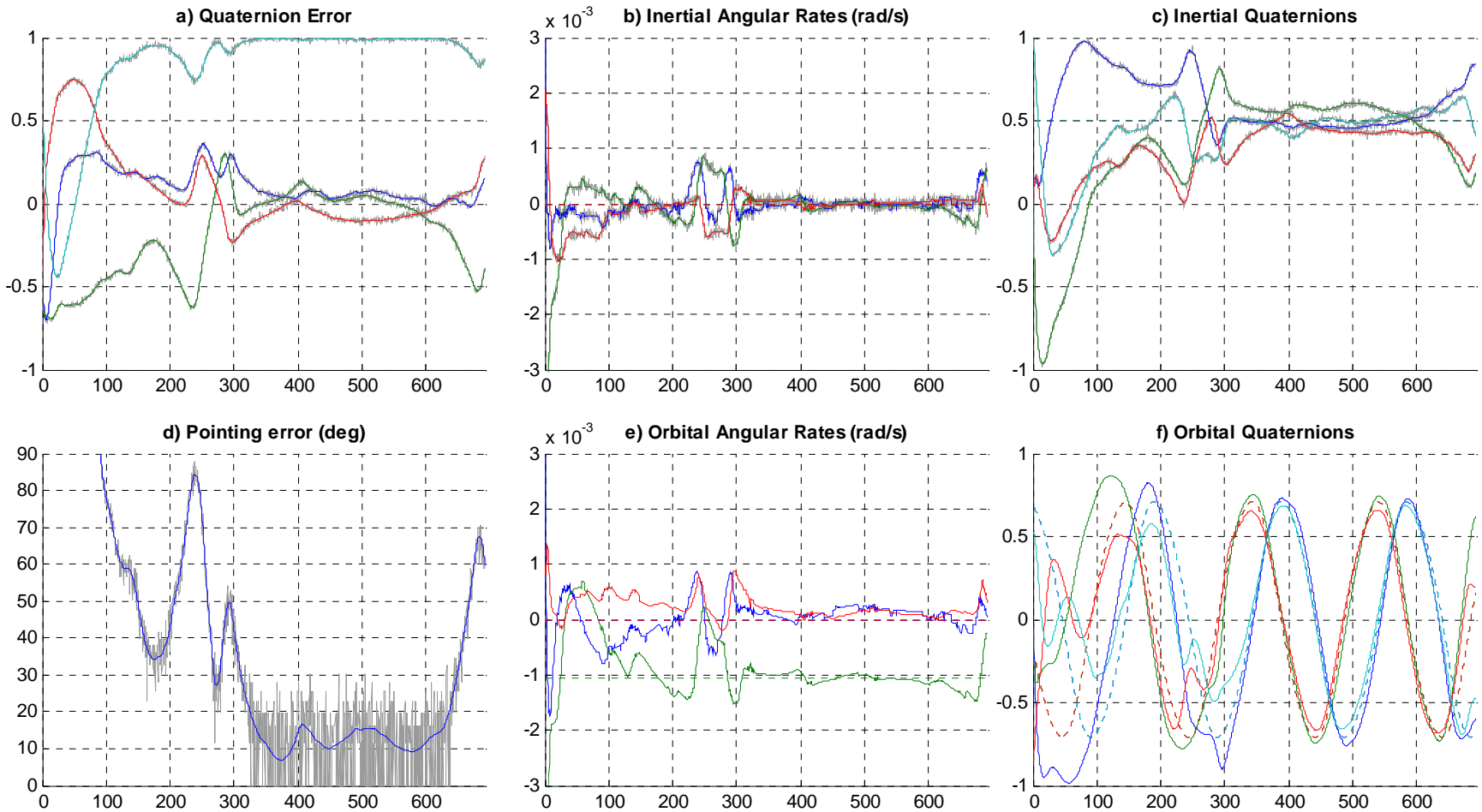


Figure 5.34: 3-axis, $C_1 = 3e-2$, $C_2 = 2e-5$, b_1 torquer out

While the system is not entirely unstable, it does have a tendency to periodically spike away from the desired. This problem can be alleviated by using a different desired vector. It is not entirely clear why this occurs, but it is probably related to the rotation of the local magnetic field as the spacecraft orbits and which direction the inactive axis is attempting to point towards.

It was found that the system is capable of handling the failure of any one of the torquers and still achieving accuracies similar to the fully functional state. Certain torque axes are required for complete stability about certain orientations though, so with a failed torquer not all desired orientations are possible. Conversely, certain orientations experienced an increase in pointing accuracy due to torquer failure. Further study should be made into this phenomenon in order to investigate its possible usefulness in increasing stability as well as to investigate the interaction between the spacecraft and magnetic field.

5.2.7 Commanding Different Quaternions

Although it has not yet been demonstrated, the controller has the capability of pointing the spacecraft to any direction in either the orbital or inertial frames. The desired orientation had little effect on the settling time or pointing accuracy in all cases except for the torquer out case above. Figure 5.35 below demonstrates how the system performs similarly with a different desired orientation. It also was done for the axis 1 torquer out to illustrate how the desired orientation and the axis of the inactive torquer relate to settling.

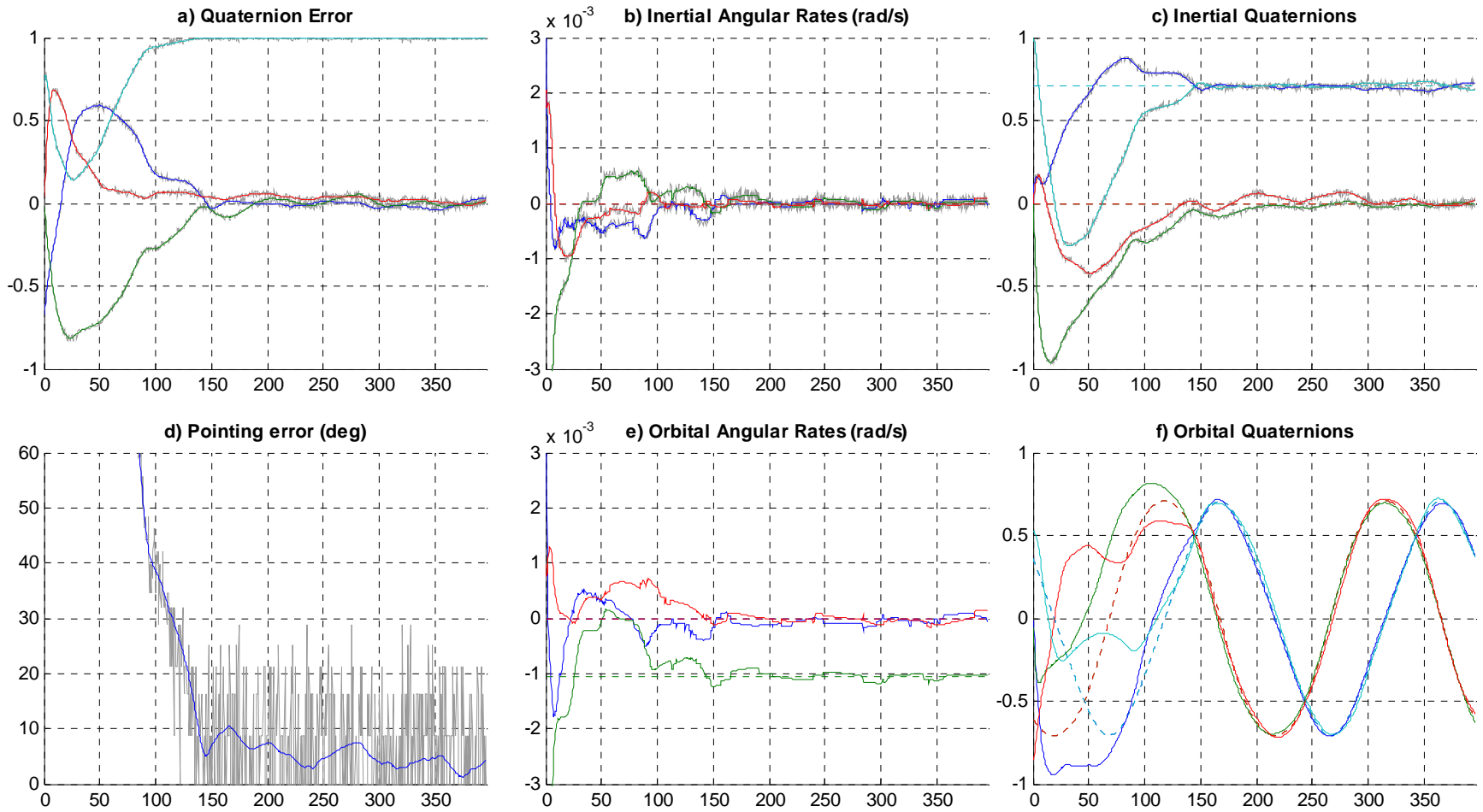


Figure 5.35: 3-axis, same parameters as Figure 5.34, $q_d = [\sqrt{2}/2 \quad 0 \quad 0 \quad \sqrt{2}/2]$

This desired vector represents a rotation of 90° about the b_1 axis so that the b_1 axis is still aligned with the i_1 axis. In the previous, unstable version of Figure 5.34, the desired vector had the b_1 axis aligned with the $-i_2$ axis. As before, the system settles to less than 10° within two orbits.

5.2.8 Commanding in the Orbital Frame

The controller also has the capability of commanding a rotation so that it aligns with points in the orbital frame. This would allow Earth-related experiments to occur or the usage of a high gain antenna for increased bandwidth. In general, performance was similar to that in the inertial frame as long as the gains were slightly lowered. By lowering the gains, similar settling errors were achieved at a trade off of slightly longer settling times.

Commands in the orbital frame were even more susceptible to low resolutions and high noise levels than in the inertial frame, probably because a non-zero angular velocity and constantly changing desired quaternion vector are required.

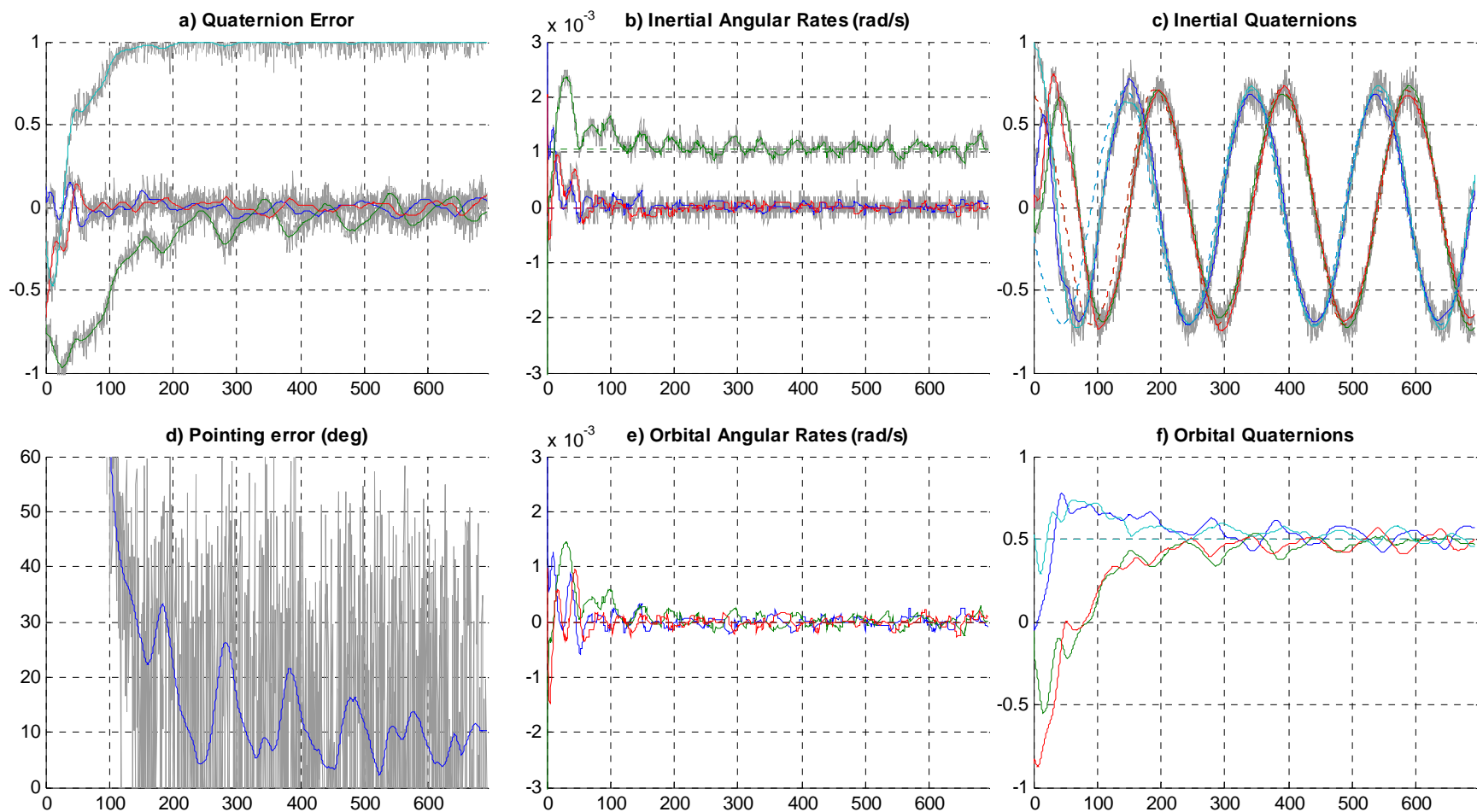


Figure 5.36: Orbital frame, $C_1 = 2\text{e-}2$, $C_2 = 1\text{e-}5$

With the relatively high noise levels here, the system needs a full seven orbits to settle. Response time can be improved to approximately one orbit with improved sensor accuracy and precision as shown below.

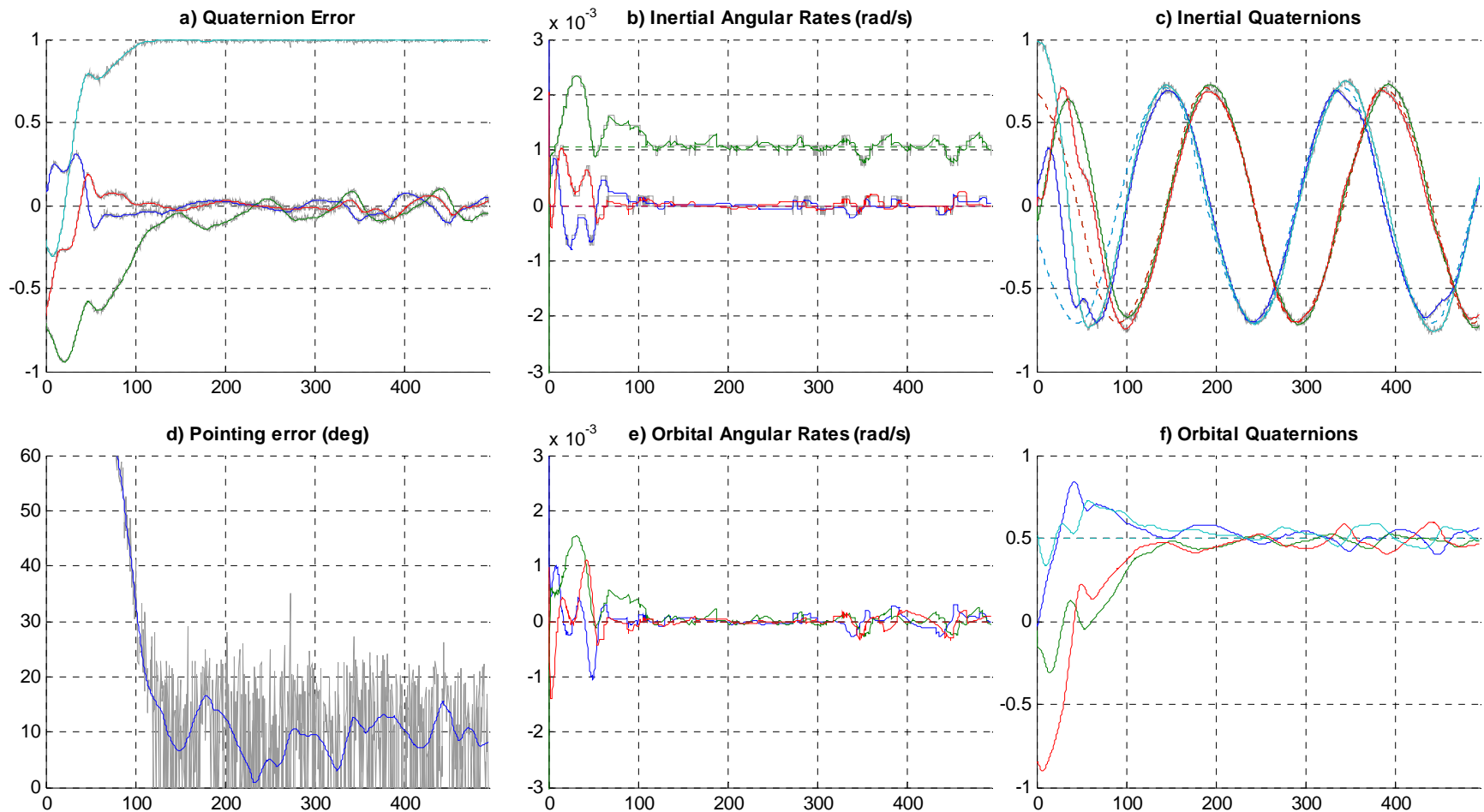


Figure 5.37: Orbital frame, $C_1 = 3e-2$, $C_2 = 2e-5$

With the resolutions from Figure 5.25 and fairly low noise levels, the system settles accuracies of about 15° in the orbital frame. The differences may also just be due to additional error introduced by the frame transformation of the desired vector. In that case it would just be a numerical artifact of the simulation and would not happen in the real world.

5.2.9 Three-Axis Conclusions

The controller was found to be much more sensitive to changes in any of the three control parameters, position gain, rate gain, and pulse time. All three parameters are coupled and must be optimized simultaneously. It is also important to know the spacecraft moments of inertia accurately for the simulated gains to apply. The algorithm performed well with low sensor resolutions, but the rate information was more critical than position. Dropping the resolution, of course, brought an inherent drop in accuracy. The system responded very well to noise and was able to maintain stability with signal-to-noise ratios in the 2:1 range. Controllability was limited when one torquer failed in that settling and accuracy depended on the desired orientation. Current consumption was very low, averaging less than $1/100^{\text{th}}$ the torquer ability, so the system should be able to handle the disturbance torques that were not included. In a fully functional satellite with reasonably good resolutions and low noise, accuracies of 10° - 20° should be achievable. Even so, the pointing error periodically dropped below 5° , so an algorithm could be written that waited for accuracy to increase before performing the experiment, taking a picture for example.

5.3 Comparison of B-dot and Three-Axis Controllers

In general, B-dot was a much simpler, more robust algorithm that could handle several simultaneous failures with relatively little drop in performance. The three-axis algorithm was much more complicated and susceptible to failure. The responses were highly non-linear and generally not intuitively predictable. On the other hand, it did have a relatively good response to

extremely unlikely resolutions and noise levels. The table below summarizes the differences between the two algorithms.

Table 5.3: Comparison of B-dot and three-axis algorithms

	B-dot	Three-axis
<i>Calculation steps</i>	3	5/7 steps
<i>Calculation type</i>	Arithmetic	Matrix algebra
<i>Gain sensitivity</i>	Low	High
<i>Calc. frequency</i>	2-10 sec	15-25 sec
<i>Settling time</i>	<1 orbit	Up to 5 orbits
<i>Ave current draw</i>	100-200 mA	<1mA
<i>Noise Response</i>	Great	Good
<i>Torquer out</i>	Unaffected	Ltd controllability
<i>Main Strength</i>	Fail-safe	Accuracy

In comparing them, it is important to remember that both algorithms are necessary for a complete controller package. The three-axis controller is not designed to work with high rates, while B-dot is not capable of achieving and level of pointing accuracy.

6 FUTURE WORK

While hopefully this thesis has answered several questions, it has raised several more, and there is still much more investigation to be done. There are a few hardware-related experiments whose data would improve simulation accuracy. This value could then be plugged into the simulation for disturbance torque calculation. First, its mass moments of inertia and principal angles could be determined either through measurement or improving the accuracy of the solid model. Second, the sensor models for the rates and quaternions should be refined once the actual hardware is chosen. Finally, the spacecraft's residual magnetic dipole while in a power-on operational state could be measured. Simulation accuracy could be improve by including the remaining principal disturbance torques.

Further investigation should be made into improving the three-axis control algorithm. Hopefully, some form of numerical position error integration feedback can be found that would improve the steady state performance. The problem with such a system would be finding a method that is capable of being implemented with the limited computing power available onboard. Additionally, the periodic fluctuation of the magnetic field varied effective gain which in turn caused an oscillation in the pointing accuracy. This problem might be mitigated by making the gains a function of the local magnetic field vector. Finally, as the spacecraft settles out near the desired orientation, the system becomes linear enough that this type of analysis is valid. A third controller could be developed based on linear control theory which would take over for additional pointing refinement.

Even with the simulation the way it is, there is more research to be done. The magnetorquer current information could be used power consumption analysis to help refine the satellite's power budget. Also, the torquer-out performance was not completely explored here. The apparent performance enhancement for some orientations should be investigated. Perhaps a two-torquer system could be used intentionally where the deactivated torquer is chosen based on the desired orientation. Finally, upon completion of the determination simulation, this work should be merged with it into one coherent ADCS simulation.

BIBLIOGRAPHY

1. Wertz, James R., ed. Spacecraft Attitude Dynamics and Control. El Segundo, CA: Kluwer Academic Publishers, 1978.
2. International Geomagnetic Reference Field (IGRF). Accessed June 10, 2005; Revised March 22, 2005; available from <http://www.ngdc.noaa.gov/AGA/vmod/igrf.html>.
3. Wertz, James R., and Wiley J. Larson, eds. Space Mission Analysis and Design (SMAD) 3rd Edition. El Segundo, CA: Microcosm Press, 1999.
4. Svartveit, Kristian. "Attitude Determination of the NCUBE Satellite." Thesis prepared for NTNU, Norway: June 2003.
5. Graversen, Torben, et al. "Attitude Control System for AAU CubeSat." Thesis prepared for Aalborg University, Denmark: 6 June 2002.
6. Guelman, M., et al. "Design and Testing of Magnetic Controllers for Satellite Stabilization." Acta Astronautica Vol. 56 (2005): 231-239.
7. Tivey, Maurice A., "Ocean Bottom Magnetology Laboratory: Magnetic Analysis Code." Accessed June 10, 2005; Revised April 2005; available from <http://deeptow.whoi.edu/matlab.html>.
8. Sidi, Marcel J. Spacecraft Dynamics and Control. Cambridge: Cambridge University Press, 2000.

Appendix A: Magfd.m

This is the program developed by Maurice Tivey at the Woods Hole Marine Magnetism Group⁷ which returns the estimated magnetic field vector at any point in space and time based on the IGRF-10 developed by the IAGA.²

```
function J=magfd (DATE, ITYPE, ALT, COLAT, ELONG)
% MAGFD
% Function to compute Earths magnetic field
% and components: X,Y,Z,T for a given latitude
% and longitude, date and altitude.
% Uses MATLAB MAT files sh1900.mat to sh2005.mat in 5 yr
% intervals.
%
% Usage: out=magfd (DATE, ITYPE, ALT, COLAT, ELONG) ;
%
% DATE = date of survey (decimal years)
% ITYPE=1 for geodetic to geocentric (USE 1)
% ALT = altitude of survey relative to sealevel (km +ve up)
% COLAT=90-latitude (decimal degrees)
% ELONG=longitude of survey (decimal degrees)
%
% Output array out contains components X,Y,Z,T in nanoteslas
% X north component
% Y east component
% Z vertical component +ve down
% T total field magnitude
%
% ref: IAGA, Division V, Working Group 8,
% International geomagnetic reference field, 1995
% revision, Geophys. J. Int, 125, 318-321, 1996.
% IGRF2000
% IAGA Working Group V-8 (Chair: Mioara Manda, Institut de
% Physique du Globe de Paris, 4 Place Jussieu, 75252 Paris,
% France. Fax:33 238 339 504, email: mioara@ipgp.jussieu.fr).
% http://www.dsri.dk/Oersted/Field_models
%
% Maurice A. Tivey March 1997
% Mod Dec 1999 (add igrf2000 and y2k compliance
% Mod Nov 2000 (use up to degree 10 sh coefficients)
% Mod Apr 2005 added 2005 coeffs
% http://deeptow.whoi.edu/matlab.html
% Copyright: Maurice A. Tivey, 2005
% Woods Hole Oceanographic Institution

if nargin < 1
    disp('DEMO MAGFD:')
    help magfd
    disp('Compute magnetic field at Woods Hole from Jan 1st 1900');
    disp(' every five years until 2005');
    disp(' Latitude 42 N, Longitude 74W')
    disp('sample command: out=magfd(1997,1,0,90-42,-74);')
    for i=1:22,
        out(i,:) = magfd(-(i-1)*5+1900,1,0,90-42,-74);
```

```

end
plot([1:22]-1)*5+1900,out(:,4),'-r+','linewidth',2);
xlabel('Year');
ylabel('Total Magnetic Field (nT)')
title('Total Magnetic Field Intensity at Woods Hole, MA')
axis tight
return
end

%igrfyear=2000;
%igrffile='sh2000';
%DGRF=[1900:5:2000];
DGRF=[1900:5:2005];
igrfyear=2005;
igrffile='sh2005';
pl=0;
if DATE < 0, pl=1; end
DATE=abs(DATE);
% Determine year for base DGRF to use.
if DATE < igrfyear,
    BASE=fix(DATE-DGRF(1));
    i=fix(BASE/5)+1;
    BASE=DGRF(i);
    if pl==0,
        fprintf('Using DGRF base year %f \n',BASE);
    end
    eval(['load sh',num2str(BASE)])
    % loads agh and agh41 but now need to get
    iagh=agh;iagh41=agh41;
    % load next epoch
    eval(['load sh',num2str(DGRF(i+1))])
    eagh=agh;eagh41=agh41;
    dgh=(eagh-iaqh)./5;dgh41=(eagh41-iagh41)./5;
    aqh=iaqh;aqh41=iagh41;
    clear iagh iagh41 eagh eagh41
    T = DATE - BASE;
else
%   if pl==0,
%       fprintf('Using IGRF base year %f \n',igrfyear);
%   end
    eval(['load ',igrffile])    % load in igrf data file
    T = DATE - igrfyear;
end
% combine spherical harmonic coefficients from first 8 degrees
% with degrees 9 and 10
agh=[agh,agh41];
dgh=[dgh,dgh41];
%
    D2R    = pi/180;
    R      = ALT;
    ONE    = COLAT*0.01745329;
    SLAT   = cos(ONE);
    CLAT   = sin(ONE);
    ONE    = ELONG*0.01745329;
    CL(1)  = cos(ONE);
    SL(1)  = sin(ONE);
    X      = 0.0;
    Y      = 0.0;
    Z      = 0.0;
    CD     = 1.0;
    SD     = 0.0;
    L      = 1;
    M      = 1;
    N      = 0;

```

```

if ITYPE == 1 % CONVERSION FROM GEODETIC TO GEOCENTRIC COORDINATES
    A2 = 40680925.; % squared semi major axis
    B2 = 40408588.; % squared semi minor axis
    ONE = A2*CLAT*CLAT;
    TWO = B2*SLAT*SLAT;
    THREE = ONE + TWO;
    FOUR = sqrt(THREE);
    R = sqrt(ALT*(ALT + 2.0*FOUR) + (A2*ONE + B2*TWO)/THREE);
    CD = (ALT + FOUR)/R;
    SD = (A2 - B2)/FOUR*SLAT*CLAT/R;
    ONE = SLAT;
    SLAT = SLAT*CD - CLAT*SD;
    CLAT = CLAT*CD + ONE*SD;
end

RATIO = 6371.2/R;

%
% COMPUTATION OF SCHMIDT QUASI-NORMAL COEFFICIENTS P AND X(=Q)
%

P(1) = 2.0*SLAT;
P(2) = 2.0*CLAT;
P(3) = 4.5*SLAT*SLAT - 1.5;
P(4) = 5.1961524*CLAT*SLAT;
Q(1) = -CLAT;
Q(2) = SLAT;
Q(3) = -3.0*CLAT*SLAT;
Q(4) = 1.7320508*(SLAT*SLAT - CLAT*CLAT);

NMAX=10; % Max number of harmonic degrees
NPQ=(NMAX*(NMAX+3))/2;
for K=1:NPQ,
    if N < M
        M = 0;
        N = N + 1;
        RR = RATIO^(N + 2);
        FN = N;
    end
    FM = M;
    if K >= 5 %8,5,5
        if (M-N) == 0 %7,6,7
            ONE = sqrt(1.0 - 0.5/FM);
            J = K - N - 1;
            P(K) = (1.0 + 1.0/FM)*ONE*CLAT*P(J);
            Q(K) = ONE*(CLAT*Q(J) + SLAT/FM*P(J));
            SL(M) = SL(M-1)*CL(1) + CL(M-1)*SL(1);
            CL(M) = CL(M-1)*CL(1) - SL(M-1)*SL(1);
        else
            ONE = sqrt(FN*FN - FM*FM);
            TWO = sqrt((FN - 1.0)^2 - FM*FM)/ONE;
            THREE = (2.0*FN - 1.0)/ONE;
            I = K - N;
            J = K - 2*N + 1;
            P(K) = (FN + 1.0)*(THREE*SLAT/FN*P(I) - TWO/(FN - 1.0)*P(J));
            Q(K) = THREE*(SLAT*Q(I) - CLAT/FN*P(I)) - TWO*Q(J);
        end
    end

%
% SYNTHESIS OF X, Y AND Z IN GEOCENTRIC COORDINATES
%
end
ONE = (agh(L) + dgh(L)*T)*RR;

if M == 0 %10,9,10
    X = X + ONE*Q(K);
    Z = Z - ONE*P(K);
    L = L + 1;
end

```

```

else
    TWO    = (agh(L+1) + dgh(L+1)*T)*RR;
    THREE  = ONE*CL(M) + TWO*SL(M);
    X      = X + THREE*Q(K);
    Z      = Z - THREE*P(K);
    if CLAT > 0 %12,12,11
        Y = Y + (ONE*SL(M) - TWO*CL(M))*FM*P(K) / ((FN + 1.0)*CLAT);
    else
        Y = Y + (ONE*SL(M) - TWO*CL(M))*Q(K)*SLAT;
    end
    L      = L + 2;
end
M      = M + 1;
end
%      CONVERSION TO COORDINATE SYSTEM SPECIFIED BY ITYPE
ONE    = X;
X      = X*CD + Z*SD;
Z      = Z*CD - ONE*SD;
T      = sqrt(X*X + Y*Y + Z*Z);
J=[X,Y,Z,T];
%      END

```

Appendix B: CP2 Magnetometer Calibration Data

This data is based on the calibration tests performed on the flight hardware using a fluxgate magnetometer for baseline data.

Table B.1: Calibration data for CP2 flight panels

a (T/bit)	b (T)	Board	Face	HMC1052 Axis	Body Axis
4.50E-07	-5.93E-05	FVII	Front	A	(+X)
4.29E-07	-4.75E-05	FVII	Front	B	(+Z)
4.40E-07	-5.45E-05	SXVIII	Left	A	(-Y)
4.33E-07	-5.26E-05	SXVIII	Left	B	(-Z)
4.92E-07	-5.68E-05	SXX	Right	A	(-Y)
4.61E-07	-5.79E-05	SXX	Right	B	(+Z)
4.16E-07	-5.60E-05	SXXI	Top	A	(-Y)
3.98E-07	-5.07E-05	SXXI	Top	B	(-X)
4.38E-07	-5.58E-05	SXXII	Bottom	A	(-Y)
4.26E-07	-5.50E-05	SXXII	Bottom	B	(+X)

Appendix C: Orbit Propagation and Attitude Simulator

This is the code used for all the attitude simulation results in Section 5. It was originally designed as an orbit propagator, solar panel power calculator, and B-dot simulation by fellow graduate student Erick Sturm over the summer of 2004. The author has modified to streamline the code and added the three-axis controller, hardware models, frame transformations, problem-specific plots, and other modifications for enhanced functionality.

```
%=====
%=====
%   Author:      Erick Sturm
%   Date:        July 2004
%   Program:     Polysat Orbit Propagator & Attitude Simulator
%=====
%   Description:
%       This program was initially created to take the
%       NASA TLEs of a cubesat and use them to determine
%       the lat and long of the cubesat at another date.
%=====
%   Revised:     Dan Guerrant
%   Date:        September 2004-June 05
%   This version is OPAS with my bug fixes and:
%   0. Minus Solar Power and Current calc. (OPASquick)
%   1. 3-axis stabilization (zeros rates) (OPAS3axis1)
%   2. 3-axis control (zeros quaternions/aligns body,inertial frames)
%       (OPAS3axis2)
%   3. Allows user to input quaternions in inertial frame to point to.
%       (OPAS3axis3)
%   4. Adds ability to point to quaternions in orbital frame. (OPAS3axis4)
%   5. Bug fixes quaternion error. Attitude sim in previous versions
%       incorrect. Still having trouble w/ control in orbital frame. Debug
%       version where desired torques inputted directly into attitude sim.
%       (OPAS3axis5, April 05)
%   6. More accurately models sensors. Omega I>0 transform finally
%       working. Includes GG disturbance. (OPAS3axis6, June 05)
%   7. Creates different plots based on control law in use. Fixed error
%       in current limiter. (OPAS3axisFinal, June 05)
%=====

function OPAS
close all;warning off MATLAB:singularMatrix;%clc
start = clock; %Store starting time for run time calculation

%=====
%Scan in the Data from the NASA TLE
%=====
%Specs for our supposed orbit: rp=660 ra=760 i=98 raan=22:30

fid = fopen('CP2TLE.txt','rb');
L0 = fgetl(fid);
L1 = fscanf(fid,'%d%6d%*c%5d%*3c%2d%f%f%5d%*c%*d%5d%*c%*d%5d', [1,10]);
```

```

L2 = fscanf(fid,'%d%d%f%f%f%f%f', [1,8]);
fclose(fid);

eY0 = L1(1,4); %Epoch Year
eD0 = L1(1,5); %Epoch Day
nD0 = L1(1,6)*4*pi/(24*3600)^2; %First Derivative of Mean Motion (rad/sec2)
nD20 = L1(1,7)*12*pi/(24*3600)^3; %Second Derivative of Mean Motion (rad/sec3)
D0 = L1(1,8); %Drag Term / Radiation Pressure Term
i0 = L2(1,3)*pi/180; %Inclination (rads)
Om0 = L2(1,4)*pi/180; %Right Ascension of the Ascending Node (rads)
e0 = L2(1,5)/1e7; %Eccentricity
om0 = L2(1,6)*pi/180; %Argument of Perigee (rads)
M0 = L2(1,7)*pi/180; %Mean Anomaly (rads)
n0 = L2(1,8)*2*pi/24/3600; %Mean Motion (rad/sec)

%=====
%Constants
%=====

Re = 6378.13649; %Equatorial Radius of the Earth (km)
mu = 3.986004415e5; %Gravitational Constant of the Earth (km3/s2)
we = 7.2921158553e-5; %Angular Velocity of the Earth (rad/s)
oe = 0.40909262967; %Obliquity of the Eccliptic (rad)
ne = 1.9909887984e-7; %Mean Motion of the Earth (rad/s)
Pmax = 1; %Maximum Solar Panel Power (W)
Ps = 1367; %Solar Radiation Power (W/m2)
t0o = 0; %Simulation Start Time
J2 = 0.00108263; %J2 Gravitational Perturbation Constant
Lv = 2*pi/180; %Elevation Angle required to see the S/C (rad)

%=====
%Define the Final Time
%=====

eYd = eY0+0; %Epoch Year Desired
eDd = eD0+0; %Epoch Day Desired
eHd = 01; %Epoch Hour Desired
eMd = 40; %Epoch Minute Desired
eSd = 00; %Epoch Second Desired

etf = eSd+60*(eMd+60*(eHd+24*(eDd+365.25*eYd))); %Epoch Time Final
eti = 60*(60*(24*(eD0+365.25*eY0))); %Epoch Time Initial

tfo = etf-eti; %Simulation Stop Time

% tspano=[t0o,tfo]; %Simulation Time Span fed into ode45

%=====
%Calculation of Time from Vernal Equinox
%=====

Yve = 04; %Epoch Year of Vernal Equinox
Dve = 79; %Epoch Day of Vernal Equinox
Hve = 06; %Epoch Hour of Vernal Equinox
Mve = 47; %Epoch Minute of Vernal Equinox
Sve = 00; %Epoch Second of Vernal Equinox

tve = Sve+60*(Mve+60*(Hve+24*(Dve+365.25*Yve))); %Epoch Time of Vernal Equinox
veo = 0;%-5.39; %Vernal Equinox Offset due to Equinox not happening @ 0:00 GMT

dti = eti-tve; %Initial Change in Time from Vernal Equinox
dtf = etf-tve; %Final Change in Time from Vernal Equinox

```



```

%=====
%Initial Condition Calculation
%=====

TLE = [i0;Om0;e0;om0;M0;n0]; %TLEs Loaded above
Keps = tle2keps(TLE,mu); %Convert TLEs to Keplerian Elements

a0 = Keps(1); %Semi-Major Axis (km)
e0 = Keps(2); %Eccentricity
nu0 = Keps(3); %True Anomaly (radians)
i0 = Keps(4); %Inclination (radians)
Om0 = Keps(5); %RAAN (radians)
om0 = Keps(6); %Arg of Perigee (radians)
P0 = a0*(1-e0^2); %Semi-Lattice Rectum (km)
r0 = P0/(1+e0*cos(nu0)); %Radius (km)
v0 = sqrt(mu*(2/r0-1/a0)); %Velocity (km/sec)
y0 = (nu0/abs(nu0))*acos((sqrt(mu*P0)/(r0*v0))); %Gamma (rad)
rD0 = v0*sin(y0); %Radial Velocity (km/sec)
nuD0 = v0*cos(y0)/r0; %Angular Velocity (rad/sec)

state0 = [n0;nD0;a0;e0;i0;Om0;om0;nu0;nuD0;r0;rD0]; %Initial State

%=====
%Orbit Propagation
%=====

tfo = .3*pi*sqrt(a0^3/mu); %Final Time for Orbit Propagator
options = odeset('RelTol', 1e-4);
[to,xo] = ode45(@oDiffEq,[t0o,tfo],state0,[],mu,J2,nD20,Re);

mm = xo(:,1); %Mean Motion (rad/s)
nD = xo(:,2); %First Derivative of Mean Motion (rad/s2)
a = xo(:,3); %Semi-Major Axis (km)
e = xo(:,4); %Eccentricity
i = xo(:,5); %Inclination (rad)
Om = xo(:,6); %RAAN (rad)
om = xo(:,7); %Arg of Perigee (rad)
nu = xo(:,8); %True Anomaly (rad)
nuD = xo(:,9); %Angular Velocity (rad/s)
r = xo(:,10); %Radius (km)
rD = xo(:,11); %Radial Velocity (km/s)

%=====
%Frame Transformations
%=====

xi=xo2xi(r,nu,om,Om,i); % Orbit 2 Inertial
xe=xi2xe(xi,to,dti,we,veo); % Inertial 2 Earth
rll = xe2rll(xe); % Earth 2 Lat, Long, & Radius

R = rll(:,1); %Radius to S/C
lat = rll(:,2); %Latitude of S/C
long = rll(:,3); %Longitude of S/C

%=====
%Find the Magnetic Field Vector using the IGRF Model
%=====

BL=rllt2BL(R,lat,long,to,eti,Re); %Mag-Field in Local N,E,Nadir (Teslas)
Be=xm2xe(BL,lat,long); %Mag-Field in Earth-Fixed
Bi=xe2xi(Be,to,dti,we,veo); %Mag-Field in Inertial

%Normalize the Mag-Field for Unit Vector Plot

```

```

for ndx=1:length(Bi)
    uBi(ndx,:)=Bi(ndx,:)/norm(Bi(ndx,:)); %Unit Mag-Field Vector in Inertial
Frame
end

%=====
%Create a Ground Track
%=====

%Create a Figure Window
f1=figure(1);
set(f1,'color','w','Renderer','zbuffer')
set(f1,'Name','Orbital Views')
set(f1,'units','normalized','position',[0 0 1 1])
% movegui(f1,'onscreen')

%Create the World Map Background and Ground Track Axes
World = imread('worldmap.jpg'); %Read World Map
imagesc([-180 180],[90 -90],World); hold; %Plot World Map
ax=gca;
set(ax,'YDir','normal')
grid on

%Algorithm to plot the Ground Track
[longm,latm]=col2mat(long,lat,i); %Convert Columns to Matrices
[m,n]=size(longm);
for ndx=1:n
    for mdx=2:m
        if longm(mdx,ndx)==0 & longm(mdx-1,ndx)~=0
            for k=1:(mdx-1)
                longp(k)=longm(k,ndx);
                latp(k)=latm(k,ndx);
            end
            plot(longp,latp,'Linewidth',2,'Color','r')
            clear longp;
            clear latp;
        elseif longm(m,ndx)~=0
            plot(longm(:,ndx),latm(:,ndx),'Linewidth',2,'Color','r')
        end
    end
end

%Find the Ground Area that can see the S/C
gai=r2gai(xi,Re,Lv);

%Algorithm to plot the Ground Area that can see the S/C
[galo,gala]=gai2gall(gai,to,dti,we,i,veo); %Convert above to Lat & Long
[m,n]=size(galo);
if n>1
    for ndx=1:n
        for mdx=2:m
            if galo(mdx,ndx)==0 & galo(mdx-1,ndx)~=0
                for k=1:(mdx-1)
                    galop(k)=galo(k,ndx);
                    galap(k)=gala(k,ndx);
                end
                plot(galop,galap,'Linewidth',1.25,'Color','g')
                clear galop;
                clear galap;
            elseif galo(m,ndx)~=0
                plot(galo(:,ndx),gala(:,ndx),'Linewidth',1.25,'Color','g')
            end
        end
    end
end
end

```

```

else
    plot(galo,gala,'linewidth',1.25,'Color','g');
end

%Plotting Cal Poly, SLO, CA
plot(-120.66512,35.30243,'rx')

%Defining Ground Track Axes Properties
title('Ground Track of the S/C')
axis([-180 180 -90 90])
set(a1,'xtick',[-180 -165 -150 -135 -120 -105 -90 -75 -60 -45 ...
               -30 -15 0 15 30 45 60 75 90 105 120 135 150 165 180])
set(a1,'ytick',[-90 -75 -60 -45 -30 -15 0 15 30 45 60 75 90])
set(a1,'units','normalized','position',[.3 .2 .6 .4])
set(a1,'xcolor','k','ycolor','k')
set(get(a1,'Title'),'FontWeight','bold','Color','k')

%=====
%Attitude Simulator
%=====

%S/C Properties-----
m = 1.00; %Mass (kg)
l = 0.10; %Length (m)
w = 0.09; %Width (m)
h = 0.11; %Height (m)

% I = 1/12*m*[(h^2+w^2);(l^2+h^2);(w^2+l^2)]; %Mass Moments of Inertia (kg-
m^2)
I = [8.817e-4; 9.804e-4; 10.35e-4]; %MMI from IDEAS model of CP2
K = [(I(2)-I(3))/I(1);
      (I(3)-I(1))/I(2);
      (I(1)-I(2))/I(3)];

%Simulation Setup-----
t0a = t0o; %Seconds to offset AtSim Start from OrProp Start
tfa = tfo; %Seconds to run AtSim
tr = 9.9; %Seconds taking readings
dtrc = 0.1; %Seconds between reading end and control start
tc = tr; %Seconds to have Torquers on [0.025,6.4]
dtcr = dtrc; %Seconds between control end and reading start

%Initial Conditions-----
% w0 = [0.005 -0.005 0.002]; %Conservative after BDot case (rad/s)
w0 = [1*pi/30 .05 -.05]; %Worst likely deployment case
q0 = [0 0 0 1]; %Initial Quaternion - Inertial->Body
state0 = [w0 q0]; %Initial State

%Desired State-----
frame = 0; %0 if desired given in inertial, 1 for orbital
switch 5 %Desired Quaternions (frame defined above)
    case 1, qd = [1 0 0 0]; %180 about b1
    case 2, qd = [0 1 0 0]; %180 about b2
    case 3, qd = [0 0 1 0]; %180 about b3
    case 4, qd = [0 0 0 1]; %Aligned
    case 5, qd = [0.5 0.5 0.5 0.5]; %120 about [1 1 1]
    case 6, qd = [0 0 sqrt(2)/2 sqrt(2)/2]; %90 about b3
    case 7, qd = [0 sqrt(2)/2 0 sqrt(2)/2]; %90 about b2
    case 8, qd = [sqrt(2)/2 0 0 sqrt(2)/2]; %90 about b1
end

if frame
    qdo = qd; %Desired Quaternions in orbital frame
    wdo = [0 0 0];

```

```

else
    qdi = qd;          %Desired Quaternions in inertial frame
    wdi = [0 0 0];
end

%Magnetometer Modeling Method-----
test = 5;             %Switch selects the test case listed below
switch test
    case 1             %Perfect 3-axis. No mag/pos/rate error, direct torque from
        control law.
    case 2             %3-axis. No mag/pos/rate error, control torque turned into
        mag commands.
    case 3             %3-axis CP3 sim.  Mag/pos/rate error, control torque to mag
        commands.
    case 4             %Perfect B-Dot sim.  No mag error.
    case 5             %CP3 B-dot sim.  Mag error.
    case 6             %CP2 B-dot sim.  Mag error, actual mag cal data
    case 7             %CP2 B-dot sim.  Mag error, actual mag cal data, b-dot w bits
        (as implimented)
end

if test >= 6
    %Actual CP2 callibration data from Side Test Data.xls
    CalData = [ % m      b
        4.50e-7    -5.93e-5;    %Front  Magnetometer Axis A (+X) FVII
        4.29e-7    -4.75e-5;    %Front  Magnetometer Axis B (+Z)
        4.40e-7    -5.45e-5;    %Left   Magnetometer Axis A (-Y) SXVIII
        4.33e-7    -5.26e-5;    %Left   Magnetometer Axis B (-Z)
        4.92e-7    -5.68e-5;    %Right  Magnetometer Axis A (-Y) SXX
        4.61e-7    -5.79e-5;    %Right  Magnetometer Axis B (+Z)
        4.16e-7    -5.60e-5;    %Top    Magnetometer Axis A (-Y) SXXI
        3.98e-7    -5.07e-5;    %Top    Magnetometer Axis B (-X)
        4.38e-7    -5.58e-5;    %Bottom Magnetometer Axis A (-Y) SXXII
        4.26e-7    -5.50e-5;    %Bottom Magnetometer Axis B (+X)
    ];
else
    % Ideal mag setup: 0=-500mG,128=0, 255=500mG
    % Tesla = m * Bit value + b
    CalData = [5e-5/128*ones(10,1) -5e-5*ones(10,1)];
end

StDvM = 2;           %Standard Deviation in Magnetometer Readings (Bits)
StDvG = 5e-5;        %Std Dev in gyro readings (rad/s)
StDvQ = 1e-2;        %Std Dev in quaternion readings from star tracker
Gres = 1e-4;         %Resolution of gyros(rad/s)
Qres = 1e-1;         %Resolution of quaternions
Ires = 0.0012;       %Resolution of Magnetorquer Current (Amps/Step)
Ilim = 0.3;          %Max current per torquer(Amps)

%Controller Parameters-----
N = 54;              %Number of Torquer Loops
A = .003;            %Average Area of Torquer Loops (m^2)
NA = 0.150622;       %Sum of area enclosed by each loop (~N*A)
C = 8e-3;            %Kyle's B-Dot Constant on CP2 (~Kk*CalData(:,1))
Kk = 20e3;           %C*128/5e-5; %B-Dot Controller Gain for CP3
(~C/CalData(:,1))
C1 = 20e-3;          %Rate gain
C2 = 10e-6;          %Quaternion gain

%Sim w/ Torquing-----

%Loop Initialization
tas = t0a;           %attitude simulation time
wbri = w0;           %Initial Omegas in the Body Frame during Readings

```

```

    gri = q0;          %Quaternions after torquers
    ndx = 1; mdx = 1; idx = 1;

while tas < tfa
    mub=[0;0;0];      %Magnetic Dipole generated by Torquers
    Treq=[0;0;0];

    %Attitude Sim of S/C During Readings
    [tar,stater]=ode45(@aDiffEq,[tas,tas+tr,tas+tr+dtrc],[wbri';gri'],...
        options,I,K,mub,to,Bi,Treq,test,mm);
    wbr=stater(:,1:3);      %Omegas in the Body Frame during Readings
    qr =stater(:,4:7);      %Quaternions during Readings
    wbc1=wbr(end,:);        %Initial Omegas in the Body Frame during
Torquing
    qci =qr(end,:);        %Initial Quaternions during Torquing

    % Mag-field and Attitude Measurments
    Bb=Bi2Bb(to,Bi,tar,qr);      %Mag-Field in Body Frame during Readings
(Tesla)
    if (test==1 | test==2 | test==4)
        Bbm = Bb;          %Measured Mag-Field (no error)
        wbrn = wbr(2,:);    %Measured angular rates (no error)
        qrn = qr(2,:);      %Measured quaternions (no error)
    else
        [BbmBit,Bbm] = magErr(Bb,CalData,StDvM);          %Measured
Mag-Field (error introduced)
        wbrn = roundto(wbr(2,:)+StDvG.*randn(size(wbr(2,:))),Gres); %Measured
angular rates (error introduced)
        qrn = roundto(qr(2,:)+StDvQ.*randn(size(qr(2,:))),Qres); %Measured
quaternions (error introduced)
    end

    %Algorithm to Allow Plotting of Measured Mag-Field
    taBm(idx:idx+2)=tar;
    Bm(idx:idx+2,1:3)=Bbm;B(idx:idx+2,1:3)=Bb;
    idx=idx+3;

    %Inertial to Orbital State Vector Transformation
    mm1 = interp1(to,mm,tar(2));      %Mean Motion(rad/s)
    theta = interp1(to,nu,tar(2));    %True Anomoly(rad)
    qoi = [0 0 sin(theta/2) cos(theta/2)]; %Orbital>Inertial rotation
    qio = [0 0 sin(-theta/2) cos(-theta/2)]; %Inertial>Orbital rotation
    qorb(mdx,:) = qtrans(qio,qr(2,:)); %Actual state in orbital frame
    worb(mdx,:) = wi2wo(wbr(2,:),qr(2,:),mm1); %Actual rates in orbital frame

    %%%%%%%%%%%%%%%%%%%%%%%%%%%%%%%%%%%%%%%%%%%%%%%%%%%%%%%%%%%%%%%%%%%%%%%%%
    %%%%%%%%%%%%%%%%%%%%%%%%%%%%%%%%%%%%%%%%%%%%%%%%%%%%%%%%%%%%%%%%%%%%%%%%%
    %%%%%%%%%%%%%%%%%%%%%%%%%%%%%%%%%%%%%%%%%%%%%%%%%%%%%%%%%%%%%%%%%%%%%%%%%
    %Find the error
    if frame          %Converts desired vector from orbital to
inertial
        qdi = qtrans(qoi,qdo);      %Desired quaternions in inertial frame
        wdi = wo2wi(wdo,qdo,mm1);  %Desired rates in inertial frame
    else
        %Converts desired vector from inertial to
orbital
        qdo = qtrans(qio,qdi);      %Desired quaternions in orbital frame
        wdo = wi2wo(wdi,qdi,mm1);  %Desired rates in orbital frame
    end
    qea(mdx,:) = qerr(qdi,qr(2,:)); %Calculate actual quaternion error
    qe = qerr(qdi,qrn);             %Quaternion error used by algorithm
    we = wbrn - wdi;                %Calculate rate error

    %Control Law
    Treq = -diag(I)*(C1.*we+C2.*qe(1:3))'; %Torque vector
requested

```

```

mub3a = (cross(Bbm(2,:)','Treq)./(norm(Bbm(2,:))^2)'); %Magnetic dipole
vector requested

%%%%%%%%%%%%%%%%%%%%%%%%%%%%%%%%%%%%%%%%%%%%%%%%%%%%%%%%%%%%%%%%%%%%%%%% B-Dot Controller %%%%%%%%%%%%%%%%%%%%%%%%%%%%%%%%%%%%%%%%%%%%%%%%%%%%%%%%%%%%%%%%%%%%%%%%%
if test==6 %BDot using mag bit values (as implimented on CP2)
    BDot = (BbmBit(2,:)-BbmBit(1,:))/(tar(2)-tar(1));
    mubBd = -C*BDot; %Magnetic dipole vector requested
else %BDot using mag bit values converted back to Tesla
    BDot = (Bbm(2,:)-Bbm(1,:))/(tar(2)-tar(1));
    mubBd = -Kk*BDot; %Magnetic dipole vector requested
end

%%%%%%%%%%%%%%%%%%%%%%%%%%%%%%%%%%%%%%%%%%%%%%%%%%%%%%%%%%%%%%%%%%%%%%%% Select active control law %%%%%%%%%%%%%%%%%%%%%%%%%%%%%%%%%%%%%%%%%%%%%%%%%%%%%%%%%%%%%%%%%%%%%%%%%
if test<=3
    mub = mub3a; %3-axis is active
    mub1 = mubBd;
else
    mub = mubBd; %B-dot is active
    mub1 = mub3a;
end

%%%%%%%%%%%%%%%%%%%%%%%%%%%%%%%%%%%%%%%%%%%%%%%%%%%%%%%%%%%%%%%%%%%%%%%% Current Limiter %%%%%%%%%%%%%%%%%%%%%%%%%%%%%%%%%%%%%%%%%%%%%%%%%%%%%%%%%%%%%%%%%%%%%%%%%
Ic = roundto(mub/(NA),Ires); %Current requested for the Torquers
(Amps)
while abs(Ic(1))>Ilim | abs(Ic(2))>Ilim | abs(Ic(3))>Ilim
    Ic = roundto(Ic./2,Ires); %Current provided to torquers
% disp('clip')
end
mub = Ic*NA;
%%%%%%%%%%%%%%%%%%%%%%%%%%%%%%%%%%%%%%%%%%%%%%%%%%%%%%%%%%%%%%%%%%%%%%%% End controller algorithms %%%%%%%%%%%%%%%%%%%%%%%%%%%%%%%%%%%%%%%%%%%%%%%%%%%%%%%%%%%%%%%%%%%%%%%%%

%Algorithm to Allow Plotting of B-Dot, Mag Dipole, and Required Current
taBD(mdx,1) = tar(2); BD(mdx,:) = BDot;
mdp(mdx,:) = mub; mdp1(mdx,:) = mub1;
qdip(mdx,:) = qdi; qdop(mdx,:) = qdo;
wdip(mdx,:) = wdi; wdop(mdx,:) = wdo;
wnp(mdx,:) = wbrn; qnp(mdx,:) = qrn;
qep(mdx,:) = qe; Ir(mdx,1:3) = Ic;
mdx=mdx+1;

%--Convergence Tests--
if test<=3 % Three-axis deadband shutoff
    if norm(we)<1e-3 & 2*180/pi*acos(qe(4))<4
% disp('Deadband')
        mub = [0;0;0];
    end
else
    if mdx>20 % B-dot shutoff
        normBD = mean([norm(BD(end,:)),norm(BD(end-1,:)),...
            norm(BD(end-2,:)),norm(BD(end-3,:)),norm(BD(end-4,:))]);
        if normBD<4e-8
            disp('Time to Converge (min)');disp(tas/60)
            disp('Norm BDot (T/s)');disp(norm(BDot))
            break
        end
    end
end
end

% %Inactive torquer tests
% mub(1) = 0;
% mub(2) = 0;

%Attitude Sim of S/C during Torquing
[tac,statec]=ode45(@aDiffEq,[tas+tr+dtrc,tas+tr+dtrc+tc],[wbci';qci'],...

```

```

options,I,K,mub,to,Bi,Treq,test,mm);
wbc=statec(:,1:3); %Omegas in the Body Frame during Torquing
qc =statec(:,4:7); %Quaternions during Torquing
wbri=wbc(length(tac),:); %Initial Omegas in the Body Frame during Readings
qri =qc(length(tac),:); %Initial Quaternions during Readings
tas=tac(length(tac)); %Increase Attitude Simulation Loop Time

%Algorithm to Create Plottable Vectors of Time, Omegas, and Quaternions
tan=[tar(1:length(tar)-1);tac(1:length(tac)-1)];
ta(ndx:ndx+length(tan)-1)=tan;
wbn=[wbr(1:length(tar)-1,1:3);wbc(1:length(tac)-1,1:3)];
wb(ndx:ndx+length(tan)-1,1:3)=wbn;
qn=[qr(1:length(tar)-1,1:4);qc(1:length(tac)-1,1:4)];
qi(ndx:ndx+length(tan)-1,1:4)=qn;
ndx=ndx+length(tan);
end

%Plotting the Results of the Simulation-----
f2=figure(2);
set(f2,'units','normalized','position',[0 0.18 1
0.75],'Color','w','Name','Detumbling Algorithm');
%Creates different plot layouts for 3-axis and B-dot results
if test <= 3
    a1=axes('parent',f2,'units','normalized','position',[.03 .55 .3
.4],'nextplot','add');
    plot(taBD./60,qep,'Color',[.6 .6 .6]);plot(taBD./60,qea);
    title('a') Quaternion
    Error','FontWeight','Bold','Color','k');set(gca,'YLim',[-1 1])
    a2=axes('parent',f2,'units','normalized','position',[.37 .55 .3
.4],'nextplot','add');
    plot(taBD./60,wmp,'Color',[.6 .6 .6]);
    plot(ta./60,wb);plot(taBD./60,wdip,':');%set(gca,'YLim',[-3e-3 3e-3])
    title('b') Inertial Angular Rates
    (rad/s)','FontWeight','Bold','Color','k');
    a3=axes('parent',f2,'units','normalized','position',[.7 .55 .3
.4],'nextplot','add');
    plot(taBD./60,qnp,'Color',[.6 .6 .6]);
    plot(taBD./60,qdip,':');plot(ta./60,qi);
    title('c') Inertial
    Quaternions','FontWeight','Bold','Color','k');set(gca,'YLim',[-1 1])
    a4=axes('parent',f2,'units','normalized','position',[.03 .05 .3
.4],'nextplot','add');
    plot(taBD./60,2.*180./pi.*acos(qep(:,4)),'Color',[.6 .6 .6]);
    plot(taBD./60,2.*180./pi.*acos(qea(:,4)));set(gca,'YLim',[0 60])
    title('d') Pointing error (deg)','FontWeight','Bold','Color','k');
    % plot(taBD,mdpl,':'); %'Color',[.6 .6 .6]);plot(taBD./60,mdp);
    % plot(taBD./60,Ir);set(gca,'YLim',[-Ilim Ilim])
    % title('d') Torquer Current Provided
    (A)','FontWeight','Bold','Color','k');
    a5=axes('parent',f2,'units','normalized','position',[.37 .05 .3
.4],'nextplot','add');
    plot(taBD./60,wordb);plot(taBD./60,wdop,':');%set(gca,'YLim',[-3e-3 3e-3])
    title('e') Orbital Angular Rates (rad/s)','FontWeight','Bold','Color','k');
    a6=axes('parent',f2,'units','normalized','position',[.7 .05 .3
.4],'nextplot','add');
    plot(taBD./60,qdop,':');plot(taBD./60,qorb);
    title('f') Orbital
    Quaternions','FontWeight','Bold','Color','k');set(gca,'YLim',[-1 1])
else
    a1=axes('parent',f2,'units','normalized','position',[.03 .55 .3
.4],'nextplot','add');
    plot(to./60,Bi);
    title('a') Magnetic Field in Orbital Frame
    (T)','FontWeight','Bold','Color','k');

```

```

        a2=axes('parent',f2,'units','normalized','position',[.37      .55      .3
.4], 'nextplot','add');
        plot(taBm./60,Bm,'Color',[.6 .6 .6]);plot(taBm./60,B);
        title('b) Magnetic Field in Body Frame
(T)', 'FontWeight','Bold','Color','k');
        a3=axes('parent',f2,'units','normalized','position',[.7      .55      .3
.4], 'nextplot','add');
        plot(taBD./60,BD);
        title('c) B-dot (T/sec)', 'FontWeight','Bold','Color','k');
        a4=axes('parent',f2,'units','normalized','position',[.03      .05      .3
.4], 'nextplot','add');
        plot(taBD./60,Ir);set(gca,'YLim',[-Ilim Ilim])
        title('d) Torquer Current Provided (A)', 'FontWeight','Bold','Color','k');
        a5=axes('parent',f2,'units','normalized','position',[.37      .05      .3
.4], 'nextplot','add');
        % plot(ta./60,[wb sqrt(wb(:,1).^2+wb(:,2).^2+wb(:,3).^2)]); %Includes
magnitude
        plot(ta./60,wb);
        set(gca,'YLim',[-.01 .01], 'YTick',-.01:0.002:.01);
        title('e) Inertial Angular Rates
(rad/s)', 'FontWeight','Bold','Color','k');
        a6=axes('parent',f2,'units','normalized','position',[.7      .05      .3
.4], 'nextplot','add');
        plot(ta./60,qi);
        title('f) Inertial
Quaternions', 'FontWeight','Bold','Color','k');set(gca,'YLim',[-1 1])
end
set(a1,'XLim',[0
tas./60], 'xgrid','on', 'ygrid','on', 'Color','w', 'xcolor','k', 'ycolor','k', 'zcol
or','k');
set(a2,'XLim',[0
tas./60], 'xgrid','on', 'ygrid','on', 'Color','w', 'xcolor','k', 'ycolor','k', 'zcol
or','k');
set(a3,'XLim',[0
tas./60], 'xgrid','on', 'ygrid','on', 'Color','w', 'xcolor','k', 'ycolor','k', 'zcol
or','k');
set(a4,'XLim',[0
tas./60], 'xgrid','on', 'ygrid','on', 'Color','w', 'xcolor','k', 'ycolor','k', 'zcol
or','k');
set(a5,'XLim',[0
tas./60], 'xgrid','on', 'ygrid','on', 'Color','w', 'xcolor','k', 'ycolor','k', 'zcol
or','k');
set(a6,'XLim',[0
tas./60], 'xgrid','on', 'ygrid','on', 'Color','w', 'xcolor','k', 'ycolor','k', 'zcol
or','k');

disp('Run Time(s)');disp(etime(clock,start))

i = 0; %Avoid displaying NaN's from very last cycle
while isnan(wb((end-i),1))
    i = i+1;
end
disp('Final Inertial Quaternians and Rates(deg/s then rad/s)');
disp(qi((end-i),:));disp([wb((end-i),:) norm(wb((end-i),:)).*180./pi];
disp([wb((end-i),:) norm(wb((end-i),:))])
disp('Final Orbital Quaternians and Rates(deg/s then rad/s)');
disp(qorb((end-1),:));disp(worb((end-1),:).*180./pi)
disp('Quaternion Error')
disp(qea(end-1,:))
disp('Pointing Accuracy (deg)')
disp(2*180/pi*acos(qea((end-1),4)))
beep

%=====

```



```

q = [
    qd(4)    qd(3)   -qd(2)   -qd(1);
    -qd(3)    qd(4)    qd(1)   -qd(2);
    qd(2)    -qd(1)    qd(4)   -qd(3);
    qd(1)    qd(2)    qd(3)    qd(4)
];

qe = (q*[qa(1);qa(2);qa(3);qa(4)])';

%=====

function qt = qtrans(q1,q2)

% Returns sum of two successive quaternion rotations
q = [
    q2(4)    q2(3)   -q2(2)    q2(1);
    -q2(3)    q2(4)    q2(1)    q2(2);
    q2(2)    -q2(1)    q2(4)    q2(3);
    -q2(1)    -q2(2)   -q2(3)    q2(4)
];

qt = (q*[q1(1);q1(2);q1(3);q1(4)])';

%=====

function wo = wi2wo(w,q,mm)

%Converts angular rates from inertial to orbital
T = [
    1-2*(q(2)^2+q(3)^2)                2*(q(1)*q(2)+q(3)*q(4))        2*(q(1)*q(3)-
q(2)*q(4));
    2*(q(1)*q(2)-q(3)*q(4))                1-2*(q(1)^2+q(3)^2)
2*(q(2)*q(3)+q(1)*q(4));
    2*(q(1)*q(3)+q(2)*q(4))                2*(q(2)*q(3)-q(1)*q(4))        1-
2*(q(1)^2+q(2)^2)
];

wo = ([w(1);w(2);w(3)]-T*[0;0;mm])';

%=====

function wi = wo2wi(w,q,mm)

%Converts angular rates from orbital to inertial
T = [
    1-2*(q(2)^2+q(3)^2)                2*(q(1)*q(2)+q(3)*q(4))        2*(q(1)*q(3)-
q(2)*q(4));
    2*(q(1)*q(2)-q(3)*q(4))                1-2*(q(1)^2+q(3)^2)
2*(q(2)*q(3)+q(1)*q(4));
    2*(q(1)*q(3)+q(2)*q(4))                2*(q(2)*q(3)-q(1)*q(4))        1-
2*(q(1)^2+q(2)^2)
];

wb = ([w(1);w(2);w(3)]+T*[0;0;mm])';

%=====

function xi=xo2xi(r,nu,om,Om,i)

%Converts from Orbit Frame to Inertial Frame in Orbit Propagator
uo = r.*cos(nu+om);
vo = r.*sin(nu+om);
ui = uo.*cos(Om)-vo.*cos(i).*sin(Om);
vi = uo.*sin(Om)+vo.*cos(i).*cos(Om);

```

```

wi = vo.*sin(i);
xi = [ui,vi,wi];

%=====

function xe=xi2xe(xi,t,dti,wie,veo)

%Converts from Inertial Frame to Earth Frame

ui = xi(:,1);
vi = xi(:,2);
wi = xi(:,3);

off=veo*3600*wie;

for ndx = 1:length(xi)
    ue(ndx)
    cos((wie)*(t(ndx)+dti)+off)*ui(ndx)+sin((wie)*(t(ndx)+dti)+off)*vi(ndx);
    ve(ndx)
    sin((wie)*(t(ndx)+dti)+off)*ui(ndx)+cos((wie)*(t(ndx)+dti)+off)*vi(ndx);
    we(ndx) = wi(ndx);
end

xe = [ue',ve',we'];

%=====

function rll=xe2rll(xe)

%Converts from Earth Frame to Radius, Longitude, & Latitude

ue = xe(:,1);
ve = xe(:,2);
we = xe(:,3);

for ndx = 1:length(xe)
    r(ndx) = sqrt((ue(ndx))^2+(ve(ndx))^2+(we(ndx))^2);
    lat(ndx)=asin(we(ndx)/r(ndx))*180/pi;

    long(ndx)=(ve(ndx)/abs(ve(ndx)))*acos(ue(ndx)/sqrt((ue(ndx))^2+(ve(ndx))^2))*180/pi;
end

rll = [r',lat',long'];

%=====

function BL=rllt2BL(R,lat,long,t,eti,Re)

%Finds Mag-Field Vector @ given alt, lat, long, time.

Bfyr = (t+eti)/3600/24/365.25+2000;
BR = R-Re;
BLat = 90-lat;
BLong = long;

for ndx=1:length(R)
    BLi(ndx,:) = magfd(Bfyr(ndx),1,BR(ndx),BLat(ndx),BLong(ndx));
end

BL=(1e-9)*BLi; %Mag field (Teslas)

%=====

```

```

function xe=xm2xe(mfv,lat,long)

%Converts from Mag-Field Frame to Earth Frame

um = mfv(:,1);
vm = mfv(:,2);
wm = mfv(:,3);

xm = [um';vm';wm'];

lt = pi/180*lat;
lg = pi/180*long;

for ndx=1:length(mfv)
    xe(:,ndx)=[-sin(lt(ndx))*cos(lg(ndx)),-sin(lg(ndx)),-
cos(lt(ndx))*cos(lg(ndx));
               -sin(lt(ndx))*sin(lg(ndx)),cos(lg(ndx)),-
cos(lt(ndx))*sin(lg(ndx));
               cos(lt(ndx))0,-sin(lt(ndx))
]*xm(:,ndx);
end

xe=xe';

%=====

function xi=xe2xi(xe,t,dti,wei,veo)

%Converts from Earth-Fixed Frame to Inertial Frame

xe=xe';

off=veo*3600*wei;

for ndx=1:length(xe)
    xi(:,ndx) = [cos((wei)*(t(ndx)+dti)+off),-sin((wei)*(t(ndx)+dti)+off),0;
                 sin((wei)*(t(ndx)+dti)+off),cos((wei)*(t(ndx)+dti)+off),0;
                 0,0,1]*xe(:,ndx);
end

xi=xi';

%=====

function gai=r2gai(xi,Re,Lv)

%Creates the boundary on Earth in inertial coordinates that can view the S/C

Rv = xi(length(xi),:);
Rm = norm(Rv);

r = Re*cos(Lv)*(cos(asin(Re/Rm*cos(Lv)))-Re/Rm*sin(Lv));
cm = Re*(sin(Lv)*cos(asin(Re/Rm*cos(Lv)))+Re/Rm*(cos(Lv))^2);
cv = cm/Rm*Rv;

ci1 = (-r):10:(+r);
ci2 = ci1;
ci = [flipud(ci1');ci2';ci1(length(ci1))];
cj1 = sqrt(r^2-(ci1).^2);
cj2 = -sqrt(r^2-(ci2).^2);
cj = [flipud(cj1');cj2';cj1(length(cj1))];
ck = zeros(size(ci));
cx = [ci,cj,ck];

```

```

if Rv(1)>0
    th = atan(Rv(2)/Rv(1))+pi/2;
else
    th = atan(Rv(2)/Rv(1))+3*pi/2;
end

ph = pi-atan(sqrt((Rv(1))^2+(Rv(2))^2)/Rv(3));

cii = (ci*cos(th)-cj*cos(ph)*sin(th)-ck*sin(ph)*sin(th))+cv(1);
cji = (ci*sin(th)+cj*cos(ph)*cos(th)+ck*sin(ph)*sin(th))+cv(2);
cki = (          -cj*sin(ph)          +ck*cos(ph))+cv(3);
cxi = [cii,cji,cki];
gai = cxi;

%=====
function [galo,gala]=gai2gall(gai,t,dti,wie,i,veo)

%Creates Plottable Matrices of the Lat and Long defining
%the Ground Area that can view the S/C from the coordinates
%of that boundary in the inertial frame

ui = gai(:,1);
vi = gai(:,2);
wi = gai(:,3);

f=length(t);
off=veo*3600*wie;
for ndx = 1:length(gai)
    ue(ndx)
    cos((wie)*(t(f)+dti)+off)*ui(ndx)+sin((wie)*(t(f)+dti)+off)*vi(ndx);
    ve(ndx)
    sin((wie)*(t(f)+dti)+off)*ui(ndx)+cos((wie)*(t(f)+dti)+off)*vi(ndx);
    we(ndx) = wi(ndx);
end

gae = [ue',ve',we'];

gall = xe2rll(gae);

long = gall(:,3);
lat = gall(:,2);

count=0;

for index=1:length(long)
    if (long(index)<-179) | (long(index)>179)
        count=count+1;
    end
end

if count>0
    n = 1;
    m = 0;
    for ndx=1:length(long)
        if i(length(i))>(pi/2)
            if ndx==1|ndx==2
                longm(ndx,n)=long(ndx);
                latm(ndx,n)=lat(ndx);
            else
                if (long(ndx)>long(ndx-1)) | ((long(ndx)<long(ndx-1)) & (long(ndx-1)>long(ndx-2)))
                    n=n+1;
                    m=ndx-1;
                end
            end
        end
    end
end

```

```

        longm(ndx-m,n)=long(ndx);
        latm(ndx-m,n)=lat(ndx);
    else
        longm(ndx-m,n)=long(ndx);
        latm(ndx-m,n)=lat(ndx);
    end
end
elseif i(length(i)) < (pi/2)
    if ndx==1|ndx==2
        longm(ndx,n)=long(ndx);
        latm(ndx,n)=lat(ndx);
    else
        if (long(ndx) < long(ndx-1)) | ((long(ndx) > long(ndx-1)) & (long(ndx-1) < long(ndx-2)))
            n=n+1;
            m=ndx-1;
            longm(ndx-m,n)=long(ndx);
            latm(ndx-m,n)=lat(ndx);
        else
            longm(ndx-m,n)=long(ndx);
            latm(ndx-m,n)=lat(ndx);
        end
    end
end
else
    longm=long;
    latm=lat;
end
end
galo=longm;
gala=latm;
else
    galo=long;
    gala=lat;
end
end

```

=====

function ad=roundto(a,b)

```

% Rounds a number (a) to a resolution (b)
c = rem(a,b);
d = c/b;
[m,n]=size(a);

for mdx=1:m
    for ndx=1:n
        if d(mdx,ndx) >= 0.5
            a(mdx,ndx) = a(mdx,ndx) + (b-c(mdx,ndx));
        elseif d(mdx,ndx) <= -0.5
            a(mdx,ndx) = a(mdx,ndx) - (b+c(mdx,ndx));
        else
            a(mdx,ndx) = a(mdx,ndx) - c(mdx,ndx);
        end
    end
end

ad=a;

```

=====

function [longm,latm]=col2mat(long,lat,i)

```

%Converts from Column to Matrix
%
1

```

```

%          2          1 -3
%Changes  -3    to   2 -2
%          -2          0 -1
%          -1

n = 1;
m = 0;

for ndx=1:length(long)
    if i(ndx)>(pi/2)
        if ndx==1
            longm(ndx,n)=long(ndx);
            latm(ndx,n)=lat(ndx);
        else
            if long(ndx)>long(ndx-1)
                n=n+1;
                m=ndx-1;
                longm(ndx-m,n)=long(ndx);
                latm(ndx-m,n)=lat(ndx);
            else
                longm(ndx-m,n)=long(ndx);
                latm(ndx-m,n)=lat(ndx);
            end
        end
    elseif i(ndx)<(pi/2)
        if ndx==1
            longm(ndx,n)=long(ndx);
            latm(ndx,n)=lat(ndx);
        else
            if long(ndx)<long(ndx-1)
                n=n+1;
                m=ndx-1;
                longm(ndx-m,n)=long(ndx);
                latm(ndx-m,n)=lat(ndx);
            else
                longm(ndx-m,n)=long(ndx);
                latm(ndx-m,n)=lat(ndx);
            end
        end
    else
        longm=long;
        latm=lat;
    end
end

%=====

function keps=tle2keps(tle,mu)

%Converts NASA TLE to Keplerian Elements

i = tle(1);
Om = tle(2);
e = tle(3);
om = tle(4);
M = tle(5);
n = tle(6);

a = (mu/n^2)^(1/3);

E = Me2E(M,e);
nu = 2*atan(sqrt((1+e)/(1-e))*tan(E/2));

keps = [a; e; nu; i; Om; om];

```

```

%=====

function E=Me2E(M,e)

%Solves for Eccentric Anomaly given Mean Anomaly and
%Eccentricity using Newton's Iteration Method

Ec = M;
Ei = Ec - (Ec-e*sin(Ec)-M)/(1-e*cos(Ec));

while (abs(Ei-Ec)>1e-7)
    Ec = Ei;
    Ei = Ec - (Ec-e*sin(Ec)-M)/(1-e*cos(Ec));
end;

E = Ei;

%=====

function stateD=oDiffEq(t,state,mu,J2,nD20,Re)

%The Orbital Differential Equations

n = state(1);%Mean Motion
nD = state(2);%First Derivative of Mean Motion (rad/s2)
a = state(3);%(mu/n^2)^(1/3);Semi-Major Axis
e = state(4);%Eccentricity
i = state(5);%Inclination (rad)
Om = state(6);%RAAN (rad)
om = state(7);%Arg of Perigee (rad)
nu = state(8);%True Anomaly (rad)
nuD = state(9);%Angular Velocity (rad/s)
r = state(10);%(a*(1-e^2))/(1+e*cos(nu))%Radius (km)
rD = state(11);%Radial Velocity (km/s)

stateD(1) = nD;
stateD(2) = nD20;
stateD(3) = 0;
stateD(4) = 0;
stateD(5) = 0;
stateD(6) = (pi*cos(i))/(43200*n)*(-0.00338-0.00154)*pi/15552000 ...
    -1.5*n*J2*(Re/a)^2*cos(i)/((1-e^2)^2);
stateD(7) = (pi*(4-5*(sin(i))^2))/(43200*n)*(0.00169+0.00077)*pi/15552000 ...
    +0.75*n*J2*(Re/a)^2*(4-5*(sin(i))^2)/((1-e^2)^2);
stateD(8) = nuD;
stateD(9) = -2*rD*nuD/r;
stateD(10) = rD;
stateD(11) = -mu/r^2 + r*nuD^2;

stateD=stateD';

%=====

function xb=xi2xb(xi,q)

%Inertial->Body Quaternion Transformation Matrix for Orbit Propagator

xin=xi';

for ndx=1:length(xi)
    i2b=[1 - 2*(q(ndx,2)^2 + q(ndx,3)^2), 2*(q(ndx,1)*q(ndx,2) +
q(ndx,3)*q(ndx,4)), 2*(q(ndx,1)*q(ndx,3) - q(ndx,2)*q(ndx,4));

```



```

        2*(q(ndx,1)*q(ndx,2) - q(ndx,3)*q(ndx,4)), 1 - 2*(q(ndx,1)^2 +
q(ndx,3)^2), 2*(q(ndx,2)*q(ndx,3) + q(ndx,1)*q(ndx,4));
        2*(q(ndx,1)*q(ndx,3) + q(ndx,2)*q(ndx,4)), 2*(q(ndx,2)*q(ndx,3) -
q(ndx,1)*q(ndx,4)), 1 - 2*(q(ndx,1)^2 + q(ndx,2)^2)];
        xbn(:,ndx) = i2b*xin(:,ndx);
end

xb=xbn';

%=====

function Bb=Bi2Bb(to,Bio,ta,q)

%Inertial->Body Quaternion Transformation Matrix for Orbit Propagator

Bia=interp1(to,Bio,ta);
Bia=Bia';

for ndx=1:length(ta)
    i2b=[1 - 2*(q(ndx,2)^2 + q(ndx,3)^2), 2*(q(ndx,1)*q(ndx,2) +
q(ndx,3)*q(ndx,4)), 2*(q(ndx,1)*q(ndx,3) - q(ndx,2)*q(ndx,4));
        2*(q(ndx,1)*q(ndx,2) - q(ndx,3)*q(ndx,4)), 1 - 2*(q(ndx,1)^2 +
q(ndx,3)^2), 2*(q(ndx,2)*q(ndx,3) + q(ndx,1)*q(ndx,4));
        2*(q(ndx,1)*q(ndx,3) + q(ndx,2)*q(ndx,4)), 2*(q(ndx,2)*q(ndx,3) -
q(ndx,1)*q(ndx,4)), 1 - 2*(q(ndx,1)^2 + q(ndx,2)^2)];
    Bb(:,ndx) = i2b*Bia(:,ndx);
end

Bb=Bb';

%=====

function stateD = aDiffEq(t,state,I,K,mub,to,Bi,Treq,test,mm)

%The Attitude Differential Equations

w=state(1:3);
q=state(4:7);

Bb = Bi2Bb(to,Bi,t,q'); %Magnetic field in body frame (Tesla)

if test==1
    T = Treq; %Torque directly from command (for debugging)
else
    T = cross(mub',Bb'); %Torque using magnetorquers
end

mm1 = interp1(to,mm,t); %Mean Motion(rad/s)

C11 = 1-2*(q(2)^2+q(3)^2); %3 components of quaternion transformation
C21 = 2*(q(1)*q(2)-q(3)*q(4)); %matrix necessary for gravity gradient
C31 = 2*(q(1)*q(3)+q(2)*q(4));

% GG = [0 0 0];
GG = [-K(1)*3*mm1^2*C21*C31 -K(2)*3*mm1^2*C11*C31 -K(3)*3*mm1^2*C11*C21];

wD = [K(1)*w(2)*w(3)+T(1)/I(1)+GG(1);
        K(2)*w(3)*w(1)+T(2)/I(2)+GG(2);
        K(3)*w(1)*w(2)+T(3)/I(3)+GG(3)];

Wp = [ 0, w(3), -w(2), w(1);
        -w(3), 0, w(1), w(2);
        w(2), -w(1), 0, w(3);
        -w(1), -w(2), -w(3), 0];

```

```
qD = 1/2*Wp*q;  
stateD=[wD;qD] ;  
%=====
```